

**Solidification of AM and AZ magnesium alloys  
characterized by heat-transfer modeled  
thermal and calorimetric analysis and  
microsegregation study of directionally solidified  
microstructure**

Doctoral Thesis  
(Dissertation)

to be awarded the degree of  
Doctor of Engineering (Dr.-Ing.)

submitted by  
**Dipl.-Ing. Djordje Mirković**  
from Užice, Serbia

approved by the Faculty of Natural and Materials Sciences,  
Clausthal University of Technology

Date of oral examination  
9 May 2008

Chairperson of the Board of Examiners:

Prof. Dr.-Ing. habil. Lothar Wagner

Chief reviewer:

Prof. Dr.-Ing. habil. Rainer Schmid-Fetzer

Reviewer:

Prof. Dr.-Ing. habil. Andreas Bührig-Polaczek

This work has been conducted at the Institute of Metallurgy  
of the Clausthal University of Technology

©2008 Djordje Mirković

Any use of texts and images, even in part, without the written consent of the copyright holder is prohibited. In particular, this is true for reproduction, translation or use in electronic systems.





---

## Table of contents

<b>List of symbols .....</b>	<b>v</b>
<b>List of abbreviations .....</b>	<b>vii</b>
<b>1 Introduction .....</b>	<b>1</b>
<b>2 Solidification curves obtained from heat-transfer modeled</b>	
<b>DTA experiments.....</b>	<b>4</b>
2.1 Introduction .....	4
2.2 Comparison of different methods to determine solidification curves .....	4
2.3 DTA Experiment and Heat-Transfer Model (DTA-HTM) .....	8
2.3.1 DTA experiment .....	8
2.3.2 Heat-transfer model (HTM).....	11
2.4 How reproducible and reliable are DTA-HTM solidification curves?.....	17
2.4.1 Impact of base line fitting .....	18
2.4.2 Different cooling runs using the same sample.....	19
2.4.3 Different samples and capsule design.....	19
2.5 Alternative determination of solidification curves and comparison with DTA-HTM data .....	20
2.5.1 Quenching and Image Analysis (QIA) .....	20
2.5.2 Thermodynamic calculation of the solidification curves.....	21
2.6 Discussion.....	21
2.6.1 Conventional thermal analysis compared to DTA .....	23
2.6.2 Relationship between QIA and DTA-HTM solidification curves.....	23
2.6.3 Relationship between thermodynamic calculations and DTA-HTM solidification curves .....	24
2.6.4 Influence of the Mn addition .....	25
2.6.5 Reliability of the DTA-HTM solidification curves .....	26
2.7 Conclusions .....	27
<b>3 Solidification curves determined from DSC with improved heat-transfer modeling .....</b>	<b>28</b>
3.1 Introduction .....	28
3.2 DSC Experiment and Heat-Transfer Model (DSC-HTM) .....	28
3.2.1 DSC experiment .....	28
3.2.2 Heat-transfer model (HTM).....	32
3.3 Results .....	43
3.3.1 DSC-HTM analysis of important magnesium alloys .....	43
3.3.2 Comparison with thermodynamic calculations of the solidification curves.....	52
3.3.3 Reproducibility of DSC-HTM solidification curves .....	53

---

---

3.4 Discussion.....	54
3.4.1 Trends in the DSC-HTM solidification curves of Mg alloys and relation to thermodynamic calculations.....	54
3.4.2 Intricacy of the "liquidus" temperature and Mn content .....	56
3.4.3 Higher order time constants.....	57
3.4.4 Conventional thermal analysis compared to DSC.....	59
3.5 Conclusions .....	59
<b>4 Comparison of DTA-HTM and DSC-HTM solidification curves .....</b>	<b>61</b>
4.1 Introduction .....	61
4.2 DTA and DSC Experiments and corresponding Heat-Transfer Model (DTA-HTM and DSC-HTM) .....	61
4.2.1 Experimental procedure.....	61
4.2.2 Heat-transfer model (HTM).....	63
4.3 Results and discussion.....	65
<b>5 Directional solidification of Mg-Al alloys and microsegregation study of Mg alloys AZ31 and AM50, part I: Methodology .....</b>	<b>68</b>
5.1 Introduction .....	68
5.2 Reactions of Al-containing alloys with sample containers: a critical review .....	70
5.2.1 Criteria for tube material selection .....	70
5.2.2 Alternative non-ferrous tube materials .....	71
5.2.3 Uncoated steel application.....	71
5.2.4 Protective measures .....	72
5.3 Experimental procedure.....	73
5.3.1 Starting magnesium alloy material .....	73
5.3.2 Sample tube material and inside protective coating .....	74
5.3.3 Sample tube filling procedure.....	75
5.3.4 Bridgman equipment and DS procedure .....	75
5.3.5 Microstructure and microsegregation characterization .....	77
5.4 Processing of the quantitative EPMA data.....	78
5.5 The total solute profile during Scheil solidification .....	81
5.6 Results .....	83
5.6.1 Reactions between unprotected steel tube and liquid alloy .....	83
5.6.2 Performance of BN-coated steel tubes .....	85
5.6.3 Microstructure in the mushy zone near the solidification front.....	87
5.6.4 EPMA-WDS microsegregation data beneath the mushy zone.....	88
5.7 Discussion.....	92
5.7.1 Sample container and directional solidification .....	92
5.7.2 Issues regarding quantitative EPMA mapping .....	95
5.7.3 EPMA data sorting: Comparison of leading-element sort to WIRS.....	95

---

---

5.7.4	WIRS solute profiles compared with Scheil-total .....	96
5.8	Conclusions .....	96
<b>6</b>	<b>Directional solidification of Mg-Al alloys and microsegregation study of Mg alloys AZ31 and AM50.</b>	
	<b>part II: Systematic comparison between AZ31 and AM50.....</b>	<b>98</b>
6.1	Introduction and procedures .....	98
6.2	Results and discussion.....	99
6.2.1	Difference between AZ31 and AM50 regarding the performance of BN-coated steel tubes.....	99
6.2.2	Microstructure in the mushy zone near the solidification front.....	100
6.2.3	EPMA-WDS microsegregation data beneath the mushy zone.....	105
6.3	Conclusions .....	110
<b>7</b>	<b>Summary .....</b>	<b>111</b>
	<b>Appendices .....</b>	<b>113</b>
Appendix A	The use of Ta-encapsulation at extreme conditions.....	113
Appendix B	Details of the reaction between steel tube and Mg-Al alloy.....	116
Appendix C	DSC response to the varying Zn content in Mg-Al-Zn alloys.....	121
	<b>References .....</b>	<b>125</b>
	<b>Curriculum vitae .....</b>	<b>129</b>

---



## List of symbols

$T_S$	temperature of sample [ $^{\circ}\text{C}$ ];
$T_{MS}$	temperature of sample thermocouple [ $^{\circ}\text{C}$ ];
$T_R$	temperature of reference [ $^{\circ}\text{C}$ ];
$T_{MR}$	temperature of reference thermocouple [ $^{\circ}\text{C}$ ];
$T_F$	furnace temperature [ $^{\circ}\text{C}$ ];
$\beta$	= $dT_R/dt$ scanning rate [ $\text{K min}^{-1}$ ];
$\Delta T_M$	= $T_{MS} - T_{MR}$ [ $\text{K}$ ];
$\Delta T$	= $T_S - T_R$ [ $\text{K}$ ];
$C_S$	heat capacity of sample material [ $\text{J K}^{-1}$ ];
$C_R$	heat capacity of reference material [ $\text{J K}^{-1}$ ];
$C_C$	heat capacity of sample/reference crucible [ $\text{J K}^{-1}$ ];
$R_1$	heat flow resistance between furnace and sample/reference crucible [ $\text{K W}^{-1}$ ];
$R_2$	heat flow resistance between sample and sample thermocouple [ $\text{K W}^{-1}$ ];
$\Phi_{FS}$	furnace-to-sample crucible heat flow [ $\text{W}$ ];
$\Phi_{FR}$	furnace-to-reference crucible heat flow [ $\text{W}$ ];
$\Phi_r$	heat flow generated by sample reaction [ $\text{W}$ ];
$\Phi_M$	= $(\Phi_{FR} - \Phi_{FS})$ - (baseline value), measured heat flow (smeared) [ $\text{W}$ ];
$f_L$	liquid phase fraction [ $\text{mol/mol}$ ];
$f_S$	= $1 - f_L$ , phase fraction of all solid phases [ $\text{mol/mol}$ ], [ $\text{g/g}$ ]
$H$	total latent heat of solidification of the sample [ $\text{J}$ ];
$h(t)$	cumulative amount of heat generated by sample reaction at time $t$ [ $\text{J}$ ];
$t$	time [ $\text{sec}$ ];
$\tau_1$	= $R_1 (C_S + C_C)$ the first time constant [ $\text{sec}$ ];
$\tau_2$	= $R_2 C_S$ the second time constant [ $\text{sec}$ ];
$G$	temperature gradient [ $\text{K mm}^{-1}$ ];
$V$	solidification rate [ $\mu\text{m sec}^{-1}$ ];
$GV$	cooling rate [ $\text{K sec}^{-1}$ ];
$\lambda_1$	average primary dendrite arm spacing [ $\mu\text{m}$ ];
$C_i^j$	measured concentration of component $j$ at measuring point $i$ [ $\text{wt.}\%$ ];
$R_i$	rank number assigned to each measuring point $i$ ;
$N$	total number of sampling points;
$C_{MIN}^j$	minimum concentration in the dataset for a given component $j$ [ $\text{wt.}\%$ ];
$C_{MAX}^j$	maximum concentration in the dataset for a given component $j$ [ $\text{wt.}\%$ ];
$\sigma^j$	experimental uncertainty associated with measurement of component $j$ [ $\text{wt.}\%$ ];
$\bar{C}_i^j$	weighted compositional value [-]; $\bar{C}_i^j = (C_i^j - C_{MIN}^j) / \sigma^j$ and $\bar{C}_i^j = (C_{MAX}^j - C_i^j) / \sigma^j$ for partitioning coefficient less and larger than unity, respectively;
$\bar{\bar{C}}_i$	mean value of $\bar{C}_i^j$ for all components [-];
$f_L(i)$	total fraction of residual liquid prior to precipitating a solid layer $i$ [ $\text{mol/mol}$ ];
$f_S(i)$	total fraction of entire solid material prior to precipitating a solid layer $i$ [ $\text{mol/mol}$ ];
$f(\varphi, i)$	$\varphi$ phase fraction in a layer number $i$ [ $\text{mol/mol}$ ];
$x(j, \varphi, i)$	composition of component $j$ in the solid phase $\varphi$ of the new solid layer $i$ [ $\text{at.}\%$ ];
$\bar{x}(j, i)$	overall composition of component $j$ in a layer number $i$ [ $\text{at.}\%$ ];
$\Delta f_S(i)$	change of the fraction of entire solid material referring to $f_S(i)$ ;
$N'$	number of crystallized layers.



## List of abbreviations

AAS	Atomic Absorption Spectrometry
DSC	Differential Scanning Calorimetry
DTA	Differential Thermal Analysis
EDS	Electron Dispersive Spectroscopy
EPMA	Electron Probe Micro Analysis
FEM	Finite Element Method
HTM	Heat Transfer Model
ICP-AES	Inductively Coupled Plasma Atomic Emission Spectroscopy
LOM	Light Optical Microscopy
QIA	Quenching and Image Analysis
SEM	Scanning Electron Microscope
WDS	Wavelength Dispersive Spectroscopy
WIRS	Weighted Interval Rank Sort

---





# 1 Introduction

From the broad spectrum of materials available today, the magnesium alloys are prominently present in fields of industrial applications where weight saving is one of the key factors in the construction of a product. A well-known example of such a field is the transportation industry, where the demand is high to reduce fuel consumption and emission of greenhouse gases. Research on magnesium base alloys became a hot topic in the last decade, not only because these alloys are light-weight materials, but also because of their promising mechanical properties, recyclability and the reduced price for primary magnesium. Nowadays these alloys form a class of materials competing with other light structural materials, such as aluminum based or polymers and, occasionally, steel based materials.

Almost all manufacturing routes dealing with metallic materials in industry start with a solidification step. A detailed understanding of solidification and knowledge of the as-cast microstructures are crucial for the achievement of the desired final cast component properties. This knowledge is also fundamental for the alloy development process, because the pursuant materials properties have to be developed from the as-solidified microstructure.

For this reason, extensive research has been performed on the solidification behavior of AM50, AZ31, AZ61, AZ62, and AZ91 commercial magnesium alloys. These selected alloys cover a wide range of typical applications such as rolling (AZ31), extrusion (AZ61), sand casting/welding wire (AZ62) and die casting (AM50 and AZ91).

The global goal and purpose of this thesis is to deepen the understanding of solidification of AM and AZ magnesium alloys by investigation of two cornerstones, which are complementary to each other regarding temperature gradient and solidification rate, and also with respect to the generated microstructure. One methodic progress aims at the determination of "solid fraction" or solidification curves, being an important characteristic of an alloy. The other aims at the reliable characterization of microstructure and microsegregation during directional solidification of these alloys.

The first cornerstone considers solidification under a negligible spatial temperature gradient and is treated in detail in Chapters 2, 3 and 4. Here the **solidification curves** were determined by developing an improved heat-transfer model (HTM) applicable to both differential thermal analysis (DTA) and differential scanning calorimetry (DSC) signals. The term "solidification curve" of an alloy is used for the solid (or remaining liquid) fraction *versus* temperature during solidification in a control volume with fixed overall alloy composition. The knowledge of this quantity is essential for the control of solidification and casting processes and a very important input parameter for solidification simulation software.

---

Also welding technology may benefit from that information. Recently Cao and Kou [2006Cao] reported on the application of the solidification curves as a tool for the prediction and elimination of liquidation-cracking occurring in partially melted zones in weldments of crack-susceptible Al alloys. The knowledge of solidification curves could also be very important for new semi-solid material casting processes, such as New Rheocasting [2003Fra] and Thixomolding<sup>®</sup> [2003Loh], which has recently started to become very interesting for magnesium alloys. Various methods are found in the literature to obtain or calculate the solidification curves of alloys. Their advantages and disadvantages and applicability to the Mg-alloys are critically reviewed in Chapters 2 and 3. The correlation between the enthalpy of solidification and the fraction of solid formed during solidification is one of the crucial issues in the determination of the solidification curves. Because [2003Don1] and [2003Lar] even claimed that the accurate determination of solidification curves cannot be obtained in a direct manner using enthalpy measurements, this issue was elaborated in detail in Chapter 3 of this thesis.

Three goals are set in this thesis to establish and advance the determination of the solidification curves.

The first goal is to provide quantitative solidification curves of a wide range of commercially important Mg alloys. The second one is to introduce a new method of desmearing, involving the independent determination of a time constant as a function of temperature for the applied equipment. Additionally, the interpretation of the measured curves is also elaborated in detail aiming at establishing a better desmearing of measured signals and minimizing the human error introduced by the operator.

The third goal was to develop a novel tantalum encapsulation enabling the proper treatment of the studied alloys. Due to high oxygen affinity and vapor pressure of investigated magnesium alloys, this special adaptation of the DTA/DSC setup using sealed Ta capsules appeared to be indispensable for the generation of reproducible and reliable data.

In **Chapter 2** a method is described where differential thermal analysis (DTA) is coupled to heat-transfer-modeling (HTM) to obtain solidification curves. In **Chapter 3** differential scanning calorimetry (DSC) is applied to obtain solidification curves. In **Chapter 4** a comparison is made of the results obtained in Chapters 2 and 3.

The second cornerstone is based on directional solidification in a high temperature gradient and at a constant solidification rate, achieved by the Bridgman technique. The resulting dendritic microstructure and inherent microsegregation will be treated in **Chapters 5 and 6** of this thesis. The extent of microsegregation present in solidified alloys impacts the successful

---

production and properties both of castings and of subsequently processed material. It is well-known that the thorough understanding of solute partitioning and buildup of microsegregation is vital for an effective control of as-cast properties. Also the efficiency of heat treatment and final mechanical properties, such as yield strength or toughness, are strongly influenced by the extent of as-cast segregation [2007Gan].

The *solute profiles* established in this thesis work, i.e. solute content versus solid phase fraction during solidification, are determined by an advanced treatment of the EPMA data, the weighted interval rank sort (WIRS).

The two critical difficulties arising in the experimental work are the loss of Al and the pollution of the melt due to the reaction between the liquid alloy and the ferrous sample container during directional solidification. This important issue was ignored in the literature dealing with directional solidification investigations carried out in the group of Mg-Al based alloys. Chapter 5 demonstrates that the key experimental challenge in the Bridgman technique applied to Mg alloys containing Al, is the development of a sufficiently inert sample tube. Providing reliable and reproducible results in subsequent microsegregation studies, required the development of a new experimental method, preserving the initial alloy composition at the start of the solidification.

A novel solution presented in this thesis is the application and optimization of a boron nitride (BN) coating preventing detrimental reaction between solute Al and sample container, or tube. Chapter 5 comprises a thorough investigation of the interplay between tube material, inside tube coating and details of the Bridgman device. The result of this investigation enables controlling the reactions present at the tube/sample interface.

Another methodic novelty, presented in Chapter 5, deals with the introduction of the correct implementation of the Scheil model for the solute profile calculation. The combination of the optimized method for directional solidification, sophisticated WIRS sorting scheme and true Scheil solute profile enables a reliable and more realistic microsegregation study of the Mg-alloys containing Al. This approach also proves to be a reliable tool for determination of correct phase sequence during solidification.

**Chapter 5** exemplifies the application of these novel methods to the alloy AZ31. In **Chapter 6** data for the alloy AM50 are presented together with a systematic comparison of results obtained for this alloy with those obtained for AZ31 alloy.

---

## 2 Solidification curves obtained from heat-transfer modeled DTA experiments

### 2.1 Introduction

An understanding of the solidification processes and the knowledge about as-cast microstructures are very important for achievement of desired final cast components properties. This knowledge is fundamental for the alloy development process, since pursuant material properties have to be developed from the as-solidified microstructure. This is valid especially for the casting process, which is one of the most important manufacturing methods of commercial magnesium alloys. As has been explained in Chapter 1, the term “solidification curve” of an alloy is used for the solid (or remaining liquid) fraction *versus* temperature during solidification in a control volume with fixed overall alloy composition.

In this study a differential thermal analysis (DTA) measurement with a mathematical heat-transfer model (HTM) is proposed as an *in-situ* method for providing solidification curves; its validity is checked by application to the AZ91 and AZ62 magnesium alloys. The AZ91 alloy was selected as the most processed Mg die cast alloy, while the AZ62 is used as the welding wire. Additionally, for both alloys the Mn content was varied in order to investigate its effect on the solidification path of the studied alloys. The main purpose of this work is to introduce a new method of desmearing involving the directly measured temperature dependence of a time constant ( $\tau_l$ ) and the heat flow resistance between the sample and its thermocouple in the Tian mathematical procedure. An improved sealed Ta-capsule design that can be used even for the very demanding Mg alloys enables reliable and reproducible DTA measurements, needed for the DTA-HTM method. Parameters influencing the reproducibility and reliability of the presented DTA-HTM solidification curves were studied.

### 2.2 Comparison of different methods to determine solidification curves

Various methods are applied to obtain or calculate the solidification curves of alloys. A traditionally performed procedure is quenching and image analysis (QIA). In QIA the sample is equilibrated at a temperature in the solidification range, quenched, and subsequently subject to metallographic preparation. The fraction of the liquid present in the sample prior to quenching is determined by applying quantitative image analysis. This determination is based on the difference in the microstructure of quenched melt to microstructure already solidified

---

prior to quenching, usually being more coarse. Some of the problems which may be experienced in applying this technique are difficulties to freeze-in the microstructure during quenching, avoiding further growth of the primary solid phase(s) and differentiation of the microstructure especially for commercial alloys which usually contain complex phases, and non-uniformity within the sample due to segregation caused by non-equilibrium solidification [1995Jen, 1996Che1]. Even though QIA appears to be a most direct experimental technique it is considered as being inaccurate due to these reasons. Furthermore, it is very tedious because for each temperature point within the freezing range an independent experiment is necessary.

Alternatively, the solidification curve may be calculated using various solidification micro-models, if all the necessary thermodynamic data *and* thermophysical/kinetic parameters are available. Examples of this approach are given by [2002Boe, 2003Don1]. Quite often, these detailed data are not available, preventing the use of this elegant approach. A more practical, though simplified, approach is to apply the two limiting solidification models, namely Scheil and complete equilibrium [1998Kur]. This is especially useful for multicomponent alloys if a reliable thermodynamic database is available but no thermophysical/kinetic parameters.

There are other methods which may be used to indirectly estimate the solid fraction. This can be done by measuring properties such as electrical potential difference or uniaxial flow stress and mathematically relating the obtained values to fraction solid [1994Kui]. Recently, Bakhtiyarov et al. [2004Bak] presented a method where the opposing torque generated in the sample by a surrounding rotating magnetic field is related to amount of solid phase in a solidifying melt. At the present time, the literature provides very few details about these indirect methods which will not be considered further here.

A new method, in which high-energy synchrotron X-rays are used for *in-situ* direct-beam imaging of solidification processes was recently developed and demonstrated to be successful in studies of Sn-Pb [1999Mat] and Sn-Bi [2006Li] alloys, and for more challenging Al-Cu alloys [2002Mat, 2005Mat]. This method allows experimental mapping of the liquid-solid interface morphology and propagation. Different X-ray absorption of elements also enables measurement of concentration gradients. Investigation of dendrite fragmentation [2005Mat1], coarsening and remelting [2006Li] is also feasible. Typically, quasi-2D measurements under directional solidification are presented [2005Mat, 2005Mat1], but also 3-D tomography studies of atomized droplets are shown [2004Pra]. This promising method enables *in-situ* investigation of the liquid-solid interface during solidification, with nominal spatial and temporal resolutions down to 1.4  $\mu\text{m}$  and 150 ms, respectively, achieved with an Al-30 wt.% Cu alloy [2005Mat]. A limitation is the high complexity of the method, requiring a high

---

intensity, transversely coherent, monochromatic X-ray source, as well as a high-resolution fast-read-out detector system.

A large group of methods used to obtain solidification curves is based on different techniques of thermal analyses or calorimetry coupled with heat transfer modeling. These methods generally assume the proportionality between the latent heat evolved during the solidification of the sample and its corresponding fraction of solid. These methods may be subdivided regarding the applied thermal analysis or calorimetric technique as follows.

The conventional thermal analysis technique provides cooling curves, i.e. temperature vs. time, during solidification of the studied sample. Based on these cooling curves, the liquid phase fraction could be calculated by determining the cumulative area between the first derivative of the cooling curve and its “base line”. That base line is the first derivative of a hypothetical cooling curve without phase transformations and is difficult to determine. Applying the thermal analysis technique using two thermocouples (one in the center and one close to the crucible wall), Bäckerud et al. [1986Bac, 1988Tam] determined solidifications curves of various commercial aluminum alloys. Fredriksson et al. [1979Fre] used one thermocouple immersed in the melt and a controlled cooled furnace to study solidification of the cast iron alloys. Recently, Riddle et al. [2003Rid] applied the two-thermocouple method to the AZ91E Mg-alloy, paying attention to some precautions related to the melting and protection of Mg melts.

Differential thermal analysis (DTA) and differential scanning calorimetry (DSC) have also been used for the determination of liquid phase fractions. Such a DTA apparatus was applied by [1995Che1, 1995Jen, 1996Che1, 1996Che2, 1996Jen, 2006Mir], and the recorded DTA curves were converted into solidification curves for various Al alloys by mathematical modeling of the heat transfer between the furnace, the reference cell and the sample cell. Chen et al. [1997Che] used similar DTA technique for N4 Ni-based superalloy while Fredriksson et al. [1979Fre] applied the same technique to a high-speed steel.

A power compensated DSC was applied by Chen et al. [1998Che] for the determination of the solidification curves for various solders, and a heat flow DSC apparatus by [2003Mir] for AZ Mg-alloys using a sealed Ta capsule to protect the sample. Contrary to the conventional two-pan DSC apparatus (sample and reference), Dong et al. [2001Don1, 2003Don] applied a single-pan constant heat flow calorimeter with the thermocouple immersed in the sample and no reference pan. Direct immersion of the thermocouple in the sample is known to minimize many negative effects, such as smearing of signal caused by heat flow resistance between the point of temperature measurement at the thermocouple tip and the actual sample. In this case,

---

a possible reaction between sample material and sample thermocouple could be one of the limiting factors.

The heat transfer between the sample and various parts of the DTA or DSC apparatus has been extensively studied. The usual procedure is to consider that different parts of the applied equipment (sample, sample crucible, reference, reference crucible, furnace etc.) have different temperatures, but a homogenous temperature distribution [1968Gra, 1979Fre, 2001Don, 2002Boe]. These temperatures and their corresponding heat flows are then interrelated through the heat flow resistance between considered parts. The main differences between these various heat transfer models are recognized through the different heat exchange phenomena considered, such as radiation, conduction and convection applied on a different number of parts of measuring equipment. A detailed review of these analyses is presented by Boettinger and Kattner [2002Boe]. Usually analytical solutions for the heat transfer models are provided [1968Gra, 1989Hem, 2002Boe], although some numerical solutions are also reported [2001Don1, 2005Don].

Another approach is numerical simulation of the heat exchange in a measurement chamber applying a finite element method (FEM) to split up the whole DTA arrangement into small cells for which the heat flow and material properties are defined. This method applied by Banerjee et al. [1995Ban] takes the actual geometry of the DTA sample cup into account with the corresponding temperature gradients in the cup. The numerical method shows some advantages over analytical heat-transfer models which may be very difficult to solve analytically if the complexity is increased. As shown by [1995Ban], application of the numerical simulation is also rather complex and does not perform very well for alloys with unknown thermophysical parameters.

A second important role of a heat-transfer model, beside description of the temperatures and heat flows inside the system, is to perform the so-called desmearing of the DTA/DSC signal. This is especially important if the DTA/DSC signal is used to study the kinetics of reactions, such as solidification of the sample. Generally, the recorded DTA/DSC signal is not directly equivalent to the actual heat flow (the rate of the reaction) in the sample due to the observed thermal lag between the thermal event and corresponding thermocouple response [1985Loe]. Distortion and delay of the DTA/DSC signal related to the original thermal effects occurring in the sample are known as smearing [1989Hem, 1993UIb, 1994Loe].

If this effect is neglected, wrong interpretations are likely. For example, an isothermal reaction in the sample (melting/solidification of a pure metal) can be observed to happen over a temperature range. The knowledge of the functional relation between the measured signal and the true heat quantity, consumed or produced during the reaction is indispensable if

---

kinetics of a reaction, in this case solidification, is investigated [1996Hoe]. The application of this relation to the measured signal is called desmearing, and can be done using two methods: the first one is based on the Tian equation [1968Gra, 1996Hoe] and the second one by solving the convolution integral [1993UIb, 1996Hoe]. For the second method, the measuring apparatus must be equipped with a built-in heater to produce a pulse-like signal in order to determine an apparatus function. This is not always available and there are some more disadvantages, such as questions arising by fitting the built-in resistor (see section 3.4.3), rather ambitious mathematics required and noise increase. Therefore, this method is not further detailed in the present work; instead, the Tian equation will be used.

## 2.3 DTA Experiment and Heat-Transfer Model (DTA-HTM)

### 2.3.1 DTA experiment

The chemical compositions of four magnesium alloys studied in this Chapter are shown in a **Tab. 2.1**, denoted as AZ91Mn, AZ62Mn, AZ91 and AZ62. Two master alloys, the AZ91HP and the AZ61 provided by Norsk Hydro Magnesiumgesellschaft mbH, Bottrop, have been used for preparation of the alloys with the higher content of manganese (AZ91Mn, AZ62Mn). The AZ91Mn alloy was used as delivered AZ91HP master alloy, while the AZ62Mn alloy was prepared by adding high purity Zn to the AZ61 master alloy. The chemical compositions of master alloys were certified by the producer. The compositions of master and prepared alloys were additionally analyzed in our chemical laboratory using AAS (atomic absorption spectrometry). Alloys with virtually no manganese (AZ91 and AZ62 in Tab. 2.1) were prepared using following pure materials: Mg bars, min 99.9 wt.% provided by Norsk Hydro Magnesiumgesellschaft mbH, Bottrop; Al bars, 99.98 wt.% produced by Hydro Aluminium High Purity GmbH, Grevenbroich and Zn rods, 99.98 wt.% obtained from the Harzer Zink GmbH, Goslar, all purities referred to metal basis. For each alloy approximately 3 kg starting material was melted and holds for 10 minutes at 750°C in stainless steel crucible. The melt was protected by mixture of 0.4 vol.% SF<sub>6</sub> and 3 vol.% Ar in air. After the homogenization by mechanical stirring, the melt was cast in a cold heavy steel mold.

---



**Table 2.1.** Chemical composition of the alloys studied, balance Mg [wt.%]

Alloy	Al	Zn	Mn	Si	Fe	Cu	Ni	Be
AZ62	6.34	2.37	0.0051	0.024	0.0094	0.0012	0.014	<0.0001
AZ62Mn	6.68	1.82	0.63	0.015	0.010	0.0015	0.0060	0.0007
AZ91	9.43	1.21	0.0064	0.032	0.0062	0.0014	0.0075	<0.0001
AZ91Mn	9.04	0.79	0.25	0.033	0.0054	0.0039	0.0065	0.0004

DTA measurements were performed using a Netzsch DTA 404 S apparatus (NETZSCH GmbH, Selb, Germany). An experimental set up for reactive alloys, based on a graphite crucible protected by glass-carbon coating, is commercially available from the manufacturer. Due to possible reaction between sample and crucible (formation of aluminum carbide) and especially a sample loss due to evaporation [2002Lin] this set up was not applied in this work.

Due to high oxygen affinity and vapor pressure of the investigated magnesium alloys, a special adaptation of DTA equipment using sealed Ta capsules (**Fig. 2.1**) and modified capsule holder (**Fig. 2.2**) was developed. This adaptation was found to be indispensable for reproducible and reliable DTA experiments in preliminary studies. The Ta-capsules were produced in our lab by using Ta tube with 10 mm outer diameter and 0.4 mm wall thickness and Ta sheet for capsule lid and bottom with 0.25 mm thickness, both of purity min. 99.9 wt.% (metal basis), by Plansee GmbH, Reutte, Austria. The Ta-capsules were filled up to 50 vol.% with the sample material and sealed by electric arc welding under argon with 1.5 bar total pressure. The average empty Ta-capsule weight was  $3520 \pm 30$  mg, and the typical sample weight was about 400 mg.

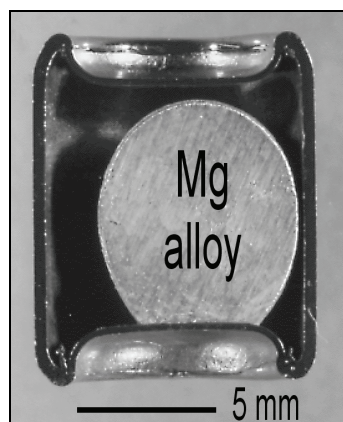


Figure 2.1. Cross-section of the optimized Ta-capsule filled with AZ62Mn sample material after being measured by DTA.

Several criteria were considered before the tantalum had been selected as capsule material. The most important one was the slow kinetic reactivity of Ta to tested material at applied measuring conditions. The reactions of Ta with Al and Mn were found as potentially critical and therefore additionally studied in this work. For this reason, the Ta-capsule was filled by AZ62Mn sample material, sealed and measured by DTA at 1 K/min scanning rate with three 300-650-300°C cycles with 15 minutes long isothermal segments between the ramps. This corresponds to an extensive exposure compared to the actual DTA experiments. A cross section of this capsule (Fig. 2.1) with emphasis on the inner sample/capsule contact surface was investigated using scanning electron microscopy coupled with energy dispersive X-ray microanalysis (SEM/EDX). No compounds characteristic for Mn-Ta ( $Mn_2Ta$ ) and Al-Ta ( $TaAl$ ,  $TaAl_2$ ,  $TaAl_3$ ) reactions were observed. Such a typical sample/capsule interface shown in **Fig. 2.3**, demonstrates that this capsule is sufficiently inert to all alloying components of the sample.

The second important factor that has been taken into consideration when selecting the capsule material is good heat conductivity in order to reduce heat-transfer resistance between the DTA sample and corresponding thermocouple. Furthermore, good weldability and mechanical stability of capsule material were very important considering the high vapor pressure of studied alloys. Tantalum meets all these requirements. More details on application of the Ta-encapsulation are given in Appendix A.

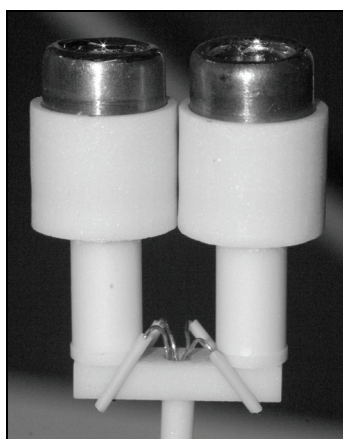


Figure 2.2. Customized DTA sample holder with reference and sample capsule.

For DTA measurements high-purity  $\gamma-Al_2O_3$  powder was used as the reference material. Prior to measurements a standard temperature calibration was performed by using the melting point of high purity Al, In, Mg, Pb and Sb elements. The DTA scanning program comprised cycles 350 - 650 - 350°C at heating/cooling rate of 1 and 5 K/min. The measurements were performed at  $5 \times 10^{-3}$  mbar static external vacuum to protect Ta-capsule outer surface against

---

oxidation and to eliminate convective heat exchange in gas inside the chamber. The overall uncertainty of the DTA measurements was estimated to be  $\pm 3$  K.

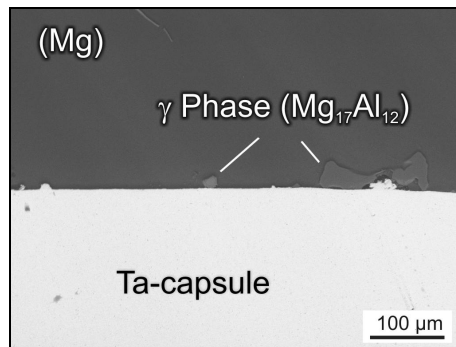


Figure 2.3. Cross section (BSE micrograph) of the AZ62Mn / Ta-capsule contact surface at bottom of the capsule shown in Fig. 2.1. No interface reaction of the alloy with Ta can be detected.

The microstructures of the samples after DTA experiments were examined by SEM/EDX. The samples were ground and polished down to 1  $\mu\text{m}$  diamond under alcohol to avoid reaction with water. The samples were etched in the solution of 1  $\text{cm}^3$   $\text{HNO}_3$ , 20  $\text{cm}^3$  acetic acid, 60  $\text{cm}^3$  ethylene glycol and 19  $\text{cm}^3$   $\text{H}_2\text{O}$  for 15 seconds at room temperature.

Additionally quenching experiments were performed as detailed later in section 2.5.1.

## 2.3.2 Heat-transfer model (HTM)

### 2.3.2.1 Desmearing of the DTA signal

In this work the heat-transfer model based on the Tian linear first-order differential equation is applied to desmear recorded DTA curves and to simulate heat transfer between DTA cells and the furnace during the solidification of the sample. A more detailed description of the model, comparing various assumptions, is given elsewhere [1968Gra, 1989Hem, 1996Hoe].

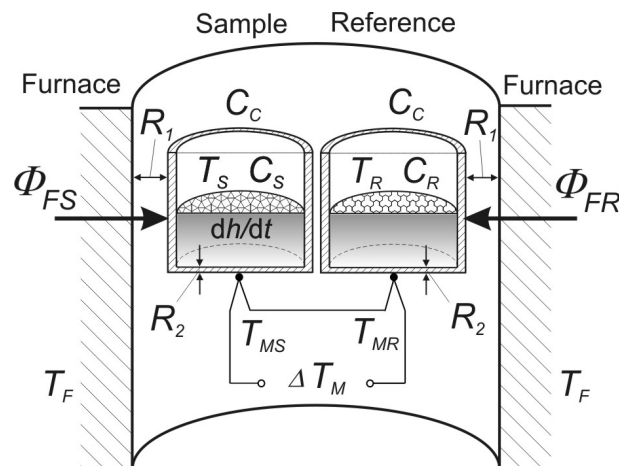


Figure 2.4. Schematic view of the DTA, with quantities used in heat transfer model.

A schematic diagram of the DTA equipment is shown in **Fig. 2.4** and the corresponding HTM quantities are summarized in the **List of symbols**. Sample and reference cells are depicted, both consisting of sample/reference material and crucible. The sample ( $T_S$ ) and reference ( $T_R$ ) temperatures are taken to be uniform inside the sample/reference material. In the first approximation they are also taken to be equal to those of actually measured temperatures at the corresponding thermocouple tips ( $T_{MS}$  and  $T_{MR}$ ). The heat flow ( $\Phi_{FS}$  or  $\Phi_{FR}$ ) between the furnace at temperature  $T_F$  and the sample/reference crucibles, respectively, has to overcome the corresponding heat flow resistance ( $R_l$ ). Based on the symmetry of the DTA equipment, this heat flow resistance is considered equal for both cells. The heat exchange between the sample and reference cells is neglected.  $\Delta T_M$  is the temperature difference between reference and sample thermocouples. This is the only directly measured quantity during the DTA experiment, besides  $T_{MR}$ . The heat generated in the sample cell per unit time,  $dh/dt$  is considered as positive and heat absorbed as negative. This heat generated by exothermic or endothermic reaction inside the sample cell implies a heat flow  $\Phi_r$ , which is expressed by Eq. (2.1):

$$\Phi_r = \frac{dh}{dt} \quad (2.1)$$

Applying the principle of energy conservation the heat balance of the sample cell during the solidification of a sample can be expressed by the following equation:

$$\Phi_r + \Phi_{FS} = (C_S + C_C) \frac{dT_{MS}}{dt} \quad (2.2)$$

That means that the sum of the heat flow generated inside the sample during solidification ( $\Phi_r$ ) and the heat flow arriving from the environment ( $\Phi_{FS}$ ) increases the temperature of the sample ( $T_S = T_{MS}$  in the present first approximation). The heat capacity of the thermocouple wires is neglected. The equivalent equation for the reference cell can be expressed as follows:

$$\Phi_{FR} = (C_R + C_C) \frac{dT_{MR}}{dt} \quad (2.3)$$

as no heat  $h$  is generated in reference cell. The heat capacities of the sample and reference crucibles are considered to be equal for both cells ( $C_C$ ). In analogy to Ohm's law, the furnace-to-cell heat flows can be written as:

$$\Phi_{FS} = \frac{T_F - T_{MS}}{R_l} \quad (2.4a)$$

$$\Phi_{FR} = \frac{T_F - T_{MR}}{R_l} \quad (2.4b)$$

It is further regarded that the heat capacity of the reference ( $C_R + C_C$ ) and the sample cell ( $C_S + C_C$ ) are identical ( $C = C_R + C_C = C_S + C_C$ ). This approximation is fitting very well to the applied Ta-capsule, which is much heavier than the both sample and reference. Therefore, the heat capacity of the cell ( $C$ ) is mostly determined by heat capacity of the capsule ( $C_C$ ). This consideration justifies the use of a single heat capacity of the sample ( $C_S$ ) that does not distinguish liquid or solid sample material.

Subtracting Eq. (2.3) from Eq. (2.2), and rearranging according to Eq. (2.4), the following expression is obtained, following the approach of Gray [1968Gra]:

$$R_1 \frac{dh}{dt} = (T_{MS} - T_{MR}) + R_1(C_S + C_C) \frac{d(T_{MS} - T_{MR})}{dt} \quad (2.5a)$$

$$R_1(C_S + C_C) = \tau_1 \quad (2.5b)$$

Here  $T_{MS} - T_{MR} = \Delta T_M$  [K] is the measured, smeared temperature difference between reference and sample thermocouples, generated mostly through the heat evolved during solidification of the sample. Here and in the following it is assumed that the base line, typically measured with an empty crucible, is already subtracted in the quantity  $\Delta T_M$ . This corresponds to the assumed equal heat capacities of sample and reference cells in Eq. (2.5).

In contrast to this quantity  $\Delta T_M$  measured during the DTA experiment, the term  $R_1(dh/dt)$  [K] is a desmeared temperature difference, where the smeared DTA signal is corrected using the term  $R_1(C_S + C_C)$ . This term is commonly marked as  $\tau_1$  and named the first time constant, as it is usually the largest time constant characteristic for the temperature balance between furnace and the sample. If further diversification is wanted, the higher-order time constants ( $\tau_2, \tau_3 \dots$ ) could be involved, as discussed later. The first time constant  $\tau_1 = R_1(C_S + C_C)$  is defined by heat flow resistance between furnace and the sample thermocouple and the heat capacity of the sample cell (sample and crucible together). Even though it involves the sample property  $C_S$ , it is essentially characteristic for the DTA equipment and depends on experimental set up such as crucible design and materials. In this work, the temperature dependence of the time constant  $\tau_1$  was experimentally found to be significant. This confirms the finding of a strong temperature dependence of resistance between furnace and sample thermocouple by Wiedemann and van Tets [1970Wie].

There are different methods to determine  $\tau_1$  time constant [1993Ulb, 1994Loe, 1996Hoe]. In this work the ( $\tau_1$ ) was independently determined using the solidification curves of pure metals measured at the same experimental conditions as the actual magnesium alloy samples.

The signal decay from the inflection point was fitted as an exponential decay as shown in **Fig. 2.5** for the Mg freezing peak at 5 K/min cooling rate. The exponential function can be derived from Eq. (2.5a) since  $dh/dt = 0$  in that part of the DTA curve. In this study Pb and Mg solidification curves were analyzed using the same conditions as in the actual alloy experiments (same Ta-capsule setup, scanning rates etc.). Values of  $\tau_l$  were 170 sec at 327°C (Pb), and 60 sec at 650°C (Mg) determined at 5 K/min scanning rate. No significant dependence on the scanning rate was observed.

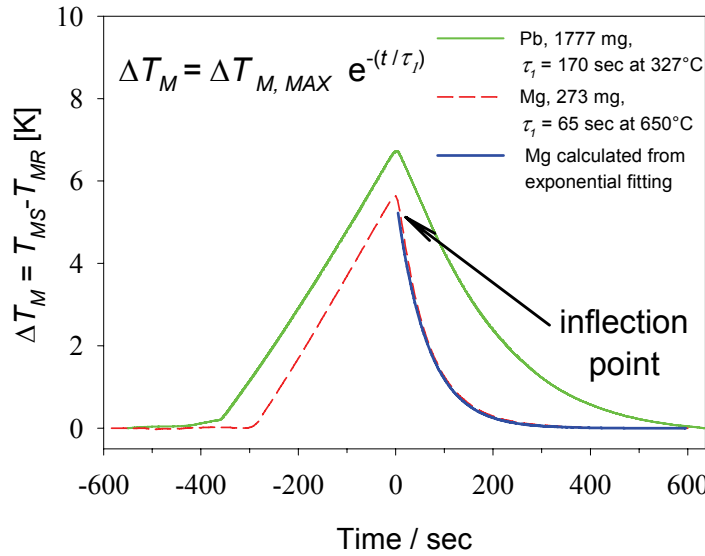


Figure 2.5. Experimental DTA freezing peaks of pure Pb and Mg at 5 K/min cooling rate and the calculated exponential signal decay for Mg. The significant variation of time constant  $\tau_l$  with temperature between 327°C and 650°C is demonstrated.

One possible way to improve the above presented heat flow model in a second approximation is the consideration of the so far neglected heat flow resistance between sample and its thermocouple ( $R_2$ ). This second heat flow resistance allows for different temperatures inside the sample and at the measuring point, as depicted in Fig. 2.4. The following equation for the sample cell is valid [1996Hoe]:

$$T_S = T_{MS} + \tau_2 \frac{dT_{MS}}{dt} \quad (2.6)$$

where  $\tau_2$  is the second time constant and is expressed as product of  $R_2$  and  $C_S$  ( $\tau_2 = R_2 C_S$ ). This next largest time constant is typically much smaller than  $\tau_l$ . An equation analogous to Eq. (2.6) can be written for the reference side and, typically, an identical time constant  $\tau_2$  for both sides, sample and reference is assumed, even though it was shown that  $R_2$  depends on the

substance in the crucible [1970Wie]. Combining available equations the following equation can be derived [1994Loe, 1996Hoe].

$$R_1 \frac{dh}{dt} = (T_{MS} - T_{MR}) + (\tau_1 + \tau_2) \frac{d(T_{MS} - T_{MR})}{dt} + (\tau_1 \cdot \tau_2) \frac{d^2(T_{MS} - T_{MR})}{dt^2} \quad (2.7)$$

To apply this advanced desmearing routine, the second time constant  $\tau_2$  must be determined. The usual way is application of a built-in calibration resistor to generate heat pulse with known electrical current and pulse time. The recorded pulse response,  $\Delta T_M$ , is then treated as superposition of two exponential functions and both time constants  $\tau_1$  and  $\tau_2$  are determined. The  $\tau_2$  essentially determine the ascending and the  $\tau_1$  descending part of the peak [1996Hoe], because  $\tau_2$  is predominantly affected by the signal delay between sample and sample thermocouple, whereas  $\tau_1$  is a measure for the signal delay between sample cell and furnace. Some disadvantages of this method need to be mentioned here. The majority of DTA and heat-flow DSC devices are not equipped with built-in calibration resistors and what is more important, for the accurate determination of the  $\tau_2$  the heat impulse should be released within the actual sample, which is difficult to realize [1983Sch]. These difficulties are substantially compounded for the customized DTA device of the present study. The fitting of a calibration resistor inside of the sealed Ta-capsule would be extremely difficult to realize, not to speak of placing it inside a Mg alloy sample. If this is not done, the applicability of a  $\tau_2$  value obtained in an empty Ta-capsule for the desmearing of DTA curve of particular sample material is questionable. For these reasons, the advanced desmearing procedure using Eq. (2.7) and involving the second time constant  $\tau_2$  is not applied in this work.

### 2.3.2.2 Relationship between enthalpy released during solidification and liquid phase fraction

It is not straightforward to establish an analytical correlation between the released enthalpy of solidification and the liquid (or solid) phase fraction for an alloy using thermal analysis techniques. Fredriksson et al. [1979Fre] assumed with some simplifications direct proportionality between the measured temperature difference and the solidification rate using the DTA technique. In other words,  $df_S/dt = \text{const} (T_{MS} - T_{MR})$ , where  $f_S$  is the fraction of solid [1979Fre]. Bäckerud et al. [1986Bac] has also assumed a linear relationship between released latent heat of solidification of commercial Al alloys and the solid fraction formed using a conventional thermal analysis technique. The mathematical procedure used by Bäckerud was based on the integration of the area between the first derivative of the cooling curve and its corresponding intricately constructed based line. The calculated area is taken to be directly

related to the released enthalpy of solidification and is assumed to be linearly proportional to the formed fraction solid of the considered alloy. No desmearing of the signal was performed in this method.

Chen et al. assumed a linear dependence of heat evolution,  $h$ , during solidification on the liquid phase fraction  $f_L$ , using Gray's interpretation of the Tian equation [1968Gra]. They applied this heat-transfer model to DTA experimental data [1995Jen, 1995Che1, 1996Che1, 1996Che2] and to power compensated DSC experimental data [1998Che] in order to determine solidification curves. This linearization is mathematically expressed as:

$$dh = H df_S = H d(1-f_L) \quad (2.8)$$

where  $H$  is assumed to be a constant for each alloy composition.  $H$  is the total latent heat of solidification. Since  $h(t)$ , as defined in Eq. (2.1), is also the cumulative amount of heat generated by sample reaction at time  $t$ , we have at the end of solidification  $h(t_{final}) = H$ .

This linear dependence is often considered as a very rough simplifying approximation. However, if the enthalpy is calculated as the function of  $f_L$  for the example of the AZ91Mn alloy using thermodynamic Mg-database [2001Sch] and Pandat software [2001Che] for two limiting cases, equilibrium and Scheil solidification curves, **Fig. 2.6** is obtained. Surprisingly good approximate linearity is obtained for the equilibrium case. Even for the solidification path calculated using Scheil's model the assumption of linear heat release is not too unreasonable as a first approximation. The specific heat contribution, included in Fig. 2.6, is also essentially linear and does not change that statement. The relationship between enthalpy released during solidification and liquid phase fraction is elaborated in more detail in section 3.2.2.3.

The following equation is derived from Eqs. (2.5) and (2.8) by applying all simplifications written in the finite-difference form for numerical solution:

$$\Delta f_S = \frac{\Delta t}{R_1 H} \left[ \Delta T_M(t) + \tau_1(T_{MR}) \left[ \frac{\Delta T_M(t + \Delta t) - \Delta T_M(t)}{\Delta t} \right] \right] \quad (2.9)$$

In previous work by Chen et al. the terms  $R_1 H$  and  $\tau_1$  were treated as two adjustable parameters determined from the measured DTA curve of *each* sample. The first time constant  $\tau_1$  was obtained from the after-reaction part of the DTA curve, by fitting to an exponential decay curve for each sample. The term  $R_1 H$  [K·s] was obtained by integration of the area between the DTA experimental curve,  $\Delta T_M(t)$ , from the onset of the first peak to the maximum of last peak corresponding to the termination of solidification; it was iteratively



adjusted to the boundary condition  $f_S = 1$  at this maximum [1996Che2, 1997Che]. This becomes problematic in the case of an unknown alloy sample where possible solid state reactions could corrupt the results. Furthermore, the total heat released should be related to the entire area including the exponential tail [1968Gra], since the  $\Delta T_M(t)$  signal is smeared.

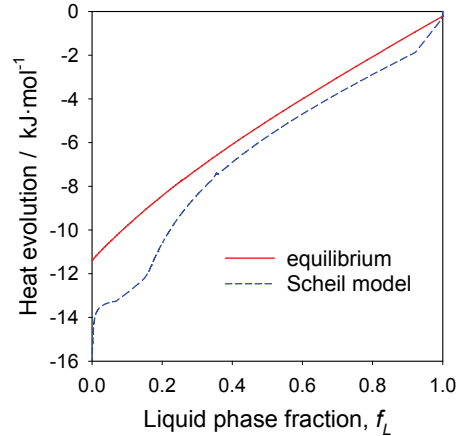


Figure 2.6. Calculated dependence of heat evolution (total enthalpy of alloy relative to its value at liquidus temperature) on liquid phase fraction during the solidification of the AZ91Mn alloy.

By contrast, in the present work  $\tau_I$  was determined in independent experiments. Based on the knowledge of  $\tau_I = \tau_I(T_{MR})$  the only remaining alloy-specific parameter in Eq. (2.9),  $R_I H$ , was determined as follows. Numerical integration of Eq. (2.9) is performed once for the product  $(R_I H) f_S(t)$  starting from  $t = t_0$  with  $f_S(t_0) = 0$  until  $t = t_S$  with  $f_S(t_S) = 1$ . The final integration step thus yields  $(R_I H) f_S(t_S) = R_I H$ . Knowing this constant we finally get  $f_L(t) = 1 - f_S(t)$  at any time  $t$  ( $t_0 \leq t \leq t_S$ ). The value of  $t_S$  had to be determined beforehand from the final peak maximum of the DTA signal. It is noted that the desmearing used in Eq. (2.9) does not change the area under curve  $\Delta T_M$  compared to the desmeared quantity in the square brackets of Eq. (2.9), thus retaining the total released heat.

## 2.4 How reproducible and reliable are DTA-HTM solidification curves?

The reproducibility of the presently obtained DTA-HTM solidification curves was studied by variation of three major conditions or parameters and comparing the calculated solidification curves. These include the influence of the operator subjectivity in selecting a base line and some experimental conditions. The results are given below and discussed in section 2.5.

### 2.4.1 Impact of base line fitting

In the case where a reproducible base line of the DTA signal could not be provided by the measurement (as was the case in this work), the base line can be interpreted/fitted in polynomial form. It is quite difficult to construct a “correct” base line in the cases of high uncertainty regarding to the nature of heat capacity changes that happen [1996Hoe], during solidification of the studied alloys. This is the case for the present alloys which are characterized by multiphase microstructure and high fraction of precipitated secondary phases, as shown in **Fig. 2.7** for one of the AZ91Mn samples.

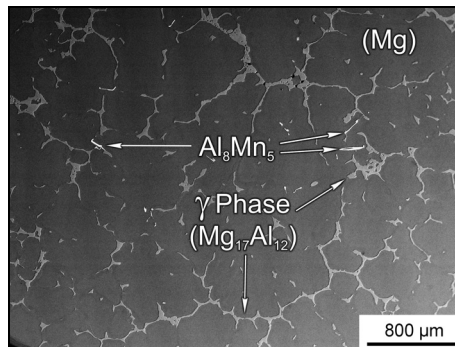


Figure 2.7. Electron micrograph (BSE) of the AZ91Mn sample solidified at 1 K/min.

To test the influence caused by the base line construction on the shape of the final calculated solidification curves, the base line was fitted by 3 suggested polynomials of the 2<sup>nd</sup>, 4<sup>th</sup> and 5<sup>th</sup> order (**Fig. 2.8a**). Some subjectivity is also induced by the operator's choice of the "undisturbed" parts of the DTA signal before and after the reaction to which the selected polynomial was fitted to. Here the DTA signal (per mass) of the AZ91Mn alloy cooled at 5 K/min was chosen as one example for fitting different base lines. The calculated DTA-HTM solidification curves, reflecting this variation are shown in **Fig. 2.8b**.

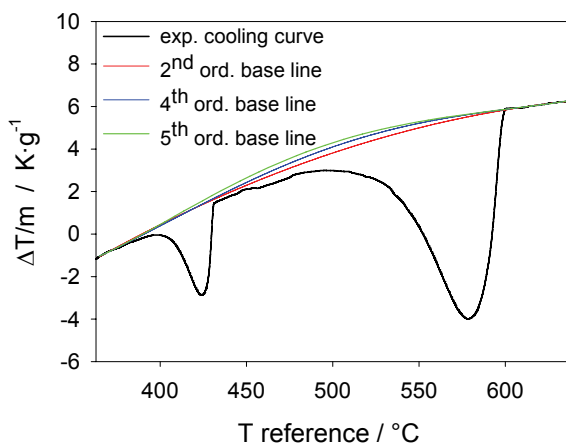


Figure 2.8a. The DTA signal of the AZ91Mn alloy at 5 K/min cooling rate with 3 base lines simulated by polynomials of the 2<sup>nd</sup>, 4<sup>th</sup> and 5<sup>th</sup> order.

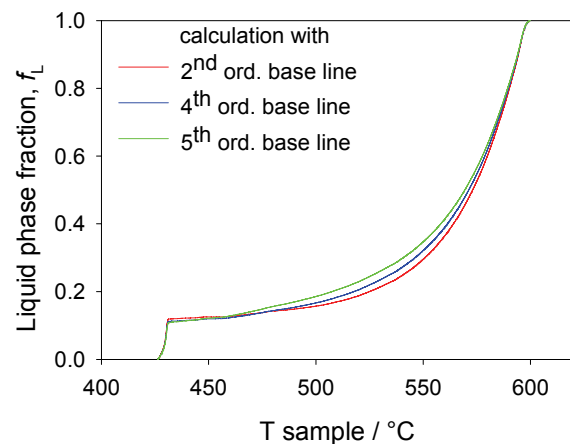


Figure 2.8b. DTA-HTM calculated solidification curves, reflecting the variations of Fig. 2.8a

### 2.4.2 Different cooling runs using the same sample

The repeatability of the calculated solidification curves has been checked by comparing the different cooling runs within the cycled measurements of the same sample. That is only possible in the adapted DTA setup using Ta-capsules which provide a perfect sealing of the reactive samples. This comparison is especially interesting if measured signals are obviously different, most likely caused by the movement of the capsule during the measurement, as shown for AZ91Mn alloy at 1 K/min cooling rate in **Fig. 2.9a**. For easier comparison, the base lines for both runs are fitted by polynomials of the 3<sup>rd</sup> order. The resulting DTA-HTM solidification curves presented in **Fig. 2.9b** are virtually identical.

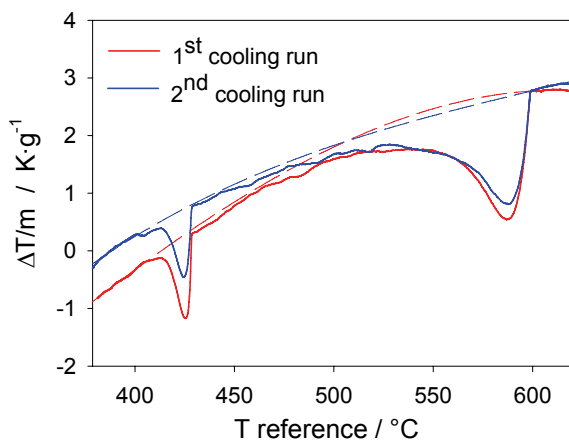


Figure 2.9a. The DTA signals of the same AZ91Mn sample at 1 K/min cooling rate recorded during the same measurement with base lines both simulated by polynomials of the 3<sup>rd</sup> order.

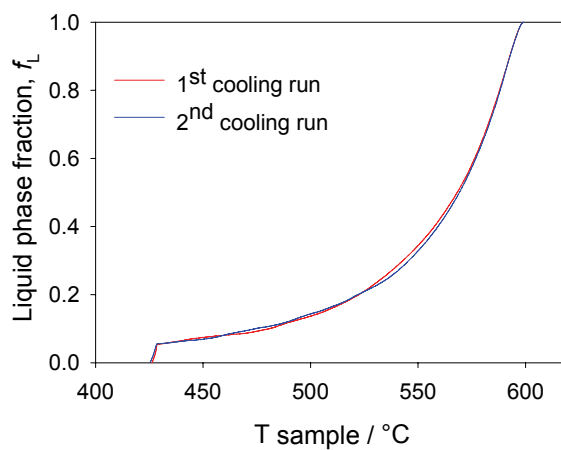


Figure 2.9b. DTA-HTM calculated solidification curves, reflecting the variations of Fig. 2.9a

### 2.4.3 Different samples and capsule design

The further diversification of the experimental conditions was made, having the signals of the AZ91Mn alloy at 5 K/min, but recorded during three different measurements each having different samples of the studied alloy (**Fig. 2.10a**). These measurements were furthermore performed in two different experimental set ups, applying different Ta-capsule designs and sample holders. The optimized capsule design (Fig. 2.1) has been used to measure samples 1 and 2, while the previous deep-drawn Ta-capsule has been applied for sample 3. The new designed capsule has been optimized especially regarding to aspects of reliability and

handling, even though the base line appears to be less stable in this example. **Fig. 2.10b** shows calculated solidification curves reflecting these variations.

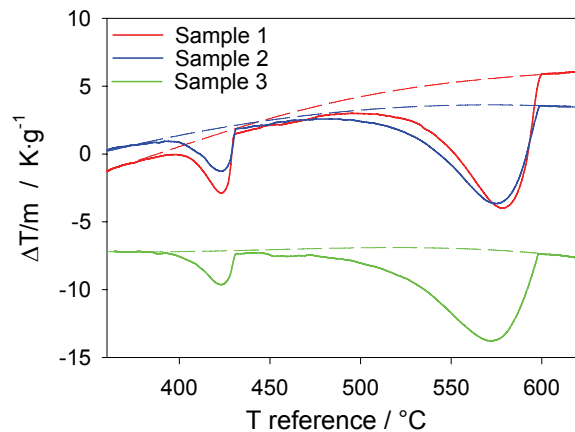


Figure 2.10a. The DTA signals of the AZ91Mn alloy at 5 K/min cooling rate recorded during three measurements. The sample 3 was measured by a different experimental set up.

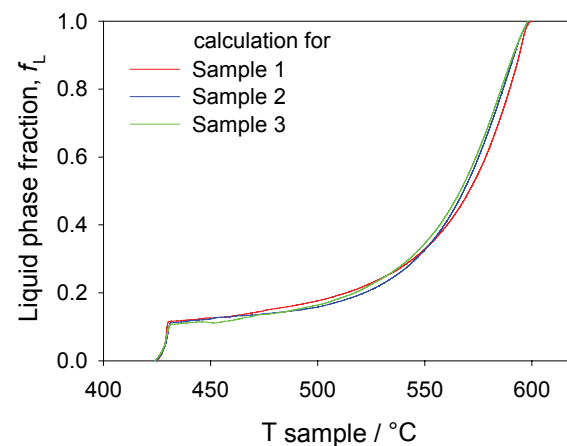
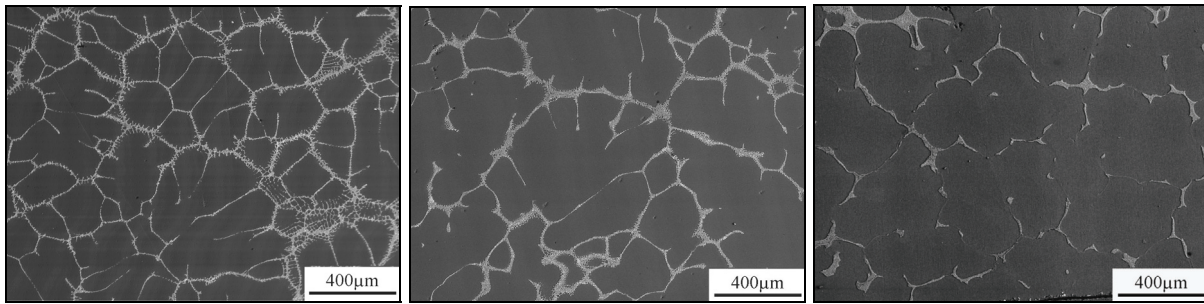


Figure 2.10b. DTA-HTM calculated solidification curves, reflecting the variations of Fig. 2.10a

## 2.5 Alternative determination of solidification curves and comparison with DTA-HTM data

### 2.5.1 Quenching and Image Analysis (QIA)

For each of the AZ91Mn, AZ91 and AZ62Mn alloys the three separate samples were experimentally studied using the conventional QIA technique. Each sample was encapsulated in a thin-wall mild steel tube (outer diameter 6 mm, 0.5 mm wall thickness, length 100 mm), held at 650°C for 1 hour, slowly cooled in furnace with controlled cooling rate of 2 K/min down to a preset temperature  $T^*$  in the (Liquid+Solid) range and subsequently quenched into liquid nitrogen (LN<sub>2</sub>). In separate experiments  $T^*$  was selected to be 550, 500 and 450°C. As an example the microstructure of an AZ91Mn alloy after quenching from the three different temperatures in the freezing range is shown in **Fig. 2.11**. The bright regions correspond to liquid prior to quenching, while dark regions show the slowly grown Mg-solid solution crystals. The area fractions determined by quantitative image analysis are shown as symbols in **Fig. 2.12**. The area fractions are considered to be approximately the same as the molar phase fractions for the sake of comparison to the calculated solidification curves.



a)

b)

c)

Figure 2.11. Microstructure (BSE) of an AZ91 alloy partially solidified at a cooling rate of 2 K/min from 650°C to  $T^*$  and subsequently LN2-quenched from a)  $T^* = 550$ ; b)  $T^* = 500$  and c)  $T^* = 450$ °C.

The bright regions show the initially liquid phase prior to quenching.

### 2.5.2 Thermodynamic calculation of the solidification curves

Solidification curves of the magnesium alloys were calculated applying two limiting solidification models (equilibrium and the Scheil solidification models) [1998Kur]. The resulting curves are presented in Fig. 2.12 as dash-dotted lines (Scheil model) and dash lines (equilibrium solidification). All calculations in this work have been done with the PANDAT software package [2001Che] and are based on the Mg-Al-Zn-Mn subsystem of the larger thermodynamic database for magnesium alloys developed in our group [2001Sch].

## 2.6 Discussion

The heat-transfer model applied in this work implies only the first time constant  $\tau_1$ . It means that a heat flow resistance between temperature sensor (thermocouple) and the sample/reference material is neglected ( $R_2 = 0$ ). That implies the assumption of zero temperature difference between sample/reference material and corresponding thermocouple ( $T_S = T_{MS}$  and  $T_R = T_{MR}$ ). One should be aware of the limitations in desmearing ability of the proposed model caused by this simplifying assumption. Clearly, this assumption is more adequate for the cases where the thermocouple is directly immersed in the sample. However, in this work the thermocouple is mounted externally at the bottom of the Ta-capsule. For two reasons it is supposed that this simplification does not crucially affect the desmearing quality of presented model: Firstly, good adhesion between sample and the inner side of the capsule bottom was always observed in this study. Secondly, tantalum is known as good heat conductor and the wall thickness of capsule bottom was chosen as thin (0.25 mm) as possible.

Without using the second time constant  $\tau_2$ , the current approach does not lose considerably in accuracy but is remaining suitably simple for application.

The following discussion will be focused on the critical analysis of the own results obtained using DTA-HTM and a comparison to different techniques for the determination of the solidification curves.

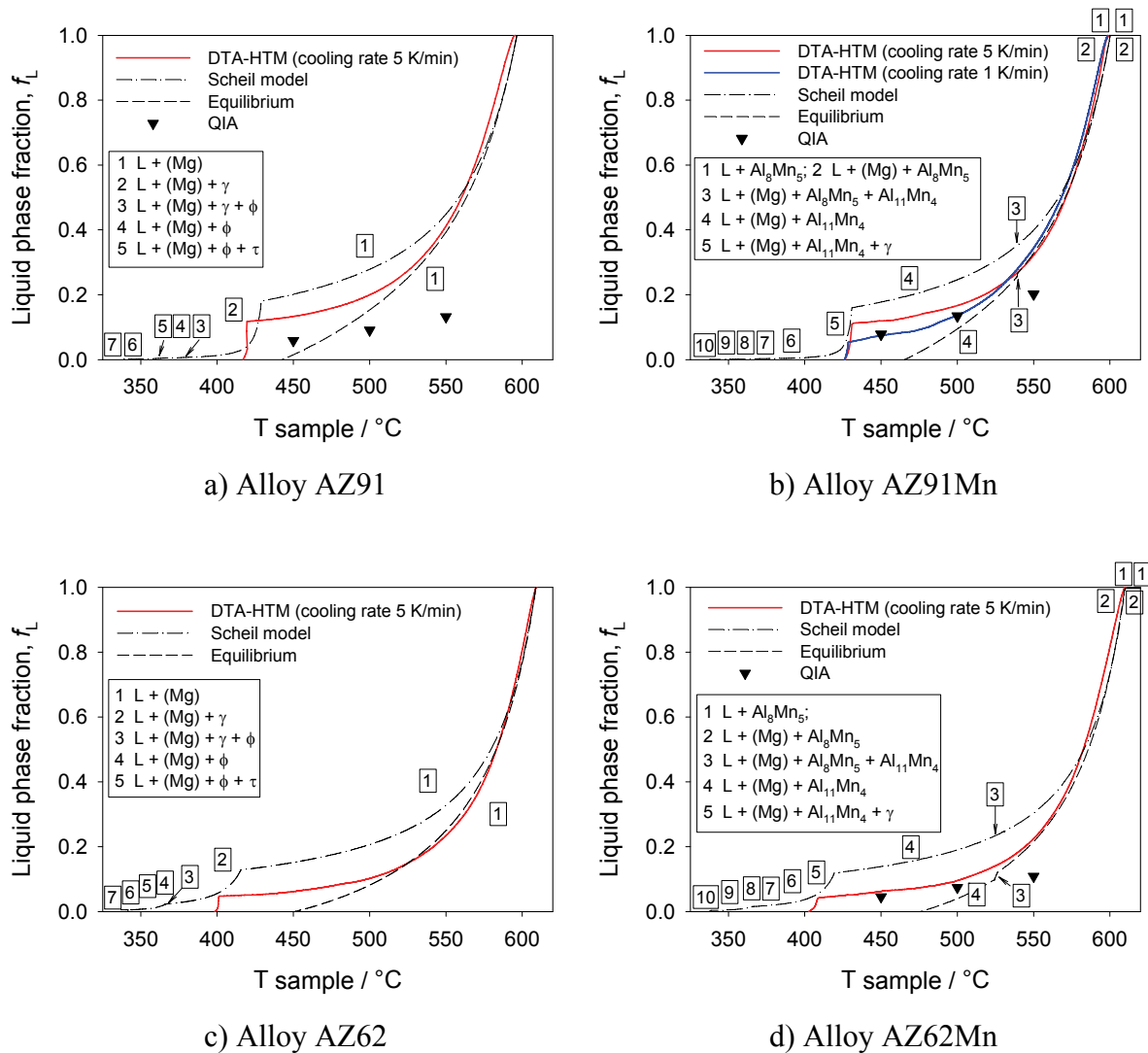


Figure 2.12. Solidification curves of the a) AZ91, b) AZ91Mn, c) AZ62 and d) AZ62Mn

alloys are determined in this work by using three different methods

(i) DTA-HTM, (ii) Scheil and equilibrium calculations, and (iii) QIA.

Phases appearing in the first five solidification steps from Scheil calculation are labeled.

### 2.6.1 Conventional thermal analysis compared to DTA

As stated by Riddle et al. [2003Rid], the conventional thermal analysis (TA) is a sensitive, rapid and inexpensive technique, compared to the DTA and particularly to the delicate DSC apparatus. In addition to the negligible cost for the apparatus, the major advantage of TA for Mg-alloys is that the evaporation or reactivity of the sample with subsequent damage of a delicate apparatus is not a concern. In contrast, there is a need to encapsulate the Mg alloy sample in DTA or DSC measurements in order to obtain reproducible results, based on our experience.

The basic problem of TA is still the same as already encountered by Bäckerud et al. [1986Bac, 1988Tam]. This is the reliable determination of the base line, which must be subtracted from the first derivative of the cooling/heating curves prior to further processing by heat-transfer model or a simple integration. In TA the base line is even more difficult to determine compared to DTA, not to speak of DSC, because the derivative rather than a directly measured signal has to be processed. Two widely accepted methods for calculating the base line in TA are Newtonian [1984Che] and Fourier [1993Fra]. Even though, the determination of base lines for TA remains highly subjective, derogating the accuracy of the provided solidification curves.

Beside the base line determination, wrong treatment of the measured TA cooling curves collected from complex shaped castings in comparison to simply shaped test cups could also provoke significant error [2005Dio]. This is particularly valid if only one thermocouple is used. The migration of the solidification front with respect to the thermocouple and the possible displacement of the thermocouples in complex shaped castings due to thermally induced stresses are other phenomena shown to have strong significance on the quality of the measured TA cooling curves.

### 2.6.2 Relationship between QIA and DTA-HTM solidification curves

In all cases the QIA results show a lower fraction of liquid compared to the DTA-HTM solidification curves as given in Fig. 2.12a, b and d. The biggest difference can be recognized at highest quenching temperature (550°C). This is explained by a systematic deficiency of the QIA method to actually freeze-in the liquid. Even with the attempted very high cooling rate in our experiments (using thin-wall sample container, small sample diameter and liquid nitrogen quenching medium) it was not possible to get immediately quenched microstructure for the given temperature. The main reason is that the heat of solidification generated within the sample provides a shield against quenching. As a result the additional growth of the large

---

primary crystals present at the quenching temperature could not be prevented. This buildup cannot be distinguished from the already present solid phase and, thus, an overestimation of the fraction of solid (or underestimation of  $f_L$ ) is unavoidable, especially when quenching from higher temperature. This observation on Mg-alloys is supported by the same trend observed for aluminum alloys [1995Jen, 1996Che1]. **Fig. 2.13** shows a comparison of the own work to the experimental QIA results of Lohmüller et al. [2003Loh] and Saito et al. [1997Sai] for alloy AZ91Mn. The solidification curves obtained from DTA-HTM and the thermodynamic calculations are the same as shown separately in Fig. 2.12b for the sake of clarity. This comparison demonstrates a general agreement but also the substantial error margin of the QIA method has been revealed in the detailed work of Saito et al. [1997Sai]. In addition to this inaccuracy the QIA method is very labor intensive and time consuming, operator subjective in the image analysis part and, thus, not attractive.

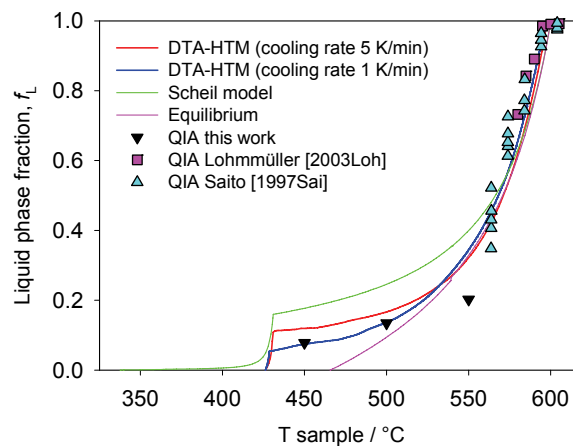


Figure 2.13. Comparison of the solidification curves of the alloy AZ91Mn shown in Fig. 2.12b to the experimental QIA results of Saito et al. [1997Sai] and Lohmüller et al. [2003Loh].

### 2.6.3 Relationship between thermodynamic calculations and DTA-HTM solidification curves

The non-equilibrium (Scheil) and equilibrium solidification model simulate two limiting cases of the solidification process. Owing to the limiting assumptions for these two models the solidification curve of a real solidification process is expected to be placed between those calculations. The measured DTA-HTM solidification curves in Fig. 2.12 support this expectation. For the AZ91Mn alloy solidification curves for both 1 and 5 K/min cooling rates



are shown in Fig. 2.12b. According to expectation, the solidification curve based on the lower (1 K/min) cooling rate shows less secondary phase amount and it is also closer to the calculated equilibrium curve. It is furthermore in good agreement with the QIA data at 450 and 500°C. All this evidence suggests that the DTA-HTM provide a reasonable description of the actual solidification process, which is at least qualitatively closer to the Scheil than to the equilibrium model.

More accurate than the Scheil model are the so-called micro-models [1998Kur] as detailed by Boettinger and Kattner [2002Boe] or by Xie et al. [2003Xie]. However, in addition to the complete thermodynamic description of the alloy system these micro-models require additional kinetic and thermophysical parameters. It is then possible to calculate also the enthalpy-temperature relation with higher accuracy using solute-diffusion. Dong et al. [2003Don] also claim the necessity to use microsegregation models to obtain solidification curves on the basis of heat evolution measurements.

The results from this work are in complete agreement with this suggestion to use micromodels for a detailed description if all the thermodynamic and kinetic data are available. The crucial point of the present work is to demonstrate that even without knowing any of these data it is possible to determine the solidification curve of a given Mg-alloy using the DTA-HTM method. This is also important in order to provide independent experimental information in order to check more sophisticated microsegregation solidification models of such alloys. Additional work is needed to apply this promising technique to other Mg-alloys and to further improve the model, for example the assumed linearization of the heat evolution and other aspects.

#### 2.6.4 Influence of the Mn addition

Within the uncertainty of measurement no difference in extracted DTA onset temperatures between alloys with and without Mn addition was observed. That is, even DTA cannot recognize the minute amount of  $\text{Al}_8\text{Mn}_5$  phase that is predicted by thermodynamic calculation to precipitate above the (Mg) solidification. That phase is only visible in the microstructure comparison, showing needle like  $\text{Al}_8\text{Mn}_5$  precipitates in the microstructure of alloys containing Mn. As example, the microstructure of the AZ91Mn sample solidified at the 1 K/min cooling rate is shown in the Fig. 2.7. The comparison of the DTA-HTM cooling curves of the corresponding samples without/with Mn in Fig. 2.12a/b and Fig. 2.12c/d also show no substantial impact of the Mn addition.

---

### 2.6.5 Reliability of the DTA-HTM solidification curves

The Figs. 2.8b, 2.9b and 2.10b show that DTA-HTM is able to provide sufficient reliability concerning the determination of the solidification curves. The largest observed deviation is below 5 %. It is obvious that these curves are obtained in a repeatable way from different DTA signals even though the DTA signals may look quite different, comparing different runs of the same sample (Fig. 2.9b) or even different samples (Fig. 2.10b). The high reproducibility of the DTA-HTM is evidenced in Fig. 2.10b, where even the strong alteration in the experimental set up (different samples and crucible design) does not provoke major changes of the solidification curves.

It is worth noting that the highest deviation is caused by the alteration of the base line (Fig. 2.8b). This stresses the importance of a reliable base line construction if DTA curves are used for determination of the solidification curves. Room for further improvement is in the use of advanced equipment (DSC). Generally, DSC provides a more stable base line than DTA, which will diminish the impact of base line fitting. As mentioned above, the conventional TA is even more handicapped, because the base line construction is even more uncertain compared to DTA.

Finally, it should be emphasized that the termination of solidification is typically assigned to the maximum of last peak of the DTA signal. This is a subjective assignment that has to be made before the HTM procedure can be performed. The possible error may not be so large in the present work with well encapsulated samples that allow repeated DTA runs and a comparison of the maximum assigned at the different DTA versus time signals. The corresponding temperatures, indicating the termination of solidification ( $t = t_S$  or  $T = T_S$  with  $f_L(T_S) = 1$ ) in Figs. 2.8b, 2.9b and 2.10b are not visibly different from each other for a given alloy. It is also interesting to note that this termination of solidification indicated in the DTA-HTM curves is sharper compared to the Scheil calculation in Fig. 2.12.

---

## 2.7 Conclusions

Solidification curves of magnesium alloys are determined by the processing of the DTA-measured signals with a heat-transfer model (HTM) based on the Tian equation. It is crucial to measure the temperature dependence of the time constant independently. Another important progress was made in the optimization of the tantalum encapsulation of the Mg alloy sample, indispensable for generation of reproducible and reliable data.

Reproducibility of these DTA-HTM solidification curves was checked by variation of three major experimental conditions or parameters. The largest impact is due to different base line fitting, whereas different cooling runs or different samples and capsule design result in similar solidification curves despite rather different DTA signal shapes.

The solidification curves are compared with those measured tediously by using quenching and image analysis and also with those calculated by limiting solidification models (equilibrium solidification model and Scheil model). The results indicate a potential of this DTA-HTM method for simple, fast and reliable determination of solidification curves even for highly reactive alloys. It is a truly independent method and does not rely on the knowledge of thermodynamic, kinetic or thermophysical alloy parameters, which are usually very difficult to provide for magnesium alloys.

---

### 3 Solidification curves determined from DSC with improved heat-transfer modeling

#### 3.1 Introduction

As has been remarked in Chapter 2, a detailed understanding of the solidification process is crucial for establishing desired final cast component properties. In the previous Chapters the term “solidification curve” of an alloy has been introduced. A detailed review of the different methods to determine solidification curves has been given in section 2.2.

In this study a differential scanning calorimetry (DSC) measurement with a mathematical heat-transfer model (HTM) is proposed as an *in-situ* method for providing solidification curves; its validity is checked by application to the AM50, AZ31, AZ61, AZ62 and AZ91 commercial magnesium alloys. The selected alloys cover a wide range of typical applications such as rolling (AZ31), extrusion (AZ61), sand casting/welding wire (AZ62) and die casting (AM50 and AZ91). The alloys denoted as AZ61, AZ62a and AZ91a with reduced Mn content (in addition to those denoted AZ62b and AZ91b) are also studied in order to investigate the effect of Mn on the alloy solidification path. Next to determining solidification curves for this wide range of Mg alloys a main purpose of this work is to introduce a new method of desmearing involving the independent determination of a time constant as a function of temperature for the applied equipment. A further improvement is achieved through a more impartial interpretation of the measured DSC curves, where the termination of solidification is not being artificially defined by the operator. It is also shown that an improved Ta-capsule design including a dependable sealing method enables reliable and reproducible DSC measurements needed for the DSC-HTM approach, even for the very demanding magnesium alloys. The question of reproducibility and reliability of the resulting DSC-HTM solidification is also addressed.

#### 3.2 DSC Experiment and Heat-Transfer Model (DSC-HTM)

##### 3.2.1 DSC experiment

The chemical compositions of the seven magnesium alloys denoted as AM50, AZ31, AZ61, AZ62, AZ62b, AZ91a and AZ91b in this Chapter are shown in **Tab. 3.1**. Three master alloys, specified as AM50, AZ61 and the AZ91HP are provided by Norsk Hydro Magnesiumgesellschaft mbH, Bottrop, Germany, while the AZ31 master alloy is provided by

---

Dead Sea Magnesium Ltd., Israel. The experimental samples denoted AM50, AZ31, and AZ91b were cut from the delivered master alloys, the notation AZ91b refers to AZ91HP.

**Table 3.1.** Chemical composition [wt.%] of the investigated alloys, balance Mg.

Notation	Al	Zn	Mn	Si	Fe	Cu	Ni	Be
AM50	<b>4.63</b>	<b>0.035</b>	<b>0.280</b>	0.019	0.0032	0.0042	0.0004	0.0005
AZ31	<b>2.85</b>	<b>1.05</b>	<b>0.230</b>	0.012	0.0034	0.0037	0.0002	0.0005
AZ61	<b>6.24</b>	<b>0.50</b>	<b>0.019</b>	0.017	0.0213	0.0019	0.0005	-
AZ62a	<b>5.61</b>	<b>1.70</b>	<b>0.011</b>	0.013	0.0229	0.0026	0.0004	-
AZ62b	<b>6.61</b>	<b>1.32</b>	<b>0.240</b>	0.013	0.0021	0.0028	0.0004	0.0005
AZ91a	<b>9.43</b>	<b>1.21</b>	<b>0.064</b>	0.032	0.0062	0.0014	0.0075	0.0001
AZ91b	<b>8.67</b>	<b>0.63</b>	<b>0.210</b>	0.020	0.0062	0.0042	0.0005	0.0004

Alloys with virtually no manganese (AZ61, AZ91a and AZ62a in Tab. 3.1) were prepared using following pure materials: Mg bars, min 99.9 wt.% provided by Norsk Hydro Magnesiumgesellschaft mbH, Bottrop; Al bars, 99.98 wt.% produced by Hydro Aluminium High Purity GmbH, Grevenbroich and Zn rods, 99.98 wt.% obtained from the Harzer Zink GmbH, Goslar, all purities referred to metal basis. The starting material for each alloy was weighted, melted and held for 10 minutes at 750°C in a stainless steel crucible with protection by mixture of 0.4 vol.% SF<sub>6</sub> and 3 vol.% Ar in air. The sample was homogenized by mechanical stirring and, then, the melt was cast in a cold heavy steel mold. The typical as-cast mass was 2 kg. The compositions of prepared alloys were analyzed in our chemical laboratory using ICP-AES (Inductively Coupled Plasma Atomic Emission Spectroscopy). The AZ62b alloy was melted under the same conditions by adding high purity Zn to the AZ61 master alloy.

The error caused by the segregation in this relatively large ingot was minimized by machining both the DSC and ICP-AES samples from the same area of the ingot. This location in the as-cast ingot is shown in **Fig. 3.1**. By following this procedure a good correlation between the DSC-HTM solidification curves and those calculated using the actually analyzed chemical compositions was maintained.

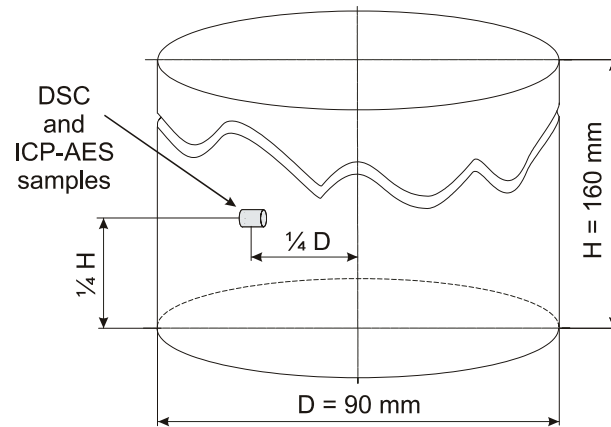


Figure 3.1. Schematic location of the DSC and ICP-AES samples taken from the as-cast ingot. The sample was lathed to a cylinder with a 5.8 mm outer diameter; an 8 mm high section of the cylinder was taken for the DSC sample, the rest was used for the ICP-AES sample.

The DSC measurements were performed using Setaram MHTC 96 DSC equipment (SETARAM Instrumentation, Caluire, France). This is a cylinder-type heat flux measuring system with thermally-coupled sample containers. The temperature and caloric calibrations are performed using high purity Ag, Cu, In, Mg and Pb metals. Both temperature and caloric calibration are performed in the heating mode. This assumes symmetry of the heat transfer phenomena on heating/cooling, which is generally accepted for the heat flow DSC [1996Hoe]. Furthermore, this assumption was experimentally checked with indium, selected as a substance with small and well-defined supercooling effects ( $< 2$  K). Even in that low temperature range, around 150 to 160°C, which is quite low for the present high temperature calorimeter, satisfactory symmetry was observed in heating and cooling cycles. The temperature and caloric calibration procedure of our scanning calorimeter follows the detailed procedures given by Sarge et al. [2000Sar].

Helium at 2 l/h flow rate has been used for the analysis chamber gas. In previous work [2003Mir, 2006Mir] the necessity for applying an inert and sealed sample crucible, i.e. a capsule, was recognized due to a high oxygen affinity and vapor pressure of the studied Mg-alloys. This was indispensable in order to obtain reproducible and reliable data. Non-tight crucibles, simply closed or covered by a lid, are rejected due to sample evaporation, as observable in the work of Lindemann et al. [2002Lin]. An experimental set up for reactive alloys, based on stainless steel capsule with a crimped seal and a graphite casing fitted inside the capsule, is commercially available from the manufacturer Setaram. This crucible design was not used in this work mainly due to a likely reaction between the sample and crucible; the formation of aluminum carbide had been observed between a graphite crucible and Al-

containing Mg alloys [2002Lin]. The relatively low volume of the graphite casing (30  $\mu\text{l}$ ) is an additional disadvantage of the commercial encapsulation, encouraging the authors to develop and optimize their own sealed Ta capsule (**Fig. 3.2a**), adapted to the MHTC96 DSC. The sample- and reference Ta-capsules inserted in DSC sensor are shown in **Fig. 3.2b**. An additional advantage of the tantalum capsule is the reduction of heat flow resistance between furnace and sample. This is because it is from mono-material tantalum and that design eliminates any transition resistances within the crucible wall, such as that between stainless steel wall and graphite casing. The selection criteria for choosing tantalum as capsule material are discussed in detail in section 2.3.1.

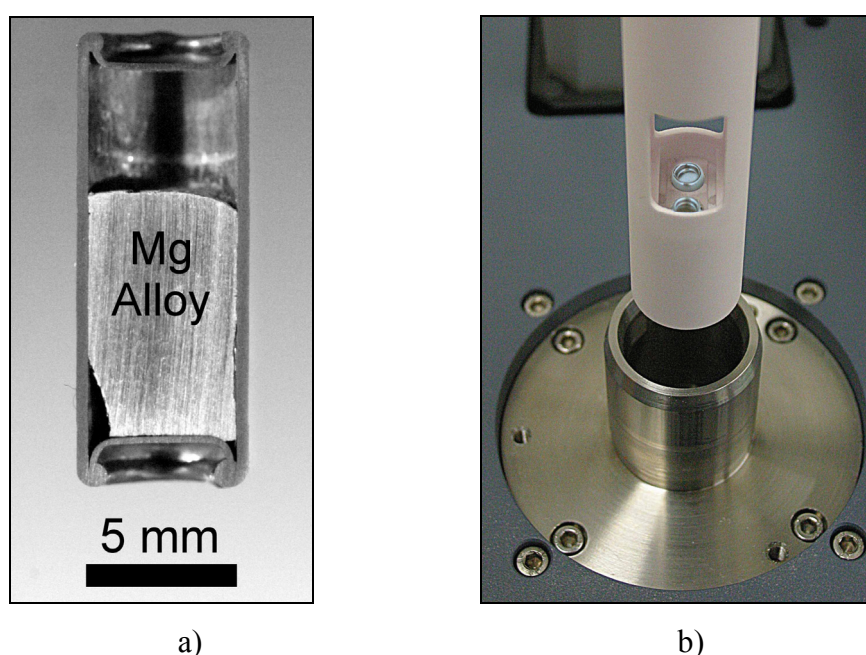


Figure 3.2. a) Cross-section of the optimized Ta-capsule filled with AZ31 sample material after being measured by DSC;  
b) MHTC96 DSC sensor with inserted sample and reference Ta-capsules

The Ta-capsules were produced in our lab by using Ta tube with a 6.7 mm outer diameter and a 0.4 mm wall thickness and Ta sheet for capsule lid and bottom with a thickness of only 0.25 mm, both with a purity of min. 99.9 wt.% (metal basis), by Plansee GmbH, Reutte, Austria. The sample Ta-capsules were filled up to 50 vol.% with the sample material and sealed under argon with 0.5 bar over pressure by electric arc welding. The average empty Ta-capsule weight was  $2950 \pm 30$  mg, and the typical sample weight was about 400 mg (cylinder  $\text{\O} 5.8$  mm; height approximately 8 mm). The reference Ta-capsule was also sealed by welding, and a sapphire cylinder was used as reference material. The sapphire mass was

492.5 mg, which is a good balance for the heat capacity of the sample. Both, the encapsulated sample and reference materials were placed approximately in the middle of the DSC-transducer cell height, as this is the most sensitive zone. The scanning program comprised cycles 150 - 700 - 150°C at heating/cooling rates of 1, 2, 3 and 5 K/min. For each alloy composition two independent samples were studied and two or three heating/cooling cycles were performed for each sample. The overall uncertainty of DSC measurements was estimated as  $\pm 3$  K for temperature determination and  $\pm 0.3$  kJ/mol for caloric measurements.

### 3.2.2 Heat-transfer model (HTM)

#### 3.2.2.1 Desmearing of the DSC signal

In this work the heat-transfer model based on the Tian linear first-order differential equation is applied to desmear recorded DSC curves and to simulate the heat transfer between the DSC cells and the furnace during solidification of the sample. A more detailed description of the model, comparing various assumptions, is given elsewhere [1968Gra, 1989Hem, 1996Hoe]. A schematic diagram of the applied DSC equipment is shown in **Fig. 3.3** and the corresponding HTM quantities are summarized in the **List of symbols**.

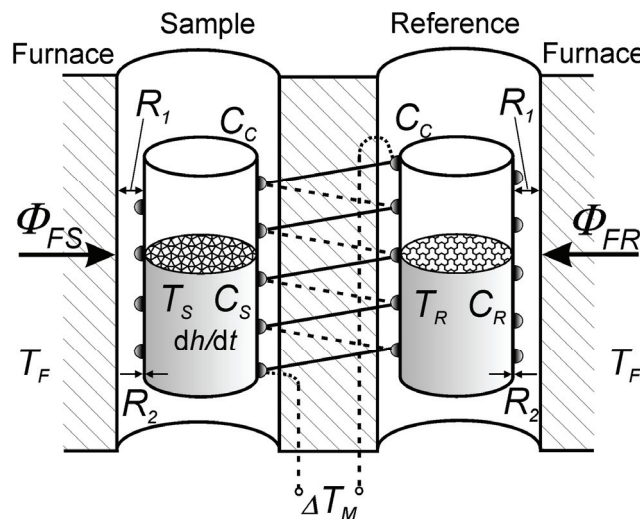


Figure 3.3. Schematic view of the DSC, with quantities used in heat transfer model.

The sample and reference cells are depicted, both consisting of sample/reference material and crucible. The sample ( $T_S$ ) and reference ( $T_R$ ) temperatures are taken to be uniform inside the sample/reference material. In the first approximation they are also taken to be equal to those of actually measured temperatures at the corresponding thermocouple tips ( $T_{MS}$  and



$T_{MR}$ ). The heat flow ( $\Phi_{FS}$  or  $\Phi_{FR}$ ) between the furnace at temperature  $T_F$  and the sample/reference crucibles, respectively, has to overcome the corresponding heat flow resistance ( $R_1$ ). Based on the symmetry of the DSC equipment, this heat flow resistance is considered to be equal for both cells. The heat exchange between the sample and reference cells is neglected.  $\Delta T_M$  is the temperature difference between the reference and sample thermocouples. This is the only directly measured quantity during the DSC experiment, besides  $T_{MR}$ . A heat flow signal  $\Phi_M$  is internally assigned to the temperature difference  $\Delta T_M$  according to the calibrating function, already defined by the caloric calibration described above.

The heat generated in the sample cell per unit time,  $dh/dt$  is considered as positive and heat absorbed as negative. This heat generated by exothermic or endothermic reaction inside the sample cell implies a heat flow  $\Phi_r$ , which is expressed by Eq. (3.1):

$$\Phi_r = \frac{dh}{dt} \quad (3.1)$$

The heat balance of the sample cell during the solidification of a sample, based on the principle of energy conservation, can be expressed by the following equation:

$$\Phi_r + \Phi_{FS} = (C_S + C_C) \frac{dT_{MS}}{dt} \quad (3.2)$$

That means that the sum of the heat flow generated inside the sample during solidification ( $\Phi_r$ ) and the heat flow arriving from the environment ( $\Phi_{FS}$ ) increases the temperature of the sample ( $T_S = T_{MS}$  in the present first approximation). The heat capacity of the thermocouple wires is neglected. The equivalent equation for the reference cell can be expressed as follows:

$$\Phi_{FR} = (C_R + C_C) \frac{dT_{MR}}{dt} \quad (3.3)$$

as no heat  $h$  is generated in the reference cell. The heat capacities of the sample and reference crucibles are considered to be equal for both cells ( $C_C$ ). In analogy to Ohm's law, the furnace-to-cell heat flows can be written as:

$$\Phi_{FS} = \frac{T_F - T_{MS}}{R_1} \quad (3.4a)$$

$$\Phi_{FR} = \frac{T_F - T_{MR}}{R_1} \quad (3.4b)$$

The heat capacities of both reference and sample cells require special consideration. Here the heat capacity of the sample material,  $C_S$ , is approximated by that of pure Mg. It can be calculated that the heat capacity of the reference cell ( $C_R + C_C$ ) amounts to approximately 1 J/K over the solidification range of the studied alloys (1.08 J/K at 650°C and 0.98 J/K at

300°C). The heat capacity difference between the reference substance (sapphire) and the sample ( $C_R - C_S$ ) is smaller than 0.1 J/K (98 mJ/K at 650°C and 82 mJ/K at 300°C) over the solidification range and thus virtually temperature independent. This difference represents the base line displacement from the zero signal level of heat flow and should appear in an additional term  $(C_R - C_S) dT_{MR}/dt$  on the right side of the final Eq. (3.5a) shown below. The remaining displacement of the DSC signal curve is corrected by a base line subtraction without making significant error. This is because  $(C_R - C_S)$  is virtually temperature independent in our case and thus a mathematical base line can be easily determined.

Subtracting Eq. (3.3) from Eq. (3.2), and rearranging according to the first time derivative of the Eq. (3.4a), the following expression is obtained, following the approach of Gray [1968Gra]:

$$\frac{dh}{dt} = \Phi_M + \tau_1 \frac{d\Phi_M}{dt} \quad (3.5a)$$

with

$$\tau_1 = R_l (C_S + C_C) \quad (3.5b)$$

Here  $\Phi_M$  is the measured, smeared heat flow between the reference and sample thermocouples, generated mostly through the heat evolved during solidification of the sample. Here and in the following it is assumed that the base line, typically measured with an empty crucible, is already subtracted in the quantity  $\Phi_M$ , and, in addition, the remaining displacement is corrected by subtracting a polynomial fitted base line. This corresponds to the assumed equal heat capacities of the sample and reference cells,  $C_R \approx C_S$ , in Eq. (3.5).

In contrast to this quantity  $\Phi_M$ , measured during the DSC experiment, the term  $dh/dt$  is a desmeared heat flow, where the smeared DSC signal is corrected using the term  $R_l (C_S + C_C)$ . This term is commonly marked as  $\tau_1$  and named the first time constant, as it is usually the largest time constant characteristic for the temperature balance between the furnace and the sample. If further refinement is wanted, the higher-order time constants ( $\tau_2, \tau_3 \dots$ ) could be involved, as discussed later. The first time constant  $\tau_1 = R_l (C_S + C_C)$  is defined by the heat flow resistance between the furnace and the sample thermocouple and the heat capacity of the sample cell (sample and crucible together). Even though it involves the sample property  $C_S$ , it is essentially characteristic for the DSC equipment and depends on experimental set up such as crucible design and materials. This is also related to the approximation  $C_R + C_C \approx C_S + C_C$ .

### 3.2.2.2 Time constant determination

There are a number of different methods for determining the time constant  $\tau_l$  [1993UIb, 1994Loe]. In this work  $\tau_l$  was determined in independent experiments, using the solidification curves of pure metals measured under the same experimental conditions as the actual magnesium alloy samples. The signal decay from the inflection point after complete solidification was fitted to an exponential decay curve as shown in **Fig. 3.4** for the Mg freezing peak at a cooling rate of 5 K/min. The exponential function can be derived from Eq. (3.5a) since  $dh/dt = 0$  in that part of the DSC curve for a pure metal. In this study the solidification curve of the pure elements Pb, Mg, Ag and Cu were analyzed using the same conditions as those in the actual alloy experiments (same Ta-capsule setup, scanning rates etc.). The high fitting correlation coefficients (typically about 0.998) confirm the exponential decay as the correct function for heat flow modeling of the after-reaction part of DSC curves.

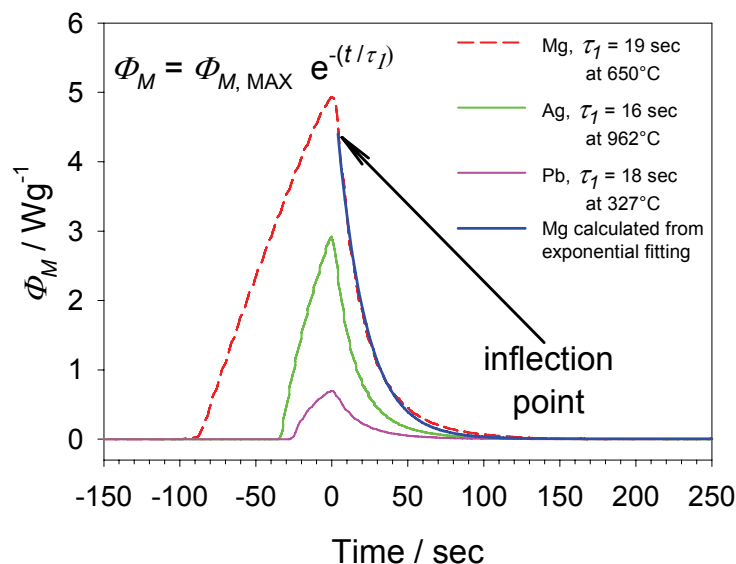


Figure 3.4. Experimental DSC freezing peaks of pure Pb, Mg and Ag at a cooling rate of 5 K/min. The pure Mg is compared with a calculated exponential signal decay. The weak temperature dependence of time constant  $\tau_l$  is noted.

The time constants obtained for the four metals at various heating or cooling rates are presented in **Fig. 3.5**. No significant dependence on the scanning rate is observed. The weak temperature dependence of time constant  $\tau_l$  is noted. For this reason in the present HTM-evaluation of the DSC cooling curves (measured in the range 150-700°C), a constant time constant value of 19 sec is assumed. A slightly decreasing time constant with increasing temperature (Ag, Cu) could be explained by the rising contribution of radiation to the heat transfer. A stronger temperature dependence of the heat resistance between the furnace and

the sample thermocouple might have been expected, as stated by Wiedemann and van Tets [1970Wie]. The weak temperature dependence, favorable in the present experiments, may be due to the high heat conductivity of helium, which is applied as the analysis chamber gas. That impact of the applied gas (argon or helium) to the time constant was studied separately by performing DSC measurements of gold in alumina crucible. The time constant determined in the case of argon (36 sec) was almost double to the value obtained in the case of helium (21 sec). It is also noted that the temperature dependence of  $\tau_I$  is much stronger for DTA equipment as compared to the present DSC equipment, as shown in a previous study on Ta-encapsulated Mg alloys using DTA (section 2.3.2.1).

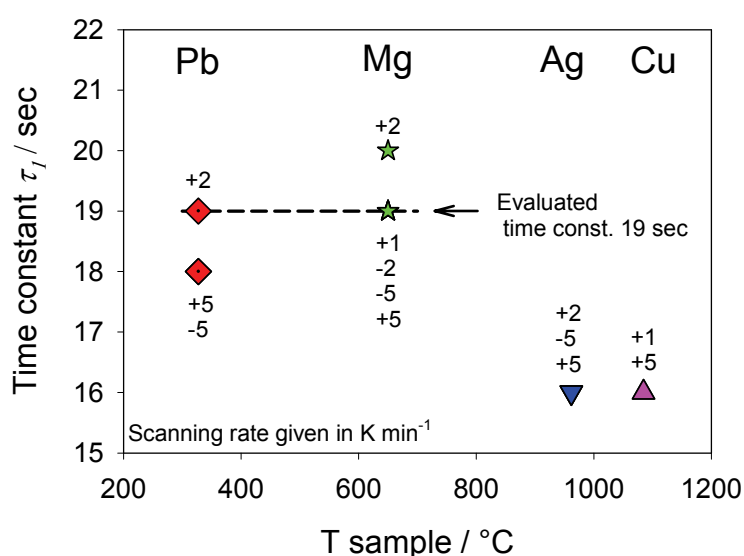


Figure 3.5. Time constants,  $\tau_I$ , calculated from exponential fitting to the DSC freezing peak decays of the pure metals used as calibrants. The numbers attached to each data point indicate the experimental heating (+) or cooling (-) rates in K/min. The constant value of  $\tau_I = 19$  sec, marked by a dashed line, is applied in the present HTM-study of the DSC cooling curves measured in the range of 150-700°C.

Another way to determine the time constant  $\tau_I$ , not in separate experiments but using the exponential tail of the last peak of the DTA/DSC curve of the actual alloy sample, is also found in the literature [1996Che1, 1998Che]. This becomes questionable in the case when an unknown alloy sample with unknown solidification path or potential solid state reactions could corrupt the results. A striking example for Mg alloys is given by Ohno et al. [2006Ohn1], for commercial AZ91 and AZ61 alloys where the “measured” solidus temperature (typically the lowest temperature peak on the DSC or DTA cooling curve) cannot

be associated with the end of solidification process. This thermal signal corresponds to the temperature at which the precipitation of  $\gamma$ -Mg<sub>17</sub>Al<sub>12</sub> phase *starts* under Scheil condition, thus the solidification process ends at a much lower temperature.

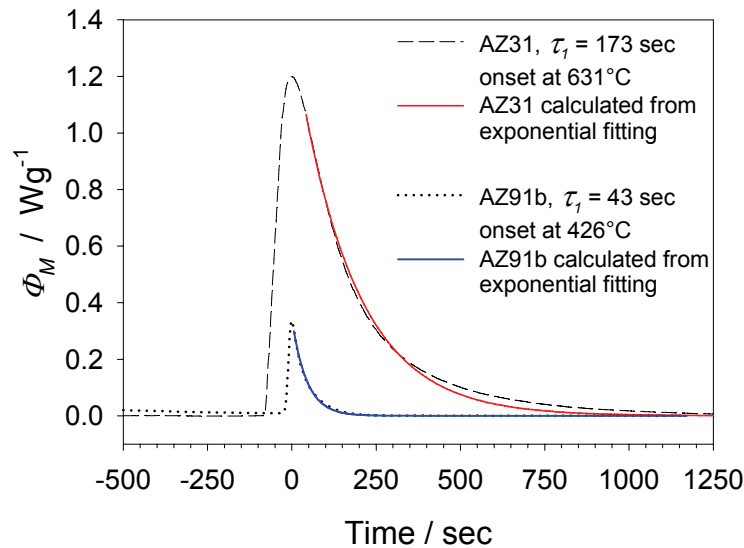


Figure 3.6. Experimentally obtained lowest cooling peaks during solidification of the AZ31 and AZ91b alloys at a 5 K/min cooling rate in the DSC. The superimposed calculated exponential signal decays indicate a poor fit and very high "time constants", demonstrating the inappropriateness of using the peak decay of these alloys for the determination of the time constant  $\tau_1$ .

It is demonstrated below that this intricate effect concerning the previously used time constant determination actually occurs in Mg alloys. The last peak on freezing of AZ31 alloy and also the low-temperature peak of AZ91b alloy are analyzed in this work, both at a 5 K/min cooling rate. For both peaks the "time constants" are calculated applying exponential decay fitting. Both DSC peaks and calculated exponential fittings are shown in **Fig. 3.6**. It is obvious that calculated "time constants" are significantly higher than those for pure metals. For the AZ91b alloy the "time constants" are found to be 43, 32 and 25 sec for -5, -3 and -1 Kmin<sup>-1</sup> cooling rates, respectively. For the AZ31 alloy, the "time constant" values of 173, 374 and 643 sec are found for -5, -2 and -1 Kmin<sup>-1</sup> cooling rates, respectively. It is also interesting that these "time constants" for alloys depend significantly on the scanning rate compared to the pure metals. Furthermore, the exponential decay fitting in Fig. 3.6 is a visibly poor approximation, compounded by significantly lower correlation coefficients compared to those for the pure metals. This implies that the release of the solidification enthalpy does not

end at the peak maximum, thus Eq. (3.5a) cannot be used with  $dh/dt=0$  for the last cooling peak tail of these Mg alloy samples.

It is interesting to note that the last heating peak tail of the AZ31 alloy can be fitted by an exponential curve. This is reflected by a relatively high correlation coefficient (0.9986) and the similar values for  $\tau_l$  constants for this alloy (23 sec) and pure Mg (19 sec). This observation is plausible since it is known [2006Ohn1] that for this alloy beyond the last heating peak only a very small heat consumption is expected due to the dissolution of the very small amount of primary phase ( $Al_8Mn_5$ ) before finally the homogeneous liquid alloy is attained.

The experimental findings detailed above indicate the significant advancement in the present method of determining the true values of the time constant  $\tau_l$  in separate experiments using pure metals and not the peak decay of an alloy sample with a freezing range and possibly complex solidification.

### 3.2.2.3 More details concerning the relationship between the enthalpy released during solidification and the liquid phase fraction

In section 2.3.2.2 a linear relationship between heat evolution,  $h$ , during solidification and liquid phase fraction  $f_L$  has been discussed. This linearization is mathematically expressed as:

$$dh = H df_s = H d(1-f_L) \quad (3.6)$$

where  $H$ , the total latent heat of solidification, is assumed to be a constant for each alloy composition. Since  $h(t)$ , as defined in Eq. (3.1), is also the cumulative amount of heat generated by sample reaction at time  $t$ , at the end of solidification we have  $h(t_{final}) = H$ . The time being related to the end of solidification ( $t_{final}$ ) will be discussed later.

This linear dependence is often considered as a very rough simplifying approximation. Dong et al. [2003Don1, 2003Don] claim that the accurate liquid fraction cannot be obtained directly using enthalpy measurements. They account this mainly to the presence of microsegregation, which induces enthalpy changes with composition that are of similar magnitude compared to the phase transformation. They argued that the direct relation of the solid fraction to the enthalpy data is only possible when there is no change in the average composition of the solid and liquid phases during transformation. Their conclusion is that the application of a microsegregation model should be the only way to accurately obtain solidification curves.

---

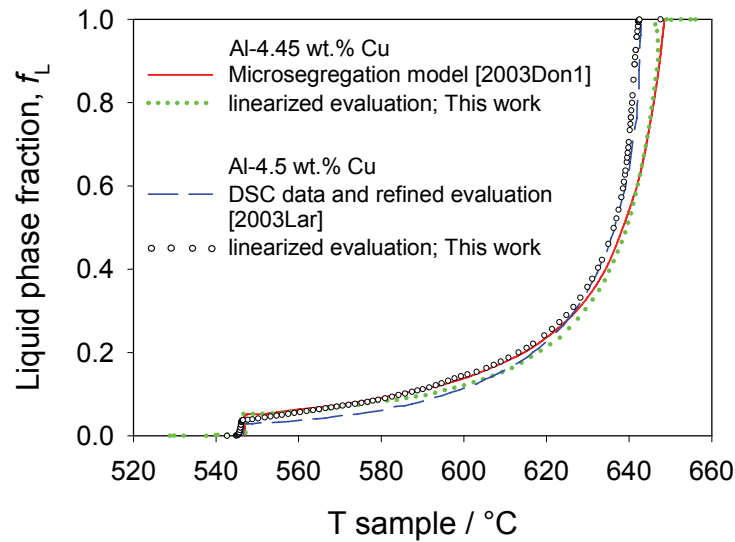


Figure 3.7. Solidification curves of binary Al-Cu alloys with 4.45 wt.% Cu [2003Don1] and 4.5 wt.% Cu [2003Lar] taken from the original works and compared with a linearized evaluation to demonstrate the impact of assuming a constant value of latent enthalpy  $H$ .

To scrutinize this statement, the solidification curves of the Al-4.45 wt.% Cu alloy are compared in **Fig. 3.7**, determined by two different approaches. The solid line on the graph is taken from Dong et al. [2003Don1] and was calculated using a multi-component microsegregation model linked with the thermodynamic data and software package MTDATA. The solid-dotted line is constructed by the present authors using directly the total enthalpy vs. temperature curve from the original experimental data from Dong et al. [2003Don1]. In doing this, it is necessary to curve-fit metastable extrapolations of the enthalpy of the single-phase liquid, supercooled below liquidus temperature, and the solid, superheated above solidus temperature; then, the measured total enthalpy of the alloy can be split into a latent part (enthalpy of solidification,  $h$ ) and a heat capacity contribution. At any temperature in the freezing range the distance between the liquid-extrapolation and the measured enthalpy curve equals  $h$ , and the distance between the liquid-extrapolation and the solid-extrapolation equals  $H$ . Using the simple linearized evaluation, Eq. (3.6) with a constant value of  $H$ , the solid fraction is given by  $h / H = f_s$ . This approach follows a detailed discussion of the basic problem of defining a unique value of  $H$  in the case of alloy solidification over a freezing range [2004Gro].

The quite good agreement between these two differently evaluated solidification curves shown in Fig. 3.7 is obvious. The biggest difference is observed in the  $0.1 < f_L < 0.3$  range of the solidification curve, while the early and final stages of the solidification show only minor

disagreements. This contradicts the presumption that the effect of microsegregation on the enthalpy change may be insignificant only in the early stage of solidification, while rising dissimilarity is expected towards the end of solidification [2003Don1]. The good agreement of the simple linearized evaluation with the microsegregation modeled curve is even more surprising, considering the complex solidification path of the Al-4.45 wt.% Cu alloy, where also nonequilibrium eutectic ( $\alpha$ -Al and  $\theta$ -Al<sub>2</sub>Cu) phases were observed in the microstructure.

It is emphasized that one prerequisite for this linearized evaluation is that the measured enthalpy data show negligible smearing. In fact, the experiment was performed [2003Don1] using a Smith-type single pan calorimeter, where a constant temperature difference is maintained between sample and its surrounding. The resulting enthalpy data can be accurately assigned to the sample temperature since this calorimetric technique features virtually no smearing. This is similarly true for the experimental work of Larouche et al. [2003Lar] on an Al-4.5 wt.% Cu alloy, due to the use of power compensated DSC equipment.

They [2003Lar] have also discarded the use of the linearized Eq. (3.6) with a constant value of  $H$ . Instead, the composition dependence of the molar enthalpy was considered with the solute concentrations of Cu in the solid and liquid phase calculated using a Brody-Flemings relationship. The heat flow differential equation for the specific set up of the power compensated DSC and the apparent heat capacity of the sample was then solved numerically in order to determine the solid fraction in the two-phase range. They employed very simplified thermodynamic literature data, assuming an ideal solution in both the liquid and fcc Al-Cu phases, whereas the liquid enthalpy of mixing is in fact strongly exothermic with a maximum value of -17.7 kJ/mol [1998Sau] instead of zero. Even though, they report a significant refinement of the liquid phase fraction at the end of the two-phase region, just before the eutectic. The resulting curve is shown in Fig. 3.7 as dashed line.

For comparison, the area defined by their originally measured DSC curve at 5 Kmin<sup>-1</sup> cooling rate was translated in this work without desmearing directly to the liquid phase fraction. For this calculation Eq. (3.7), given in the next section, was applied with the time constant value  $\tau_l$  set to zero in view of the negligible smearing in their set up. The result is shown in Fig. 3.7 as light-dotted line. No drastic disagreement is observed between the very simplified linearized evaluation and the more sophisticated evaluation [2003Lar]. Application of desmearing may further reduce the gap between those two curves. It is interesting that the disagreement is more pronounced in the temperature range between 620°C and somewhat above the eutectic, where the linearized evaluation yields about 4 % residual liquid instead of 3 %; this higher value was also noted before [2003Lar].

---



Since [2003Don1] and [2003Lar] studied binary Al-Cu samples with virtually the same composition, 4.45 and 4.5 wt.% Cu, respectively, both are plotted for comparison into the same Fig. 3.7. Both samples were also solidified at similar rates, -5 K/min [2003Lar] and about -5.9 K/min [2003Don1]. It is worth noting that a larger disagreement is observed between these two samples than between the present simple linearized evaluation of the original calorimetric data and the more sophisticated one for the same sample. We entirely agree with the statements of both [2003Don1] and [2003Lar] that the concentration variation of the liquid and solid phases during alloy solidification has a substantial impact on the *molar* enthalpy for the individual phases; both have plotted qualitatively similar pictures, showing that the gap between the enthalpy per mol of liquid phase and per mol of solid phase substantially narrows with decreasing temperature. However, we cannot follow the conclusion that this indicates a substantial decrease in the *latent* enthalpy  $H$ , since an isothermal transition between such a liquid and such a solid is not possible because of their different compositions.

This had been shown in more detail previously for the solidification of a ternary Al-Ce-Si alloy and the comparison of the calculated "latent enthalpy" with the DSC measurement [2004Gro]. It was made clear that the definition of a unique value of  $H$  is not possible for the alloy; however, the possible variation over the freezing range was in the order of the experimental calorimetric error. In essence, the assumption of a constant value of  $H$  may be acceptable. The only unique quantity is the total enthalpy (or heat evolution) of the alloy over the freezing range. Plotted as a function of  $f_L$ , a linear relation would be expected if  $H$  is constant, as seen from Eq. (3.6). That was actually shown to be the case with reasonable accuracy for the equilibrium solidification of the quaternary Mg alloy AZ91 [2006Mir], based on well validated thermodynamic data. For the solidification path calculated using Scheil's model the assumption of linear heat release is a rough approximation.

---

### 3.2.2.4 The present HTM-evaluation of experimental DSC data

The following equation is derived from Eqs. (3.5) and (3.6) by applying all simplifications written in the finite-difference form for numerical solution:

$$\Delta f_S = \frac{\Delta t}{H} \left[ \Phi_M(t) + \tau_1(T_{MR}) \left[ \frac{\Phi_M(t + \Delta t) - \Phi_M(t)}{\Delta t} \right] \right] \quad (3.7)$$

In the first step, before processing a measured DSC alloy curve with this desmearing function, the  $\tau_l$  values for all calibration metals were determined, thus providing the temperature dependence of  $\tau_l(T)$ . The  $\tau_l$  function should be checked after every calibration routine before being applied for desmearing of all DSC curves measured with the same experimental setup. In the next step, the base line has to be constructed for each measured DSC alloy curve. Depending on the used equipment and the kind of transformations occurring in sample, this might be difficult and may significantly increase the systematic uncertainty [1991Hem, 1996Hoe]. In the present setup of the Calvet-type calorimeter only a small correction of the baseline was necessary. Finally, the only remaining alloy-specific parameter in Eq. (3.7),  $H$ , is to be determined.

Now, another important novelty in the present approach is introduced; by contrast to Chen et al. [1998Che], no user-specific points on the DSC curve are selected to define start and end of solidification process. That is, the start point ( $t_0$ ) is set somewhat prior to the first onset and the end point ( $t_{final}$ ) somewhat after the last peak decay. At  $t_0$  and  $t_{final}$  the measured value  $\Phi_M$  clearly coincides with the baseline, the value of which was reset to zero. Between  $t_0$  and  $t_{final}$  the DSC alloy curve is further processed. This method reduces the operator's input to the base line construction and significantly minimizes the operator's impact on the final result. Especially, the difficult decision about an alleged end of solidification at the last peak maximum is avoided; the impact may be significant as demonstrated in the comparison of Figs. 3.4 and 3.6.

Numerical integration of Eq. (3.7) is performed once for the product  $Hf_S(t)$  starting from  $t = t_0$  with  $f_S(t_0) = 0$  until  $t = t_{final}$ , and, using  $f_S(t_{final}) = 1$ , the value of  $H$  is calculated. The final integration step thus yields  $Hf_S(t_{final}) = H$ . Knowing this constant we finally get  $f_L(t) = 1 - f_S(t)$  at any time  $t$  ( $t_0 \leq t \leq t_{final}$ ). It is noted that the desmearing used in Eq. (3.7) does not change the area under the DSC curve  $\Phi_M(t)$  compared to the desmeared quantity in the square brackets of Eq. (3.7), thus retaining the total released heat.

In previous work by Chen et al. [1998Che] the term  $H$  was obtained by simple computing of the peak area between the entire DSC curve and the constructed base line. The term  $\tau_l$  was then treated as an adjustable parameter determined from the measured DSC curve of *each* sample. An initial value of this  $\tau_l$  was obtained from the after-reaction part of the DSC curve, by fitting to an exponential decay curve for each sample. This value was further iteratively adjusted to meet the boundary condition  $f_S = 1$  at the maximum of the last peak, where the solidification was claimed to be terminated [1998Che]. We do not think it is justified to artificially proclaim that point (or any other with  $\Phi_M \neq 0$ ) on the curve as the end of solidification; the Mg alloy AZ31 exhibits significant ongoing solidification beyond that point, see Fig. 3.6. Furthermore, it is questionable to neglect the exponential tail of the last peak during such an iterative determination of the  $\tau_l$  constant. The total heat released should be related to the entire area including the exponential tail [1968Gra] even for pure metals, since the  $\Phi_M(t)$  signal is smeared. Otherwise significant errors are unavoidable if the last peak on the DSC cooling curve is large, such as in some of the present Mg alloy samples, or if the applied equipment is characterized by a longer time constant.

### 3.3 Results

#### 3.3.1 DSC-HTM analysis of important magnesium alloys

Results of the experimental DSC study and the proposed HTM evaluation of solidification curves are shown in mutually corresponding diagrams, (a) and (b), for the following commercially important Mg alloys, specified in Tab. 3.1: AM50 (**Fig. 3.8**), AZ31 (**Fig. 3.9**), AZ61 (**Fig. 3.10**), AZ62a (**Fig. 3.11**), AZ62b (**Fig. 3.12**), AZ91a (**Fig. 3.13**), and AZ91b (**Fig. 3.14**). The DSC cooling curves are shown at a cooling rate of 5 K/min in Figs. 3.8a-3.14a. Heating curves and other scanning rates are shown only for two alloys, AZ31 (Fig. 3.9a) and AZ61 (Fig. 3.10a), for the sake of clarity. The DSC cooling curves of the AM50 and AZ31 alloys exhibit only one strong peak during heating/cooling cycle, while two strong signals are clearly observed for all other alloys. The additional weak signals are difficult to see on the scale of Figs. 3.8a-3.14a.

---

**Table 3.2.** Temperatures and latent solidification enthalpies extracted from the DSC signals. Calculated equilibrium enthalpy data are also shown. Each heating/cooling signal is based on two different samples, at least two repeated cycles and two different scanning rates

Alloy	Thermal signal / °C			Solidification enthalpy / kJmol <sup>-1</sup>	
	Heating <sup>a)</sup>	Cooling <sup>b)</sup>	Evaluated temperature	Measured	Equilibrium calculation
AM50	624 s 434 w	622 s 435 w	623 435	7.3±0.3	7.78±0.06
AZ31	632 s 368 w	631 s not detect.	632 368	7.5±0.3	7.88±0.01
AZ61	612 s 433 s	611 s 426 s	612 433	7.3±0.3	7.32±0.03
AZ62a	612 s 416 s 366 w	611 s 406 s 351 w	612 416 366	7.0±0.3	7.29±0.08
AZ62b	608 s 424 s	608 s 416 s	608 424	6.9±0.3	7.27±0.02
AZ91a	592 s 431 s	591 s 424 s	592 431	6.4±0.3	6.77±0.05
AZ91b	600 s 433 s	600 s 426 s	600 433	7.1±0.3	7.02±0.02

a) Peak onset for invariant reactions, peak maximum otherwise

b) Peak onset

w = weak and diffuse signal

s = strong and clear signal

not detec. = not detected

All these peak temperatures are shown in **Tab. 3.2** and were extracted from the DSC curves as follows. The temperature for the single strong signal, as well as for the signal at higher temperature if two strong peaks are observed, was taken as the mean value of the peak maximum temperature on heating and the peak onset on cooling curve. On the other hand, the temperature for the strong signal at a lower temperature was obtained from the maximum of the corresponding signal on the heating curve. In addition to the strong signals, a weak signal was noted at lower temperature in the DSC measurements of AM50, AZ31 and AZ62a alloys. The evaluated temperatures in Tab. 3.2 are obtained using a higher weighting for the heating signals and are intended to indicate the best value of the corresponding phase transition temperatures. Both the measured temperatures and measured enthalpies in Tab. 3.2 are

considered to be consistent and reproducible; no significant dependence on the heating/cooling rates was observed.

More details of the DSC response to the varying Zn content in AZ61 and AZ62a alloys are given in Appendix C.

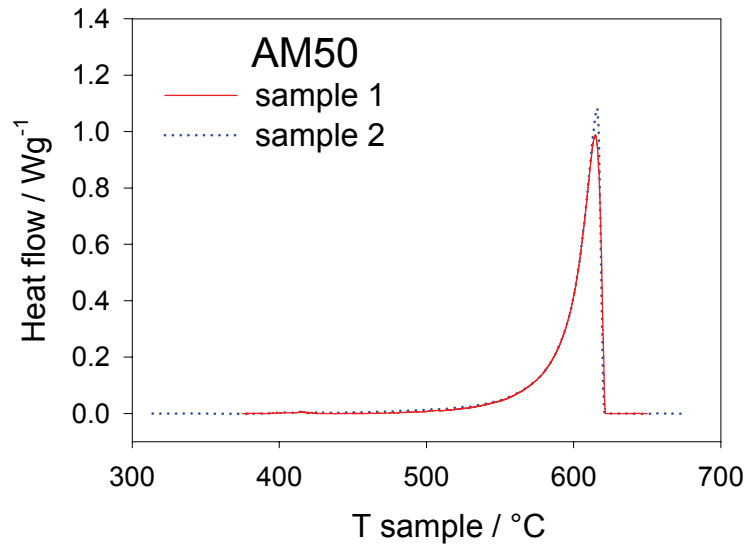


Figure 3.8a. DSC signals of two AM50 samples at a 5 K/min cooling rate demonstrate the perfect reproducibility of the present Ta-encapsulated DSC experiments.

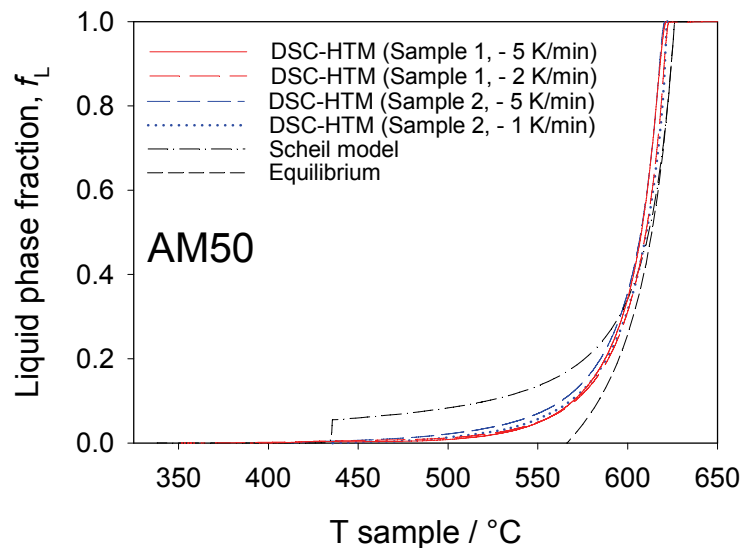


Figure 3.8b. DSC-HTM calculated solidification curves of the AM50 alloy. Scheil and equilibrium calculations are also shown.

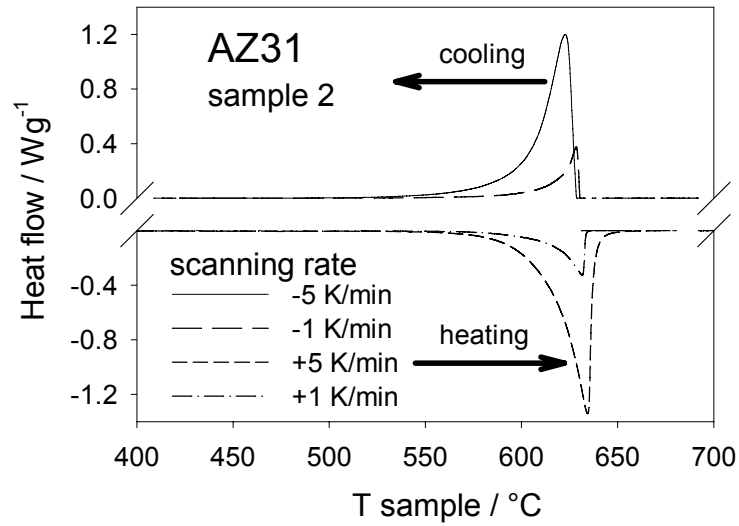


Figure 3.9a. DSC signals of one AZ31 sample during both 1 and 5 K/min heating/cooling cycles.

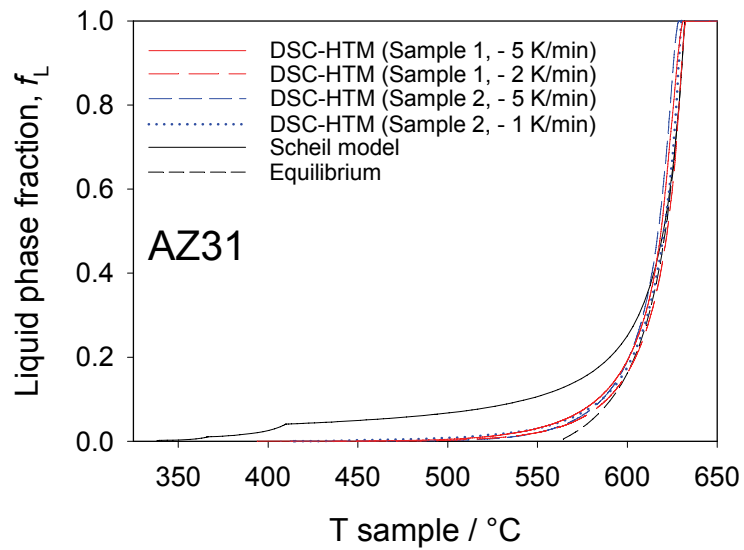


Figure 3.9b. DSC-HTM calculated solidification curves of the AZ31 alloy. Scheil and equilibrium calculations are also shown.

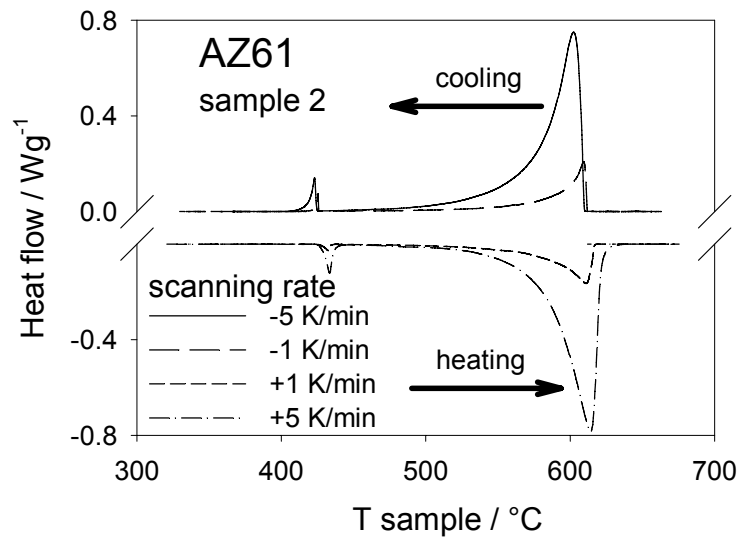


Figure 3.10a. DSC signals of one AZ61 sample during both 1 and 5 K/min heating/cooling cycles.

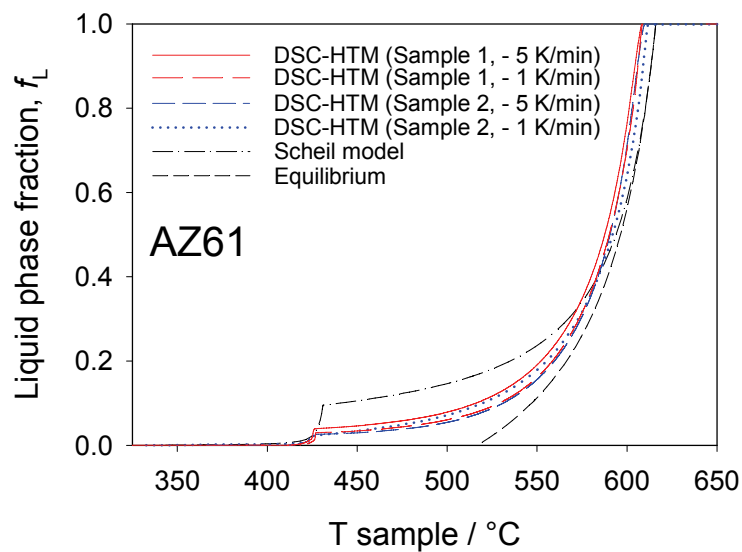


Figure 3.10b. DSC-HTM calculated solidification curves of the AZ61 alloy. Scheil and equilibrium calculations are also shown.

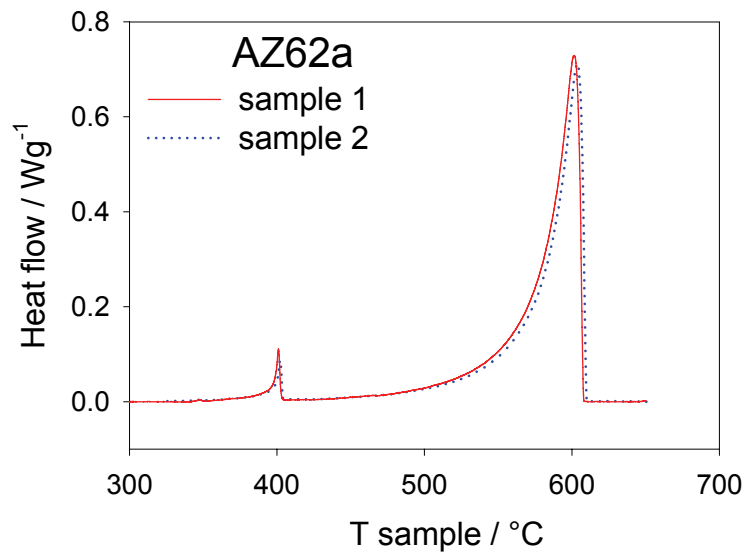


Figure 3.11a. DSC signals of two AZ62a samples at a 5 K/min cooling rate.

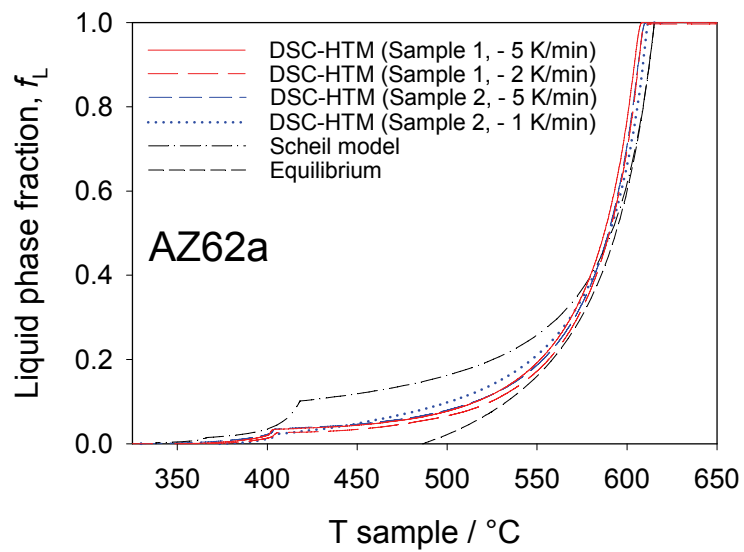


Figure 3.11b. DSC-HTM calculated solidification curves of the AZ62a alloy. Scheil and equilibrium calculations are also shown.



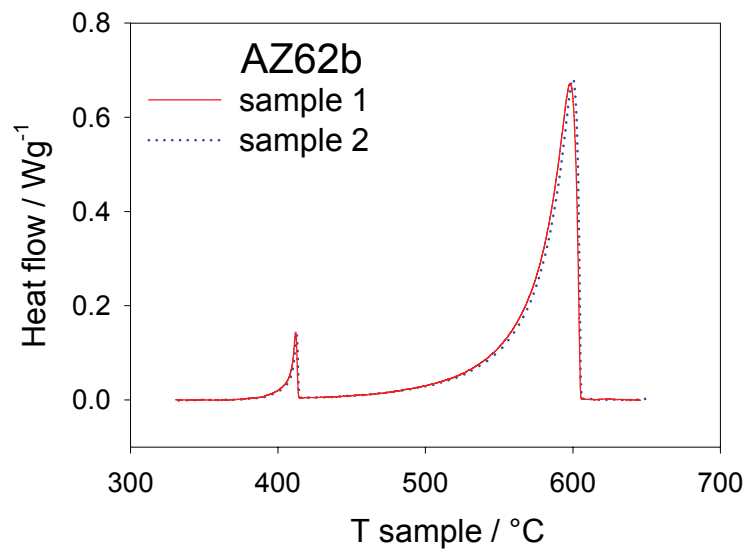


Figure 3.12a. DSC signals of two AZ62b samples at a 5 K/min cooling rate.

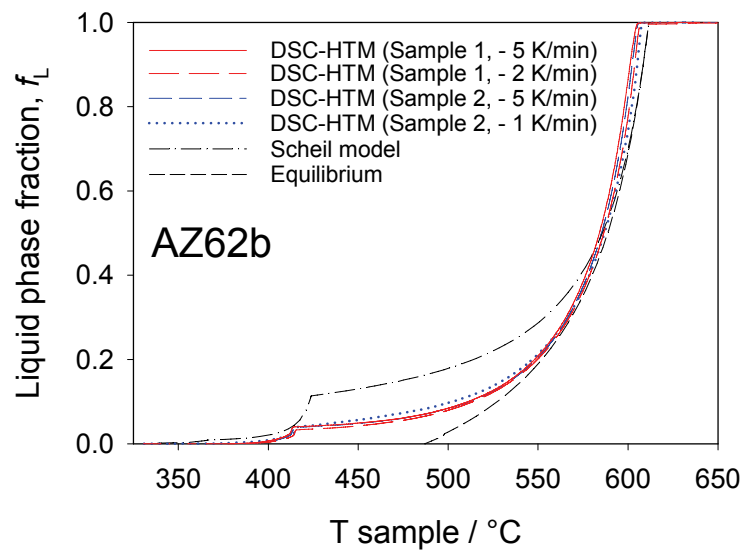


Figure 3.12b. DSC-HTM calculated solidification curves of the AZ62b alloy. Scheil and equilibrium calculations are also shown.

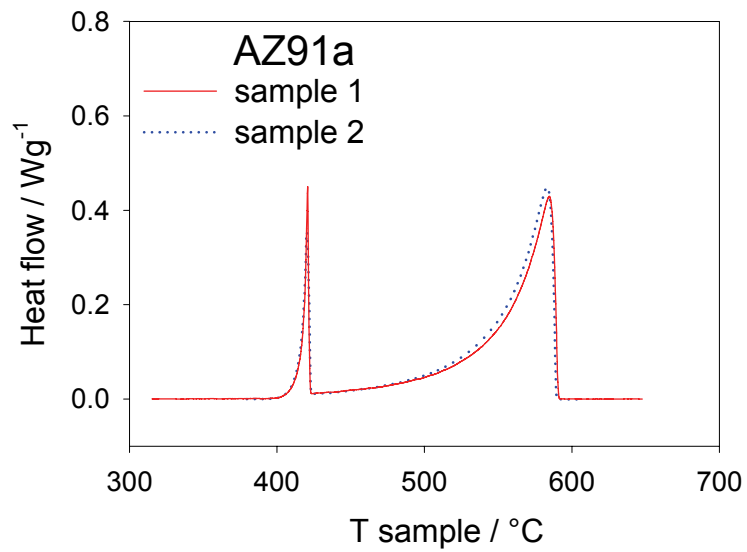


Figure 3.13a. DSC signals of two AZ91a samples at a 5 K/min cooling rate.

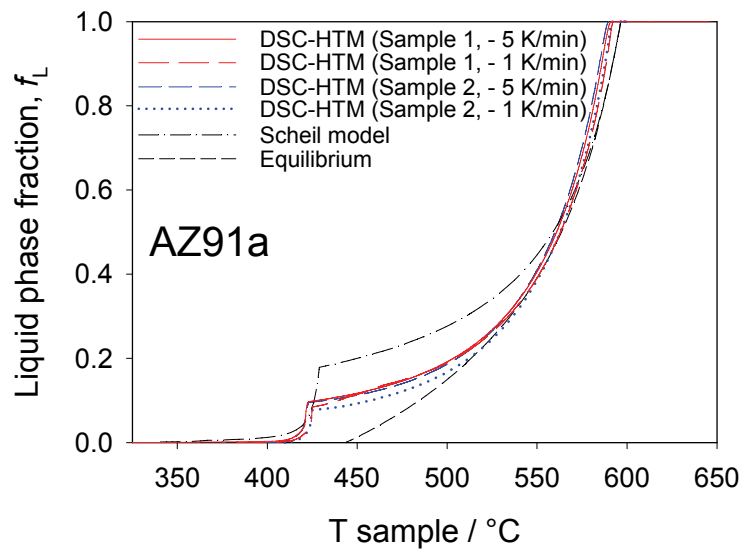


Figure 3.13b. DSC-HTM calculated solidification curves of the AZ91a alloy. Scheil and equilibrium calculations are also shown.

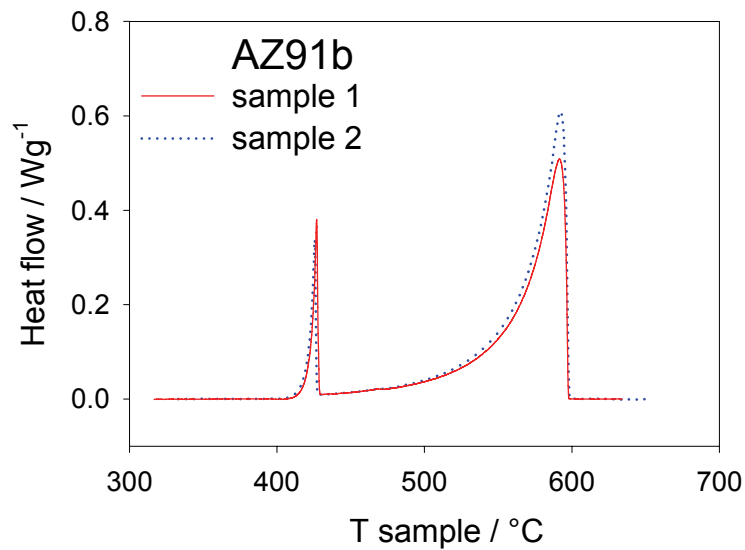


Figure 3.14a. DSC signals of two AZ91b samples at a 5 K/min cooling rate.

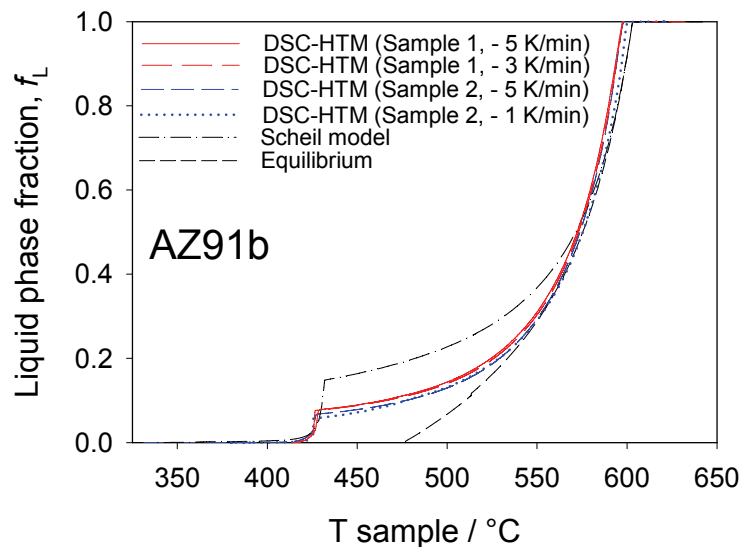


Figure 3.14b. DSC-HTM calculated solidification curves of the AZ91b alloy. Scheil and equilibrium calculations are also shown.

The compiled measured solidification enthalpies in Tab. 3.2 correspond to the quantity  $H$ , evaluated from the numerical procedure described above. In view of the invariance of the total latent enthalpy to the desmearing process, the same value is also obtained by a simple integration of  $\Phi_M(t)$ , thus providing an additional check on the correctness of the desmearing procedure. The maximum overall uncertainty of  $\pm 0.3$  kJ/mol is estimated for both the heating and cooling curves. The value in the column "equilibrium calculation" is obtained following

the approach for thermodynamic calculation of a latent enthalpy during equilibrium solidification given in [2004Gro]; the actual thermodynamic calculations were done with the PANDAT software package [2001Che] and are based on the Mg-Al-Zn-Mn subsystem dataset [2006Ohn1, 2006Ohn2, 2006Ohn3] of the larger thermodynamic database for magnesium alloys developed in our group [2001Sch].

### 3.3.2 Comparison with thermodynamic calculations of the solidification curves

Using the same thermodynamic dataset and software, solidification curves of the magnesium alloys were calculated applying two limiting solidification models (equilibrium and Scheil solidification). The compositions for the elements relevant for calculation, i.e., Al, Zn, Mn, and balance Mg, are indicated in Tab. 3.1 in bold letters. The resulting curves are presented in Figs. 3.8b-3.14b as dash-dotted lines (Scheil solidification) and short-dash lines (equilibrium solidification). It is noted that these two limiting models in fact essentially bracket the experimentally determined DSC-HTM solidification curves, as expected. A more detailed discussion follows later.

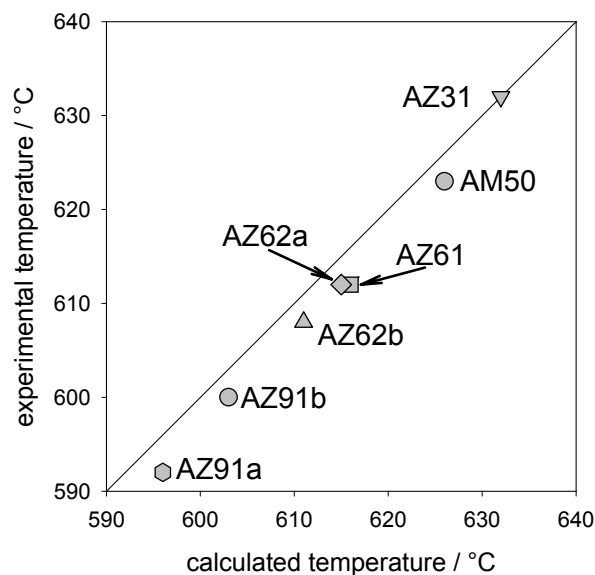


Figure 3.15. Comparison between the calculated and experimental "liquidus" temperatures for all studied alloys. The straight line is a visual aid corresponding to perfect agreement. The "liquidus" temperature corresponds de facto to the highest observable DSC signal and to the calculated start of massive crystallization of the (Mg) phase.

The comparison between calculated and experimental "liquidus" temperatures for the seven alloys is shown in **Fig. 3.15**. It was recently demonstrated [2006Ohn1] that the measured "liquidus" temperature for most of the AZ and AM Mg alloys generally does not represent the actual phase diagram value as the primary precipitate for these Mg-alloys (mainly  $\text{Al}_8\text{Mn}_5$ ) cannot be detected in the thermal analysis because of its small amount. The comparison in Fig. 3.15 is thus made based on the highest observable DSC signal, taken as the evaluated temperature in Tab. 3.2. From the thermodynamic calculation the exact temperature of the start of massive crystallization of the (Mg) phase was taken, even though a minute amount of  $\text{Al}_8\text{Mn}_5$  might have formed between this temperature and the (higher) true liquidus point. The calculated value thus reflects the  $\text{L}+(\text{Al}_8\text{Mn}_5) / \text{L}+(\text{Al}_8\text{Mn}_5)+(\text{Mg})$  phase boundary, if the alloy is located on the liquidus surface of this Al-Mn precipitate. There is no difference between equilibrium and Scheil calculation in this temperature range. A good agreement is obtained, considering the scale in Fig. 3.15. The mean deviation between experimental and calculated values is less than 3 K.

### 3.3.3 Reproducibility of DSC-HTM solidification curves

The evaluated DSC-HTM solidification curves in Figs. 3.8b-3.14b are based on the DSC measurements of two independent samples for each studied alloy and two different heating/cooling cycles for each sample. All DSC-HTM evaluated solidification curves, based on the two different DSC cooling runs of the same sample, are so close to each other that they could not be distinguished on the graph.

The excellent reproducibility of the DSC cooling curves between different samples is demonstrated for example in Fig. 3.8a for the alloy AM50 at -5 K/min. After HTM evaluation a similarly high reproducibility is obtained for the DSC-HTM solidification curves in Fig. 3.8b.

Further checks of the impact of experimental conditions on the reproducibility were performed by using an entirely different experimental setup. For two of our alloys, AZ91b and AZ62b, additional DSC measurements were performed by Prof. Ferro's group at the University of Genova and are evaluated for comparison. These DSC measurements were performed using a Setaram TG-DSC 111 calorimeter. The same scanning program was applied with a scanning rate of 3 K/min. Purified Ar flow at 2 l/min was used as protective measuring chamber gas. The DSC-HTM method presented above was applied to these experimental DSC curves. The resulting two solidification curves are shown in **Fig. 3.16** and compared with the corresponding curves from Figs. 12b and 14b, based on the measurements in our lab

---

in Clausthal. Comparing the curves for a given alloy, quite similar data are obtained, showing no drastic influence of the experimental conditions. It is noted that these conditions for the DSC measurements were completely different, concerning the design of the Ta capsule, thermally decoupled sample containers, argon instead of helium and so on in the other DSC apparatus.

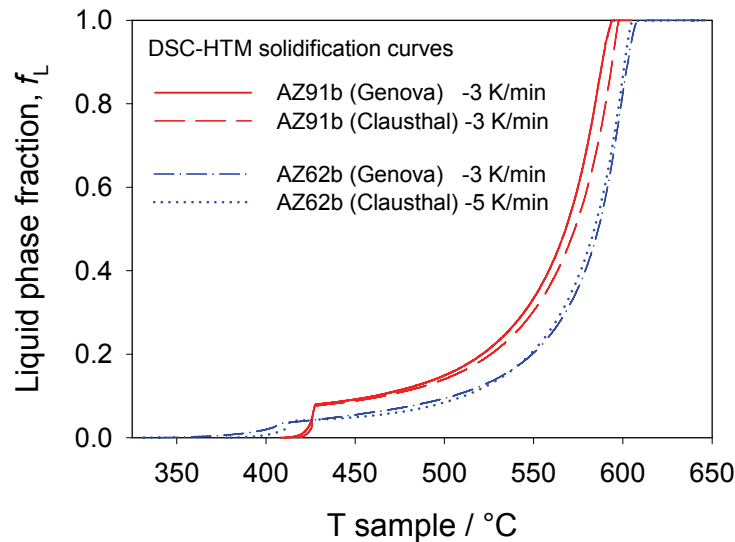


Figure 3.16. Comparison of solidification curves based on DSC cooling curves measured independently in different DSC equipment in Genova and Clausthal for the AZ91b and AZ62b alloys.

## 3.4 Discussion

### 3.4.1 Trends in the DSC-HTM solidification curves of Mg alloys and relation to thermodynamic calculations

It is interesting to note that the DSC-HTM solidification curves for a given alloy but at different cooling rates between 5 and 1 K/min in Figs. 3.8b-3.14b are very consistent with each other; the largest observed deviation is below 5 % of liquid fraction. One might have expected that under slower cooling the  $f_L$  curves would tend more towards the equilibrium limit; yet, that systematic trend cannot be clearly taken from Figs. 3.8b-3.14b, except maybe for the high-aluminum alloys AZ91a/b in Figs. 3.13b-3.14b. It is probable that this range of cooling rates is too narrow for a significant impact on the  $f_L$  curves of these Mg alloys. On the

other hand the range of 5 to 1 K/min is reasonable for intended caloric precision measurements in the present calorimeter setup. In the work of Larouche et al. [2003Lar] on the Al-4.5 wt.% Cu alloy, a clearer trend was observed at higher cooling rates (5, 10, and 60 K/min) also showing significant undercooling. Their DSC setup with open pans and 15 mg sample is not feasible for the more demanding Mg-alloys, requiring the present Ta-encapsulation.

In reviewing the  $f_L$  curves of the Mg alloys with a lower Al content (AM50 and AZ31) no low-temperature step is observed that relates to the sharp bends in the Scheil limit curves at 436°C or 410°C; these limiting calculations indicate a eutectic monovariant reaction, reflecting the start of additional  $\gamma$ -Mg<sub>17</sub>Al<sub>12</sub> phase precipitation. Weak signals are observed in the corresponding DSC curves at 435 and 368°C, though, as given in Tab. 3.2. This indicates that the qualitative trend for these alloys is closer to equilibrium (no eutectic at all), compared to the other five alloys with higher Al content. They all do show a clear eutectic bend in the DSC-HTM  $f_L$  curves in vicinity to the bend in the Scheil limit in Figs. 3.10b-3.14b. This trend is supported by a recent study on the non-equilibrium solidification and incipient melting temperatures of the alloys in the AM and AZ series [2006Ohn1]. Also, the fact that this eutectic bend is strongly curved (monovariant) rather than a sharp nonvariant step is reflected in both the DSC-HTM  $f_L$  curves and the Scheil limit calculations for all these alloys. Therefore, these alloys with higher Al content may be rated as closer to the Scheil than to the equilibrium limit, compounding the notion of extremely strong microsegregation of the Al component in these Mg alloys, especially for AZ91.

The measured latent solidification enthalpies,  $H$ , in Tab. 3.2 are consistently the same for heating or cooling runs and scanning rates from 5 to 1 K/min. For example, looking at the four rather different DSC signal curves of alloy AZ61 in Fig. 3.10a, it is astounding that they all convert to the same value of  $H = 7.3 \pm 0.3$  kJ/mol. The obvious significant undercooling of the second thermal signal does not affect the total enthalpy. These experimental values tend to be a little lower than the calculated equilibrium values in Tab. 3.2, but agree essentially within the overall uncertainty. For comparison, the latent enthalpies have also been calculated assuming Scheil solidification, using the same method as given in [2004Gro]. The resulting values of  $H$  are slightly above the equilibrium calculation, for example 8.05, 7.63 and 7.29 kJ/mol for AZ31, AZ61 and AZ91a, respectively, with a larger uncertainty of about  $\pm 0.3$  kJ/mol. They follow the same trend of decreasing values as in the equilibrium calculation or in the experiment. This indicates that the total value of  $H$  is a quite distinctive parameter for these alloys, not strongly dependent on the cooling rate and irrespective of an assumption made on the linearity of  $H(f_L)$ .

---

The experimental DSC-HTM  $f_L$  curves of all seven alloys fall, within the experimental uncertainty, inside the limits given by the Scheil and equilibrium curves. This supports the qualitative usefulness of these limiting solidification models. So-called micro-models [1998Kur] should be applied for a quantitative description as detailed by Boettinger and Kattner [2002Boe] or by Xie et al. [2003Xie]. However, in addition to the complete thermodynamic description of the alloy system these micro-models require detailed kinetic and thermophysical parameters. It is then possible to calculate also the enthalpy-temperature relation with higher accuracy using solute-diffusion. Dong et al. [2003Don1] also noted the necessity of using microsegregation models to obtain solidification curves on the basis of heat evolution measurements. Based on the present results we entirely agree with this suggestion to use micromodels for a detailed description, if all the thermodynamic and kinetic data are available. A key point of the present work is to demonstrate that even without knowing any of these data it is possible to determine the solidification curve of a given Mg-alloy using the DSC-HTM method with high reproducibility. This is also important in order to provide independent experimental information in order to check more sophisticated microsegregation solidification models of such alloys.

### 3.4.2 Intricacy of the "liquidus" temperature and Mn content

The impact of alloy composition on the "liquidus" temperature is shown in Fig. 3.15, and the intricacy of formation of  $Al_8Mn_5$  was outlined in section 3.3.2. The AZ62a and AZ91a alloys, having a very reduced Mn content, display the true liquidus temperatures (calculated) of 615 and 596°C, respectively, with (Mg) being the primary forming phase. The corresponding alloys AZ62b and AZ91b with a commercially typical Mn content of around 0.2 wt.% Mn fall in the same range with 611 and 603°C for the start of the bulk (Mg) solidification; the variation in Al and Zn content is mainly responsible for the variation in these temperatures.

The important point is that both AZ62b and AZ91b exhibit true liquidus temperatures (calculated) of 642°C, outside the frame of Fig. 3.15. This is where the calculation shows the start of primary crystallization of  $Al_8Mn_5$ . That phase is in fact observed in tiny amounts in the microstructure, shown in Fig. 2.7 in Chapter 2 and magnified in **Fig. 3.17** as bright needle-like  $Al_8Mn_5$  precipitates.

---



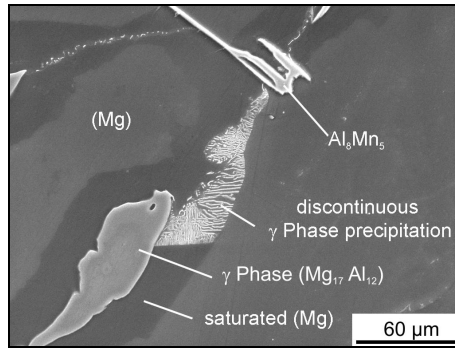


Figure 3.17. Electron micrograph (BSE) of the AZ91b sample. Even under the slow cooling rate of 1 K/min the non-equilibrium  $\gamma$  phase particles are precipitated, resembling a Scheil solidification model with substantial Al-segregation.

Even utmost scrutiny and numerical evaluation of the digital DSC signals does not reveal a peak in this higher temperature range. This is well explained by the minute amount of  $\text{Al}_8\text{Mn}_5$  phase fraction, being less than 0.001 as predicted by the thermodynamic calculation, which also shows the negligible heat effect during solidification of this primary precipitate. In summary, it is not possible to detect this true liquidus point using thermal analysis, not even with the present dedicated DSC setup for Mg alloys.

In addition to these tiny primary  $\text{Al}_8\text{Mn}_5$  crystals the microstructure in Fig. 3.17 also demonstrates the occurrence of coarse  $\gamma$ - $\text{Mg}_{17}\text{Al}_{12}$  crystals, grown during solidification in a eutectic, right next to some finer solid state precipitated  $\gamma$ - $\text{Mg}_{17}\text{Al}_{12}$ . This eutectic should not occur under equilibrium conditions, as seen in Fig. 3.14b. Even though this DSC sample had been cooled under only 1 K/min, a much slower cooling rate compared to real castings, this microstructure demonstrates that the solidification process of this alloy is close to the Scheil conditions, typically used for very rapid solidification. A very slow solid state diffusion in this alloy is responsible for this behavior [2006Ohn1]. This indicates that the measured fraction solid curves may also be useful for higher cooling rates, keeping in mind that additional undercooling effects are expected at much higher cooling rates.

### 3.4.3 Higher order time constants

The heat-transfer model applied in this work employs only the first time constant  $\tau_1$ . This means that a heat flow resistance between the temperature sensor (thermocouple) and the sample/reference material is neglected ( $R_2 = 0$ ). That implies the assumption of zero temperature difference between the sample/reference material and the corresponding thermocouple ( $T_S = T_{MS}$  and  $T_R = T_{MR}$ ). One should be aware of the limitations in desmearing ability of the proposed model caused by this simplifying assumption. Clearly, this assumption

is more adequate for the cases where the thermocouple is directly immersed in the sample. However, in this work the thermopile is mounted externally on the walls of the Ta-capsule. For three reasons it is supposed that this simplification ( $R_2 = 0$ ) does not crucially affect the desmearing quality of presented model: Firstly, good adhesion between sample and the inner side of the capsule bottom was always observed in this study. Secondly, tantalum is known to have a high thermal conductivity (57 W/mK) and the wall thickness of the capsule was chosen as thin as possible, 0.25 mm at the bottom and 0.4 mm at the wall. The third reason supporting this assumption is the installation of the thermocouples around the sample/reference cells. The cells are thermally coupled/connected by 2 thermopiles, both consisting of 20 pairs of thermocouples. The thermopiles are mounted laterally to the cells, so that only a thin-wall ceramic cylinder separates the thermocouple junctions and the Ta-capsule, which is tightly fitting in the ceramic cylinder. In summary, without using the second time constant,  $\tau_2$ , the current approach does not lose considerably in accuracy but remains suitably simple for application.

A possible improvement of the above presented heat flow model and the desmearing procedure could be achieved by application of the next higher second time constant ( $\tau_2$ ). In this way, a second order approximation is obtained, where the previously neglected heat flow resistance between the sample and its thermocouple ( $R_2$ ) is taken into consideration. This second heat flow resistance affects the difference between the real sample temperature and the temperature recorded on the measuring point, as depicted in Fig. 3.3. The impact of the sample substance in the crucible on ( $R_2$ ) has been discussed previously [1970Wie]. In analogy to Eq. (3.5b), the ( $R_2$ ) is related to ( $\tau_2$ ), which is the second time constant and is expressed as a product of  $R_2$  and  $C_S$  ( $\tau_2 = R_2 C_S$ ). This second time constant is typically much smaller than the first one ( $\tau_1$ ) and can be determined by application of a built-in calibration resistor to generate a heat pulse with known electrical current and pulse time. Even if this method of determination offers some advantages (easy measurements possible at any temperature), there are also some disadvantages that need to be mentioned here. The majority of heat flow DSC devices, especially disk-type systems, are not equipped with permanently installed calibration heaters. Even more important is that the heat pulse should be released within the actual sample in order to accurately determine the ( $\tau_2$ ) constant, which is usually very difficult to realize [1983Sch]. Different locations of the built-in heater and the sample, as well the heat flow through the wires introduce systematic uncertainties. These difficulties are substantially compounded for the customized DSC device of the present study. The fitting of a calibration resistor inside of the sealed Ta-capsule would be extremely difficult to realize, not to speak of

---

placing it inside an Mg alloy sample. If this is not done, the applicability of a ( $\tau_2$ ) value obtained in an empty Ta-capsule for the desmearing of DSC curve of particular sample material is questionable. For these reasons, the advanced desmearing procedure involving the second time constant ( $\tau_2$ ) is not applied in this work.

#### 3.4.4 Conventional thermal analysis compared to DSC

The limitation of the conventional thermal analysis regarding its application for determination of the solidification curves is discussed in the Chapter 2, section 2.6.1. In that section the comparison between the conventional thermal analysis and DTA has also been detailed. In Chapter 2, where a similar heat-flow model was applied to DTA measurements, the base line alteration was found to cause the highest deviation of obtained solidification curves (section 2.4.1). In this respect, the conventional TA is even more cumbersome, because the base line construction is even more uncertain compared to DTA (see section 2.6.1). The superiority of DSC equipment, even compared to DTA, regarding the reliability of the base line construction is highlighted in this work, even if a base line construction always remains arbitrary to some extent. The high base line stability, typical for the cylinder-type DSC device used in this work, significantly diminishes the impact of base line fitting.

### 3.5 Conclusions

Solidification curves of magnesium alloys are determined by processing DSC-measured signals with a heat-transfer model (HTM) based on the Tian equation. The following important improvements were included:

- (i) The temperature dependence of the time constant for the customized DSC setup is determined from independent measurements and not from DSC signals of the alloy samples;
- (ii) The measured DSC signals are processed in an impartial modus, without defining the termination of solidification artificially by the operator;
- (iii) The tantalum encapsulation of the Mg alloy sample was optimized and customized for the cylinder-type DSC device and proved indispensable for the generation of reproducible and reliable data.

Highly reproducible DSC-HTM solidification curves,  $f_L(T)$ , are determined for important Mg alloys of the AZ and AM series. They indicate that for cooling rates between 5 and 1 K/min, the  $f_L(T)$  curves show no significant variation with cooling rate; also, the alloys with higher Al content may be rated as closer to the Scheil than to the equilibrium limit as demonstrated by thermodynamic calculations.

---

The total value of latent solidification enthalpy  $H$  is revealed as a quite distinctive parameter for these alloys, not strongly dependent on the cooling rate, even between the Scheil and equilibrium limits, and irrespective of an assumption made on the linearity of  $H(f_L)$ .

The impact of manganese at commercially typical contents of about 0.2 wt.% Mn on the true "liquidus" temperature is detailed. Due to the intricacy of possible  $Al_8Mn_5$  formation in minute amounts before the bulk solidification of (Mg) starts, it is not feasible to detect this true liquidus point using thermal analysis, not even using the present dedicated DSC setup for Mg alloys. It could only be detected in thermodynamic calculations, supported by microstructural observations.

The DSC-HTM method is compared to alternative methods based on thermal analysis or differential thermal analysis. The superiority of DSC based method is mainly due to a much better heat flow stability requiring only a very small base line correction. This diminishes significantly the error introduced by ambiguous construction of a base line in DTA and especially TA.

The present work demonstrates that the DSC-HTM  $f_L(T)$  curves cannot be described quantitatively by the Scheil and equilibrium limits. Application of micro-models with a more detailed description of microsegregation, including back diffusion etc., is thus a necessity for a better theoretical modeling. Such micro-models require, in addition to the complete thermodynamic description, detailed knowledge of kinetic and thermophysical alloy parameters, which are generally not available for magnesium alloys. A key point of the present work is to demonstrate that even without knowing any of these data it is possible to determine the solidification curve of a given Mg-alloy using the DSC-HTM method with high reproducibility. This may also be important in order to provide independent experimental information in order to check more sophisticated microsegregation solidification models of such alloys. The results indicate the potential of this DSC-HTM method for simple, fast and reliable determination of solidification curves even for highly reactive alloys.

---

## **4 Comparison of DTA-HTM and DSC-HTM solidification curves**

### **4.1 Introduction**

In this chapter a comparison of improved in-situ DTA-HTM and DSC-HTM methods for determination of solidification curves is presented. The detailed overview of these methods regarding their advantages and limitations is given in Chapter 2 for DTA-HTM and Chapter 3 for DSC-HTM. .

A mathematical heat-transfer model (HTM) based on the Tian linear first-order differential equation is applied to the measured DTA and DSC curves of the following magnesium alloys: AZ31, AM50, AZ61, AZ62 and AZ91, thus providing their corresponding solidification curves.

Compared to earlier work, a better simulation of the measured DTA and DSC signals is attained through an independent measurement of the time constant as function of temperature for the applied equipment. A further improvement is achieved through a more impartial interpretation of the measured DTA/DSC curves, where the termination of solidification is not being artificially defined by operator. Both improvements enable a better desmearing of the DTA/DSC signal and reduce the error induced by the operator. The comparison of different applied measurement techniques (DTA and DSC) and their respective limitations to obtain solidification curves is in the focus of this presentation.

Reproducibility and reliability of obtained DSC-HTM solidification curves are also tested. For this reason independent samples of AZ62 and AZ91 alloys are measured by DSC at the group of Prof. Ferro at the University of Genova applying entirely different experimental set up. Both DSC experimental data recorded in Clausthal and Genova are processed by the improved heat-transfer model and resulting solidification curves are compared.

### **4.2 DTA and DSC Experiments and corresponding Heat-Transfer Model (DTA-HTM and DSC-HTM)**

#### **4.2.1 Experimental procedure**

The chemical composition of the studied alloys is given in Tab. 3.1, section 3.2.1. The samples denoted as AZ62 and AZ91 in present chapter are given as AZ62b and AZ91b, respectively, in the Tab. 3.1.

---

High oxygen affinity, vapor pressure of the measured Mg alloys, as well high reactivity of alloying element aluminum significantly complicate searching of the proper sample crucible for DTA/DSC measurements. The commercially available crucible solutions have been studied, but rejected owing to various limitations. Details on selection criteria why tantalum has been chosen as crucible (capsule) material are given in Chapter 2, section 2.3.1 The cross-sections of applied Ta-capsules are shown in **Fig. 4.1**. They differ for DTA and DSC. The capsules are sealed by electric arc welding under argon with 1.5 bar total pressure.

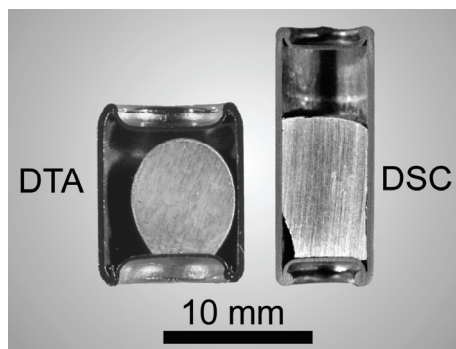


Figure 4.1. Cross-section of the used DTA and DSC Ta-capsules. The capsules are shown with Mg alloy sample after being measured by DTA and DSC, respectively

The developed Ta-capsule is particularly adapted to the methodic requirements of both applied methods of thermal analysis. The height-width ratio of the DTA capsule is adapted to the bottom mounted thermocouple and bottom was made from as thin as possible Ta sheet material. The design of DSC capsule suits very well applied cylinder-type DSC equipment. Aspects of reliability and handling are also considered during the development of the Ta-capsules.

DTA apparatus in Clausthal and DSC in Clausthal and Genova have been used to measure AZ62 and AZ91 alloys. Remaining alloys are measured only by DSC in Clausthal. For each alloy composition two independent samples were studied and two or three heating/cooling cycles were performed for each sample. For DTA overall uncertainty is estimated to be  $\pm 3$  K and for both DSC systems  $\pm 3$  K and  $\pm 0.3$  kJ/mol by temperature determination and caloric measurements, respectively.

DTA experiments in Clausthal are performed using a Netzsch DTA 404S (NETZSCH GmbH, Selb, Germany) apparatus. DSC experiments in Clausthal are performed by Setaram MHTC 96 heat-flow DSC equipment (SETARAM Instrumentation, Caluire, France). This is cylinder-type measuring system with thermally-coupled sample containers which were helium flushed during the measurement. DSC experiments in Genova are performed using a heat-flux

twin cylindrical Calvet-type calorimetric system Setaram TG-DSC 111. Also cylindrical Ta-capsules (not shown in Figure 1) with 6 mm inner diameter and 13 mm height were used.

#### 4.2.2 Heat-transfer model (HTM)

The modeling of the heat flow between DTA/DSC cells and the furnace applied in this work is based on the so-called Tian equation [1989Hem, 1996Hoe] for the heat flow  $\Phi_r$  [J/s] produced through reaction or transition inside the sample. The equations 1a and 1b are given for DTA and DSC, respectively:

$$\text{DTA:} \quad R_1 \Phi_r = \Delta T_M + R_1 (C_S + C_C) \frac{d(\Delta T_M)}{dt} \quad [\text{K}] \quad (4.1a)$$

$$\text{DSC:} \quad \Phi_r = \Phi_M + R_1 (C_S + C_C) \frac{d\Phi_M}{dt} \quad [\text{J}] \quad (4.1b)$$

where  $t$  is the time and for DSC  $\Phi_M = (\Phi_{FR} - \Phi_{FS})$  is the heat-flow difference between sample and reference which is directly measured during the DSC experiment. Analogically for DTA,  $\Delta T_M = (T_{MS} - T_{MR})$  stays for the directly measured temperature difference between sample and reference cells. It is worth noting that the both directly measured quantities  $\Phi_M$  and  $\Delta T_M$  are not directly equivalent to the actual heat flow (the rate of the reaction) in the sample due to the thermal lag (smearing) between event and corresponding thermocouple response [1985Loe]. The term  $R_1 (C_S + C_C)$  is commonly marked as  $\tau_1$  and named the first time constant. The  $\tau_1$  is defined by heat flow resistance between furnace and the sample thermocouple ( $R_1$ ) and the heat capacity of the sample cell (sample and crucible together). Related desmearing details for DTA and DSC have been discussed in sections 2.3.2.1 and 3.2.2.1, respectively. A schematic diagram of the both DTA and DSC methods and quantities relevant for the heat-transfer model are shown in **Fig. 4.2**.

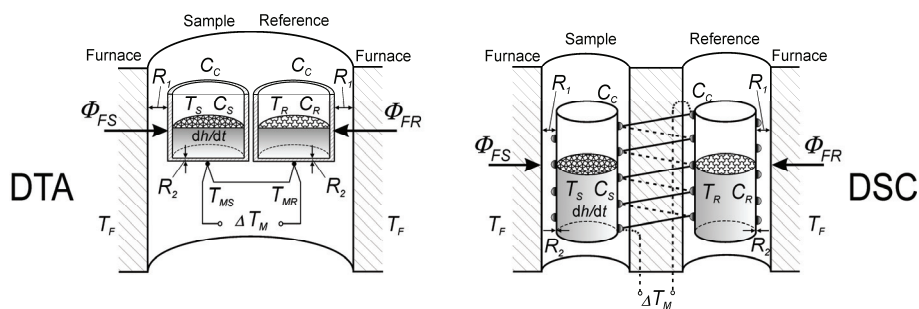


Figure 4.2. Schematic view of the DTA and DSC, with quantities relevant for the heat transfer model

It is not straightforward to establish an analytical correlation between released enthalpy of solidification and liquid (or solid) phase fraction using thermal analysis techniques. Among

other authors [1979Fre, 1986Bac], Chen et al. assumed a linear dependence of heat evolution during solidification on the liquid phase fraction  $f_L$ , in their application of the Tian equation to DSC experiment [1998Che] and with a similar heat-transfer model to DTA experiment [1996Che1, 1997Che] in order to determine solidification curves. Assuming this linearization, the heat flow generated by exothermic or endothermic reaction inside the sample,  $\Phi_r$  can be expressed by the heat evolution  $H d(1 - f_L)$  which occurs in the sample:

$$\Phi_r = \frac{H d(1 - f_L)}{dt} \quad (4.2)$$

where  $H$  is the total latent heat of solidification, assumed to be a constant for each alloy.

This linear dependence is often blamed to be a very rough simplifying approximation. Some authors [2003Don1, 2003Lar] even claimed that the accurate liquid fraction cannot be obtained directly using enthalpy measurements. However, if we calculate enthalpy as function of  $f_L$  for the studied alloys using our thermodynamic Mg-database [2001Sch] and Pandat program [2001Che] for Scheil solidification, **Fig. 4.3** is obtained. Calculated line for equilibrium case is not shown, it produces nearly a straight line. Even for the enthalpy release calculated after Scheil's condition, the assumption of linear heat release may be accepted as a first approximation. The specific heat contribution, included in Fig. 4.3, is also essentially linear and does not change this statement. The more detailed discussion about this very important subject relating enthalpy released during solidification and liquid phase fraction is given in sections 2.3.2.2 and 3.2.2.3.

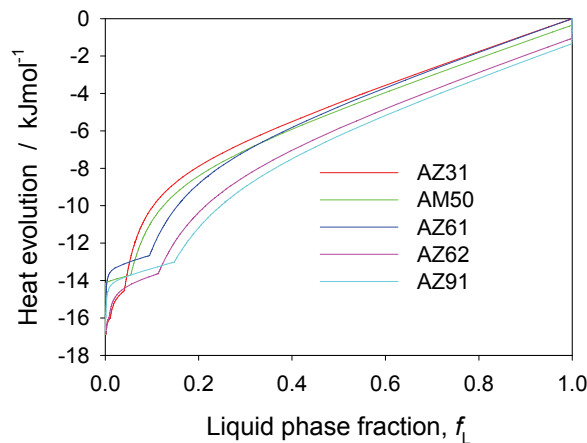


Figure 4.3. Dependence of heat evolution (total enthalpy of alloy relative to its value at liquidus temperature) on liquid phase fraction during the solidification; calculated according to Scheil conditions for the studied alloys



After combining Eqs.(4.1a/1b) and (4.2), the finite-difference form of final equation can be used for calculation of solidification curves. For this calculation, the knowledge of time constant  $\tau_l$ , as characteristic for the applied DTA/DSC equipment and experimental conditions, is necessary. In this study  $\tau_l$  has been determined independently using the cooling curves of pure metals measured at the same experimental conditions as the actual magnesium alloy samples (same Ta-capsule setup, scanning rates etc.). This in contrast to the previous work [1996Che1, 1997Che, 1998Che], where for the time constant determination the exponential tail of the last peak of the DTA/DSC curve was applied. This becomes questionable in the case when an unknown alloy sample with unknown solidification path or potential solid state reactions could corrupt the results. Detailed discussion why the peak decay of an alloy cannot be used for the determination of the time constants is given in chapter 3, section 3.2.2.2.

The next important point necessary to be discussed is the way how experimental DTA/DSC cooling curve are being processed to the solidification curve of investigated alloy. It is not necessary and even wrong to artificially proclaim one point on the curve, such as maximum of the last peak on the cooling curve, as the end of solidification, as it is being suggested by Chen et al. [1998Che]. The total heat released should be related to the entire area including the exponential tail [1968Gra]. More details on the novel evaluation method for treating the measured DTA/DSC signal are given in chapter 3, section 3.2.2.4.

### 4.3 Results and discussion

Exemplary, experimental cooling curves and solidification curves are shown only for AZ62 and AZ91 alloys. **Fig. 4.4a** shows the original experimental DTA and both DSC cooling curves and **Fig. 4.4b** the liquid phase fraction curves derived from them using the present DTA-HTM/DSC-HTM for alloy AZ62. It is obvious that  $f_L$  curves related to DSC curves show surprisingly good agreement. Even if the DSC curves are associated with two independent alloy samples and are recorded applying two completely different experimental set ups, the derived  $f_L$  curves virtually coincide in the graph. For comparison, the solidification curves calculated by limiting solidification models (equilibrium solidification and Scheil model) are also given.

**Figs. 4.5a and 4.5b** show the analogous data for the alloy AZ62. It is noticeable for both alloys that the solidification curves obtain by DTA-HTM exhibit higher amount of the  $\gamma$  phase, than those defined by DSC-HTM. This disagreement might be explained by the worse base line stability of DTA. DSC, which is superior compared to DTA with respect to

---

quantitative heat flow measurement and base line stability, is considered being capable to provide more reliable experimental basis data which are further processed to solidification curves. For both DTA and DSC,  $R_l$  decrease implies resolution improvement, but also proportional peak area decrease for DTA.

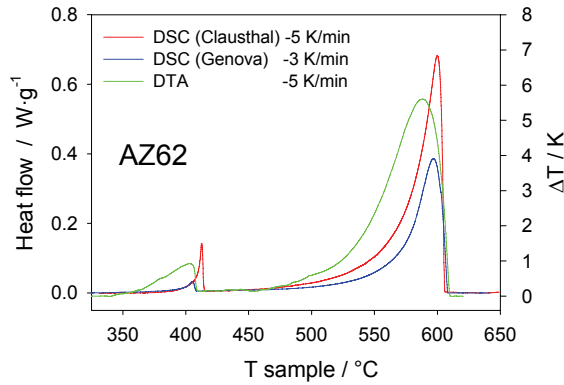


Figure 4.4a. The DTA/DSC signals of AZ62 alloy

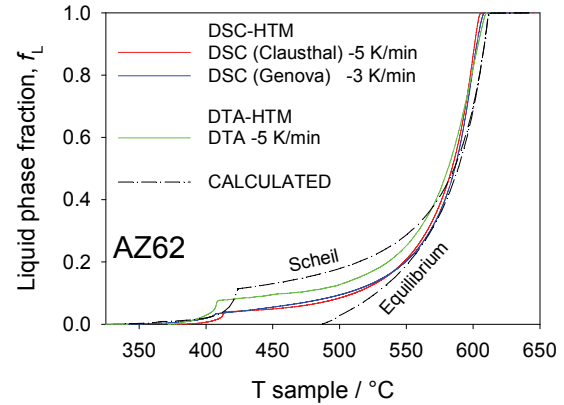


Figure 4.4b. DTA-HTM/DSC-HTM calculated solidification curves of AZ62 alloy. Scheil and equilibrium calculations are also shown.

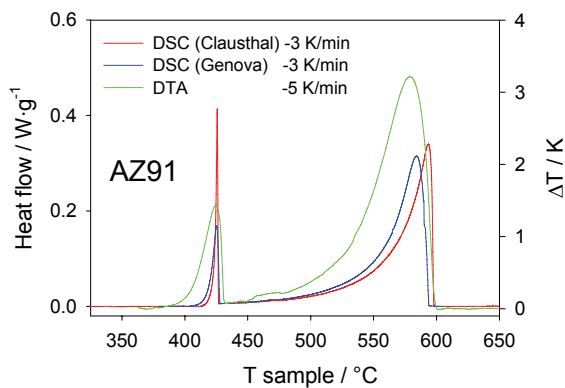


Figure 4.5a. The DTA/DSC signals of AZ91 alloy

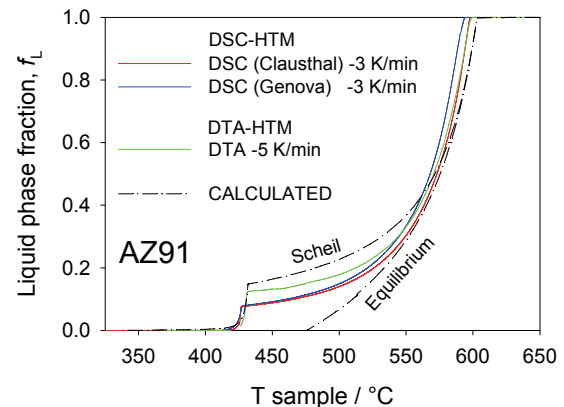


Figure 4.5b. DTA-HTM/DSC-HTM calculated solidification curves of AZ91 alloy. Scheil and equilibrium calculations are also shown.

The solidification curves calculated according to Scheil conditions show a qualitatively similar path compared to those given by DSC-HTM in Figs. 4.5b and 4.6b. This is in accordance with the metallographic analysis of DTA-cooled samples where even under the slow cooling rate of 1 K/min the non-equilibrium  $\gamma$  particles are precipitated, resembling a Scheil solidification mode, rather than equilibrium (Fig. 2.7, section 2.4.1).

---

The Scheil and equilibrium solidification models simulate two limiting cases of the solidification process. Even these two simple models require a complete thermodynamic description of the alloy system under consideration. Based on that information the enthalpy-temperature relation may be calculated and a higher accuracy is obtained using solute-diffusion micromodels additionally as shown by Boettinger and Kattner [2002Boe]. Dong et al. [2003Don1] also claim the necessity to use microsegregation models to obtain solidification curves on the basis of heat evolution measurements. We are in complete agreement with this approach to use micromodels for a detailed description *if* all the thermodynamic and kinetic data are available.

In this work a method of desmearing is introduced which involves independent determination of a time constant as function of temperature for the applied equipment. A further improvement is achieved through a more impartial interpretation of the measured DTA/DSC curves, where the termination of solidification is not being artificially defined by operator. The solidification curves obtained by DTA/HTM and DSC/HTM are compared where the base line construction is emphasized as one of the most important parameters influencing the reproducibility and reliability of solidification curves.

---

## **5 Directional solidification of Mg-Al alloys and microsegregation study of Mg alloys AZ31 and AM50, part I: Methodology**

### **5.1 Introduction**

The extent of microsegregation present in solidified alloys impacts the successful production and properties both of castings and of subsequently processed material. The workability and mechanical properties are particularly affected by the presence of microporosities and embrittling secondary phases. These detrimental aspects are typically intimately linked with interdendritic segregation which is defined as the compositional variability existing on the length scale of dendrite arms. Since most alloys solidify dendritically under commercially relevant conditions, the thorough understanding of solute partitioning and buildup of microsegregation is vital if these defects are to be controlled effectively. Also the heat treatment efficiency and final mechanical properties, such as yield strength or toughness, are strongly influenced by the extent of as-cast segregation [2007Gan].

Various micro-solidification models are available to elucidate the effects of microsegregation [1998Kur] and crystal growth morphology [2004Sek]. The models are ranging from simple Scheil model with most restrictive assumptions, up to the highly sophisticated approaches, such as promising phase-field method [2000Boe, 2004Sek]. The sophisticated models demand complete information about solid/liquid interface equilibria and various kinetic and thermophysical alloy parameters. Thus, their applicability is limited. This is particularly valid if Mg-alloys are treated, where the lack on necessary data is being quite slowly resolved. Only recently Böttger et al. [2006Boe] reported about controlling microstructure in Mg alloys by combination of thermodynamic, experimental and phase-field approach.

Whatever the model complexity may be, it is obvious that the reliability of any micro-solidification model needs to be validated against dedicated experimental measurements. Perhaps one of the most stringent tests for any microsegregation model is a comparison of the measured and model-predicted solute profile [2007Gan], even if some doubt has been raised in this regard [2003Lac]. The term "solute profile" is used for the solute concentration (content) *versus* solid phase fraction during solidification. It will be shown later in this work that, more specifically, the "solute" profile needs to be extended to comprise precipitates containing solute components. The X-ray mapping over a representative region of the sample,

---

usually performed by EPMA (Electron probe micro analysis), provides experimental data for solute profile determination which are typically superior to simple line scans. Sampling sites are commonly predefined by a grid. The solute profile for each element is then obtained by sorting the X-ray mapping data for the solute according to one of several sorting schemes. Here the sorting scheme denoted as WIRS (weighted interval ranking sort) and recently proposed by Ganesan et al. [2005Gan] is highlighted. It appears as significant novelty, overcoming substantial deficits observed in previous schemes, as discussed later. The WIRS approach is applied in the present work and it will be shown that it enables a quantitative treatment of primary non-matrix precipitates.

Numerous studies involving X-ray mapping of directionally solidified samples and data processing are found in the literature, mostly dealing with steel [1970Fle, 2003Lac], aluminum alloys [2003Xie, 2005Kur, 2007Gan] or superalloys [2005Gan, 2006Fen] but only few are found regarding magnesium alloys. Zhang et al. [2007Zha] recently combined directional solidification, electron probe micro analysis and Scheil solidification model to study morphology and microsegregation of a binary Mg-4 wt.% Al alloy. Pettersen et al. [1990Pet] studied dendrite crystallography of directionally solidified AZ91 Mg-alloy. Both studies have the application of Bridgman technique in common. In the present work the Bridgman-type directional solidification (DS) was also applied. The heat supply and extraction are adjusted in order to generate essentially constant temperature gradient ( $G$ ). Combination with a constant solidification rate ( $V$ ) provides well-defined and easy to control microstructure. Even if this is a well established technique [1998Kur], its application to Mg-alloys containing Al is challenging. This is relevant since most commercial Mg-alloys are alloyed with Al. The critical difficulties arise through Al-loss and melt pollution due to reaction between liquid alloy and sample container during directional solidification. This issue was ignored in the literature regarding directional solidification of the group of Mg-Al based alloys. This important aspect is discussed in detail in the following chapter.

The main purpose of this work was to develop a reliable method for directional solidification of Mg alloys containing Al, where the obtained microstructure can be used for an advanced analysis of microsegregation. The method was tested with two alloys, AZ31 and AM50, typically applied for rolling and die casting, respectively. The first novelty presented here is the application and optimization of a boron nitride (BN) coating to prevent detrimental reaction between solute Al and sample container, or tube. This coating is not considered as an isolated issue. It is the integrated understanding of the interaction between tube material, tube inside coating and applied Bridgman device parameters that enables controlling the reaction at the tube/sample interface. The preservation of the initial alloy composition during

---

solidification was a key criterion to judge the achieved result. The second methodic novelty is introduction of the correct implementation of the Scheil model for the solute profile calculation. Combination of the optimized DS method, sophisticated WIRS sorting scheme and real Scheil solute profile enables reliable microsegregation study of the Mg-alloys containing Al and appears to be reliable tool for determination of correct phase sequence during solidification. These methods are exemplified here essentially for the alloy AZ31; data for the alloy AM50 and a systematic comparison are in the focus of Chapter 6 of this thesis.

## 5.2 Reactions of Al-containing alloys with sample containers: a critical review

Preliminary experiments performed in this study emphasized the need to control the detrimental side reaction of liquid Mg-Al alloys with steel tubes during directional solidification (DS). Such problems, caused by the reaction of Al-containing melts with the container, are not unknown. Particularly the high pressure die casting (HPDC) industry dealing with Al-alloys and Mg-alloys containing Al is affected. Numerous literature reports related to this problem in HPDC practice are available [2002Sha, 2002Sha1, 2003Han, 2003Tan, 2005Che, 2007Nos]. A strong analogy between Bridgman-type directional solidification and die casting regarding this undesirable reaction can be extracted from a critical review of this literature, despite some differences with respect to thermal cycling and differing contact times. The conclusions of this review are presented below, starting with general criteria evaluating the feasibility of a tube material as container for DS.

### 5.2.1 Criteria for tube material selection

The three most important issues regarding selection of appropriate tube material are 1) reactivity, regarding Al loss and melt pollution caused by reaction at the tube-sample interface, 2) thermal conductivity, which affects temperature profile of Bridgman equipment, 3) linear thermal expansion, which might affect protection ability of applied coating. All of them are to be considered in order to prevent, or at least substantially reduce, reaction between alloying element Al and sample tube. Two most effective solutions to achieve this are: 1) tube material which is inert to the sample, and 2) effective surface coating.

It is quite difficult to find appropriate inert material. This is primarily due to the high reactivity of aluminum, which reacts with most metallic materials. Alumina is a good sample holder for liquid aluminum, but unacceptable for Mg-alloys due to the reaction of  $\text{Al}_2\text{O}_3$  with Mg. Iron is a good sample holder for liquid magnesium, but problems due to the reaction with

---

solute Al will be detailed below. Even though, for economical and practical reasons, it is worth while to investigate which one of the numberless steel sorts would perform best.

Steel application in contact with Al has already received a great deal of attention by Al-HPDC community [2002Sha, 2002Sha1, 2003Han, 2005Che]. One of the most pronounced negative phenomenon regarding steel application in Al-HPDC is die soldering, which is sticking of molten aluminum to the surface of the die material and remaining there after the ejection of the part. The die sticking due to chemical/metallurgical reactions between the molten alloy and the die at high temperatures is of special interest for this study. Not as severe, but principally similar effects are observed by the Mg-HPDC community [2003Tan, 2007Nos]. This effect is highly detrimental for both, Al and Mg, HPDC processes as it considerably decreases tool life and surface quality of the castings. Typical for die soldering is formation of intermetallic Al-Fe-rich phases on the die-melt contact surface; in the case of Mg-alloys the aluminum is introduced as major alloying element in the most important alloy groups AZ and AM.

Iron pickup of magnesium melts in steel crucibles is an additional detrimental effect caused by the contact between steel and Mg melts, particularly if the contact is held for longer time. Scharf and Ditze [2007Sch] reported recently that sludge and dross formation, as well increased iron melt content and inclusions of intermetallic particles are consequences of this effect.

### 5.2.2 Alternative non-ferrous tube materials

As the soldering is mainly due to high affinity between iron and aluminum, a plausible possibility to overcome that problem would be to replace steel by a non-ferrous material. Shanlar and Apelian [2002Sha1] tested four candidates, one tungsten-based, two titanium-based and one molybdenum-based material, against molten aluminum attack. They found that the tungsten-based alloy ANVILOY 1150 considerably postpones the start of intermetallic layer growth, compared to H13 steels die materials (composition given below).

Pure tantalum is already successfully applied for encapsulation of various Mg alloy samples in our laboratory [2005Mir, 2006Mir]. Non-ferrous tube materials were also regarded for application in this study, but rejected for the reasons given in chapter 7.1.1.

### 5.2.3 Uncoated steel application

Tool steels are commonly used in both aluminum and magnesium die casting industry. The H13 steel is often applied (Fe - 5Cr - 1Si - 1.5Mo - 0.4C - 0.4Mn - 0.9V, wt.%). Similar steels are well studied [2002Sha, 2002Sha1, 2005Che] regarding die soldering during Al casting.

---

Shanlar and Apelian [2002Sha] have studied mechanisms of the reaction between molten Al-Si alloy and H13 tool steel by performing a set of diffusion couple experiments. They found that in this case soldering is diffusion controlled process, where iron and aluminum atoms diffuse into each other resulting in the parabolic growth of a series of intermetallic compounds on the steel substrate.

Tang et al. [2003Tan] performed similar experiments immersing the H13 samples for 5-180 minutes into molten Mg-alloys at 680°C with various aluminum (3-12 wt.%) and manganese (0.18-0.52 wt.%) content. The role of manganese appears quite interesting: the Mn-free alloys with 3 and 6 wt.% Al showed only few dispersed intermetallic particles. A continuous intermetallic layer was formed only when the Al content of the melt reached 12 wt.%, even after only short dipping time, for Mn-free alloys. In this case only the Mn-free FeAl phase was found in the layer. On the contrary, all Mg-Al alloys containing Mn produced continuous Al-Fe-Mn intermetallic layer. The Mn accumulates in the layer, up to 48 at.% Mn. The same authors investigated AZ91 Mg-alloy (Mg - 9 Al - 1 Zn - 0.5 Mn, wt.%) at conditions described above and found linear growth rate of intermetallic compound thickness; this suggests surface reaction control and differs from the parabolic relationship found for Al-Si alloy [2002Sha], discussed above.

The only tube material reported so far for directional solidification of Mg alloys was the corrosion resistant austenitic Cr-Ni alloyed stainless steel [1990Pet, 2007Zha], similar to the austenitic stainless steel denoted as V4A and investigated also in the present work.

#### 5.2.4 Protective measures

Protective measures applicable for ferrous material in contact with Al-containing melts could be divided into recommendations regarding process parameters and those concerning engineering of the contact surface.

The most effective process parameters are interface temperature but also the melt composition. [2002Sha1] reported about critical temperature of 671°C for combination of H13 steel and common Al-alloy with 10 wt.% Si, (ASTM 680). Importance of the melt temperature reduction is also identified in this study and will be discussed later.

Engineering of the inside tube wall surface characteristics by coating, heat treatment and surface reactions could be the most effective means of retarding Al-Fe reaction. Shankar and Apelian [2002Sha1] reported about steel nitriding and aluminizing and also boron nitride coating by plasma vapor deposition (PVD) as reasonable protective measures. PVD is also employed by [2007Nos] for coating H13 steel dies by TiAlN/a-C mixture, where a-C is

---



amorphous diamond-like carbon. It is difficult, though, to achieve a homogeneous protective layer *inside* a tube, especially for the small inner tube diameter applied in this work.

## 5.3 Experimental procedure

### 5.3.1 Starting magnesium alloy material

The AZ31 and AM50 alloys studied in this work were delivered as ingot specified as AZ31 by Dead Sea Magnesium Ltd., Israel and AM50 by Norsk Hydro Magnesiumgesellschaft mbH, Bottrop, Germany. The ingot chemical composition for AZ31 alloy is shown in **Tab. 5.1**, where the Fe, Cu and Ni contents are not shown, being less than 50  $\mu\text{g/g}$ . The ingot chemical compositions, as well as compositions related to subsequent sample preparation stages listed in Tab. 5.1, are provided by in-house chemical laboratory using ICP-AES (Inductively Coupled Plasma Atomic Emission Spectroscopy).

**Table 5.1.** Chemical composition [wt.%] of investigated AZ31 samples as ingot, before and after directional solidification (DS), balance Mg. EPMA is related to the mean value of all 441 points measured on the  $1 \times 1 \text{ mm}^2$  area.

Sample AZ31	Furnace temperature, $^{\circ}\text{C}$	$V$ , $\mu\text{m/sec}$	Analysis method	Al	Zn	Mn
Ingot	-	-	ICP-AES	2.85	1.05	0.23
Before DS	-	-	<b>ICP-AES</b>	<b>2.63</b>	<b>0.97</b>	<b>0.20</b>
After DS	720	82.8 <sup>c)</sup>	<b>ICP-AES</b>	<b>2.60</b>	<b>0.96</b>	<b>0.17</b>
			EPMA	1.72	1.22	0.05
		38.9 <sup>a)</sup>	<b>ICP-AES</b>	<b>2.61</b>	<b>1.05</b>	<b>0.12</b>
			EPMA	1.83	1.18	0.17
	800	82.8 <sup>d)</sup>	<b>ICP-AES</b>	<b>2.36</b>	<b>0.99</b>	<b>0.18</b>
			EPMA	1.60	1.17	0.03
		38.9 <sup>b)</sup>	<b>ICP-AES</b>	<b>2.51</b>	<b>1.09</b>	<b>0.13</b>
			EPMA	1.49	1.16	0.009

Conversion to cooling rates,  $GV$ : <sup>a)</sup> 0.381, <sup>b)</sup> 0.614, <sup>c)</sup> 0.811, <sup>d)</sup> 1.31 K/sec

### 5.3.2 Sample tube material and inside protective coating

The following two steel-types were tested as tube material:

- 1) Mild steel denoted as St35, material number 1.0308 (DIN 2391), which is a low-alloyed ferritic carbon steel containing Fe - 0.13 C - 0.23 Si - 0.45 Mn, wt.%;
- 2) High-alloyed austenitic stainless steel denoted as V4A, material number 1.4571 (DIN 2462), which was chosen to reproduce results published by literature. The steel composition was Fe - 17 Cr - 12 Ni - 2.1 Mo - 0.3 Ti - 0.50 Si - 1.3 Mn, wt.%.

The St35 steel was accepted as final solution. The seamless high-precision tubes with 5 mm inner and 6 mm outer diameter are cut into 600 mm long pieces. For all the experimental DS results presented in this report a highly efficient protective coating procedure was developed and applied as detailed below.

Boron nitride (BN) suspensions are accepted as necessary diffusion barrier between melt and tube. Such suspensions are commonly used for coating of casting tools in industrial practice. Three commercially available suspensions with different liquid phases (two ethanol-based and one water-based) and bonding agents (aluminum phosphate hydroxide, SiO<sub>2</sub> and magnesium aluminosilicate ) are tested. Brand names and providers are EKamold<sup>®</sup> EP by ESK Ceramics GmbH & Co. KG, Kempten, Germany; Hebocoat 400 E by Henze BNP GmbH, Kempten, Germany; Type-V by Saint-Gobain Advanced Ceramics, Lauf, Germany, respectively. Their efficiency was tested with both mild (St35) and stainless steel (V4A). Extensive tests showed that St35 steel coated by BN suspension denoted as “Type-V”, the water-based with magnesium aluminosilicate as bonding agent, performed best as protection. According to manufacturer specifications, the dried coating consists of 94 wt.% BN and 6 wt.% binder.

The coating was applied in the following manner: the inner tube surface was manually roughened by a bolt covered with sand paper and degreased by acetone. The BN suspension was applied by suction, left in vertical position to drain, dried for 10 minutes at 100°C and baked for 45 minutes at 350°C, as recommended by vendor. The BN coating appeared dull, slippery, white and quite hard, but varied in layer thickness. A shiny surface and uniform layer thickness of about 100 μm are finally obtained by careful polishing with cotton batting. Both alternative ethanol-based BN suspensions provided a smooth, equally thick coating after similar processing, but appeared much softer. These alternative coatings also went through the complete testing cycles with liquid metal, detailed below, before rating them as less efficient.

---

### 5.3.3 Sample tube filling procedure

Filling of the tube with sample material was performed in the following manner. The alloy ingots were cut, degreased, melted and held for 10 minutes at 750°C in a stainless steel crucible. The typical insert mass was 2 kg. The melting crucible was designed as deep (500 mm) and narrow (100 mm) vessel, exposing a relatively small melt surface to air. This surface was covered with a mixture of 0.4 vol.% SF<sub>6</sub> in Ar, at a flow rate of 250 ml/min. No burning or extensive Mg oxidation on the melt surface was observed. The steel crucible was heated in a vertical resistance furnace (height 500 mm), also used for preheating of the sample tubes to 700°C. The necessary preheating time to reach the target temperature of 700°C was initially determined by a thermocouple inserted in a sample tube. The preheated tubes were flushed by sucking protective gas available closely above the melt surface, then immersed into the melt and slowly (carefully) filled by suction. The melt flow stopped in the upper non-preheated tube section. After filling, the tube was taken out and cooled at ambient temperature. The preheating temperature and melt suction rate were subject to optimization in order to achieve the desired tube length filled by sample of 450 mm, exhibiting no bubbles, cavities or porosities in the sample. After filling, some samples were taken out of the tubes and analyzed by ICP-AES. The results are denoted as “Before DS” (directional solidification) in Tab. 5.1. Only slight Al-loss compared to ingot composition is observed.

The tube was shorted to 400 mm, removing the empty tube section. Mg-alloy residues sticking on the tube outer surface were also removed. A gas-tight sealing of the sample in the tube was obtained in the following manner: at the bottom and top end of the tube the alloy content was removed by drilling at 10 and 20 mm length, respectively. Solid steel cylinder inlays were tightly inserted into these holes and sealed by welding at both ends of the tube. The top side inlay was later used also for tube mounting in the Bridgman equipment for the DS experiment.

### 5.3.4 Bridgman equipment and DS procedure

The customized Bridgman furnace is schematically presented in **Fig. 5.1a**. The essentially constant temperature gradient zone was generated by heat supply designed as single-zone vertical resistance furnace and cooling trap with direct water sprinkling serving as heat extractor and promoter of unidirectional solidification of the melt. The temperature gradient  $G$  was varied by adjusting two different furnace target temperatures, 720 and 800°C. The corresponding "sample" temperature profiles were measured by 1 mm K-type thermocouple

---

inserted into an empty tube and are shown in **Fig. 5.1b**. The arrows at 228 mm indicate the water surface of the cooling trap. The distance on the x-axis relates to the upper steel block surface. This steel block is mounted fixed inside the furnace, improving its vertical temperature homogeneity. The spatial uncertainty in Fig. 5.1b is about  $\pm 1.5$  mm. Two horizontal lines indicate temperatures of 600 and 400°C, both marking the approximate freezing range of studied alloys (Tab. 3.2, section 3.3.1). The temperature gradient for each furnace temperature is calculated as slope of the secant line through two points, defined by intersection of temperature profile curve and 600/400°C lines.

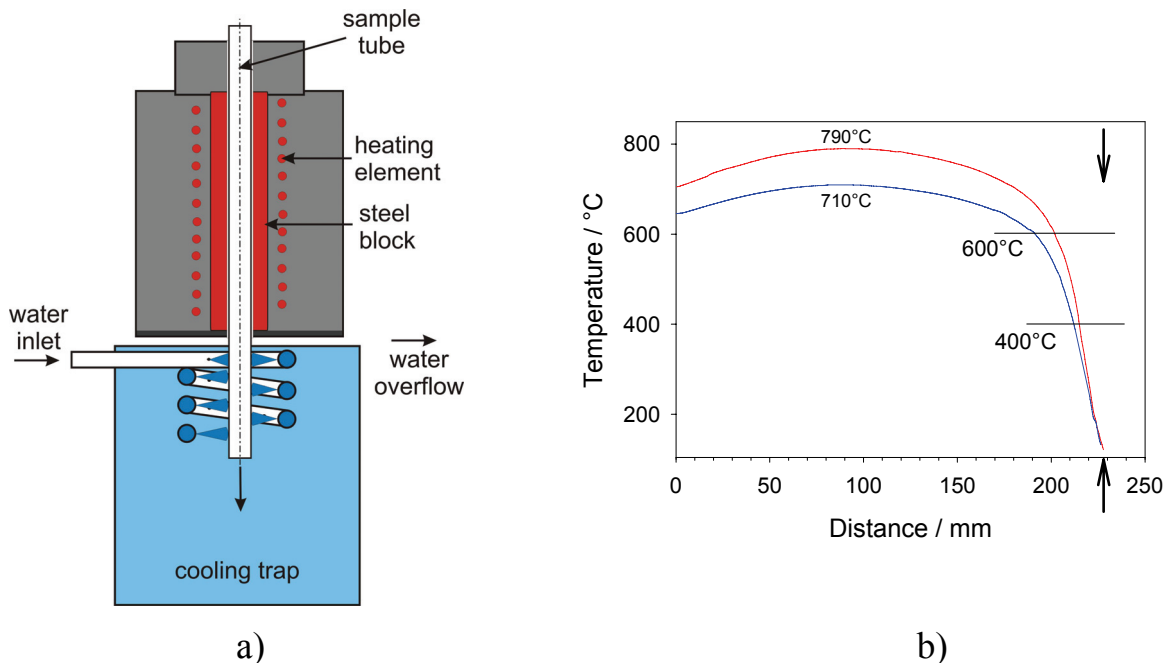


Figure 5.1. Bridgman equipment;

a) schematic presentation

b) temperature profiles. The arrows at 228 mm indicate the water surface of the cooling trap. The distance on the x-axis refers to the upper steel block surface.

A high precision sample positioning facility was used to enable accurate and smoothly controlled movement of the sample within the stationary furnace. The sample tube was hanged and linked by stainless steel wire to the positioning facility. Two sample speeds i.e. solidification rates were applied in this work, 38.9 and 82.8  $\mu\text{m}/\text{sec}$ . The combination of two temperature gradients and two solidification rates resulted in four cooling rates, given as  $G \cdot V$  values. The parameters relevant for directional solidification in this work are compiled in **Tab. 5.2** sorted according to increasing  $G \cdot V$  value. The table also includes the local solidification times for both alloys and four  $G \cdot V$  values. It is calculated by dividing each alloy

temperature freezing range by the corresponding  $GV$  value. The freezing range is defined here by a Scheil calculation where the first and the last 0.05% of the solid phase are excluded. More details on this calculation are given at the end of section 5.5.

Table 5.2. Relevant parameters for directional solidification.

Furnace temperature / °C		720	800	720	800
Temperature gradient $G$ 600→400°C / K·mm <sup>-1</sup>		9.8	15.8	9.8	15.8
Solidification rate, $V$ / μm·sec <sup>-1</sup>		38.9	38.9	82.8	82.8
Cooling rate, $GV$ / K·sec <sup>-1</sup>		0.381	0.614	0.811	1.31
Local solidification time <sup>a)</sup> / sec	AZ31	774	480	364	225
	AM50	509	316	239	148

a) freezing range see text.

The BN-protected steel tube containing the alloy was inserted through the cold furnace and immersed 20 mm into the water. The furnace target temperature (720 or 800°C) was attained within 2 hours. Afterwards, the sample tube was held at that temperature for 30 minutes before the directional solidification process was started by lowering the tube. The samples were solidified for a length of at least 100 mm with the preset moving speed. After the solidified alloy reached the desired length, the specimen was quenched into the lower part of the water cooling trap in Fig. 5.1a.

### 5.3.5 Microstructure and microsegregation characterization

For the subsequent cross-sectional microsegregation characterization the tube was crosscut at the position which was already slightly immersed at the time of quenching; that location was completely solidified before quenching. The samples were ground and polished down to 1 μm diamond under alcohol to avoid reaction with water. For EPMA measurement the sample was not etched.

For the light optical microscopic (LOM) analysis of the mushy zone in a longitudinal section, the sample was laterally grinded until approximately half of the cylindrical sample

was removed. The unfolded surface along the centerline was then polished as described above. The samples were etched in the solution of 1 HNO<sub>3</sub> + 19 H<sub>2</sub>O (by volume) for 15 seconds at room temperature.

**Quantitative segregation mapping:** The dendritic segregation characteristics of the constituent elements (Mg, Al, Mn and Zn) were analyzed by quantitative segregation mapping, using a Cameca SX-100 Electron Probe Microanalyzer (EPMA) (Cameca, Courbevoie, France) equipped with four wavelength dispersive spectrometers (WDS). The acceleration voltage, beam current and spot size for these analyses were 20 kV, 40 nA and 2 μm, respectively. These parameters are adapted to the quite sensitive Mg surface, preventing excessive damage by electron beam. The WDS system was equipped with diffraction crystals of TAP (used for Al and Mg), LIF (used for Zn) and LLIF (used for Mn). For all elements X-ray counts were measured for K<sub>α</sub> lines. These counts were converted to concentration values using standard correction procedures, calibrated from MgO for Mg, pure Zn for Zn, MnSiO<sub>3</sub> for Mn and potassium-feldspar for Al. A sample area of 1000 · 1000 μm<sup>2</sup> was scanned in spot mode with a grid spacing of 50 μm and a live sampling time of 30 seconds in each spot. The scanned area was located approximately in the center of the sample cross section. For each of the 21·21=441 grid points the linear peak background model was applied to the measured counts, including two offset measurements at each peak, each lasting for 15 sec.

**Compositional maps:** For qualitative solute compositional maps an area of 1000 x 768 μm<sup>2</sup> was scanned in spot mode with a grid spacing of 1 μm with the live sampling time of 20 msec. The same EPMA-WDS equipment and remaining acquisition parameters were applied. The scanned area is located approximately inside that of quantitative measurement.

## 5.4 Processing of the quantitative EPMA data

It is noted here that processed EPMA data have to conform to a random sampling approach proposed by Flemings et al. [1970Fle]. The current grid approach avoids subjective selection of scan points and appears reasonable. The solute profile for each element is then obtained by sorting the EPMA mapping data for the solute according to one of several sorting schemes. Current approaches for EPMA data processing are recently reviewed and thoroughly discussed by Ganesan et al. [2005Gan].

---

One widely employed technique implies sorting the data for each component *separately* into increasing or decreasing series, depending on their segregation behavior. Monotonous composition profiles for *each* element are thus obtained. The monotonous variation of the solid concentration with fraction solid is assumed and sub-solidus diffusion is ignored [2003Lac]. The method is recommended by Gungor [1989Gun] and applied to binary Al-Cu alloy. He also studied statistical significance and used the method to estimate eutectic volume fraction. However, some disadvantages are obvious. The individual sorting of each element does not correspond to a unique fraction solid of each measuring point. As a consequence, the sum of all elements at each assigned fraction solid may not be 100%. This approach is not considered further in this work.

Other approaches exist that partially overcome some of these problems, such as (1) sorting all the measurements based on composition of a single component, denoted as "leading-element sort", or (2) sorting based on the compositional difference between two solutes, the latter not being considered further in the present work. A characteristic weakness for both methods is the subjectivity with respect to the choice of the elements the sorting is being based on. Despite this weakness, the leading-element sort is tested in this work, since this sorting scheme is quite popular [2003Lac, 2003Xie] especially for a relatively small number of alloying elements. Basically, the concentration measurements of all solute elements are simultaneously ordered based on ascending or descending concentrations series of a particular solute element, the "leading-element". For example, assuming ascending aluminum concentrations with fraction solid, Al may be chosen as leading-element, thus defining the sorting of remaining solute elements. The assigned fraction solid is based on the ratio of monotonically ascending sampling site number to the total number of sampled points. This approach was used for comparison in this work.

However, the main disadvantage of these sorting methods is the entire loss of information regarding the length-scale. The obtained solute profiles compile the data as a progressive monotonous increase from low to high concentrations, at least for the leading element or its difference, regardless of the actual position in the specimen [2003Lac]. Thus the real phase sequence during solidification might be wrongly reflected in the solute profile. [2003Lac] recommended the study of the correlations between different solutes as the tool to sort the data for drawing solute profiles.

Along this line, Ganesan et al. [2005Gan] developed a sorting approach that is capable of separating the effects of data scatter from the underlying segregation trend. The approach is denoted "weighted interval rank sort" (WIRS) and comprises three steps: 1) Determination of

---

partitioning directions; 2) Ordering and ranking of EPMA data and 3) Assignment of fraction solid.

First step is determination of the segregation behavior of a particular solute. Among various methods to obtain this information [2005Gan], the elemental EPMA maps are used in this work to draw solute-solvent correlation relationships, such as shown below in section 5.6.4.2.

In the second step, the measured concentrations  $C_i^j$  of each component  $j$  at each measuring (grid) point  $i$  is first assigned a weighted value,  $\bar{C}_i^j$ , which is a difference according to

$$\bar{C}_i^j = \frac{C_i^j - C_{MIN}^j}{\sigma^j} \quad (5.1)$$

for a normally segregating element (partitioning coefficient less than unity) and by

$$\bar{C}_i^j = \frac{C_{MAX}^j - C_i^j}{\sigma^j} \quad (5.2)$$

for an inversely segregating element (partitioning coefficient larger than unity). Here  $C_{MIN}^j$  or  $C_{MAX}^j$  are the values of minimum or maximum concentration in the dataset for a given component  $j$  and  $\sigma^j$  is the experimental uncertainty associated with measurement of that component. In the present work the EPMA detection limit for each component was used as experimental uncertainty  $\sigma^j$ .

For each site on the grid, the  $\bar{C}_i^j$  values are then averaged over all components  $j$ , yielding

$$\bar{\bar{C}}_i = \frac{\sum_{j=1}^4 \bar{C}_i^j}{4} \quad (5.3)$$

where  $\bar{\bar{C}}_i$  is the mean value of  $\bar{C}_i^j$  for all four components Mg-Al-Zn-Mn in the alloy. A rank number  $R_i$  is assigned to each site according to increasing values of  $\bar{\bar{C}}_i$ . After [2005Gan], certain components may be ignored in the averaging process if deemed necessary. In the present work, the contribution of all elements was considered during data treatment.

In the third step the assignment of fraction solid is defined. All the sites, associated with the original measured compositions  $C_i^j$ , are then reordered according to ascending rank number  $R_i$  and assigned to ascending fraction solid,  $f_s$ , proportional to the rank number:

$$f_s = (R_i - 0.5)/N \quad (5.4)$$

where  $N$ , the total number of sampling points, equals 441 for our grid. The shift of  $(-0.5/N)$  ensures a symmetric distribution of fraction solid values between zero and unity.



## 5.5 The total solute profile during Scheil solidification

Sophisticated solidification micro-models are available for a detailed description of microsegregation, including back diffusion in the solid and other intricacies [1997Kra, 1997Kra1, 2000Boe, 2003Xie]. Such micro-models require, in addition to the complete thermodynamic description, detailed knowledge of kinetic and thermophysical alloy parameters, which are generally not available for magnesium alloys. Therefore the much simpler Scheil solidification model, assuming complete mixing in the residual liquid, equilibrium at the interface to the solid phases and blocked diffusion in the growing solid material [1942Sch] is used. This approach is widely used for practical applications [2002Agr, 2004Cha]. In comparison to microsegregation solute profiles, typically the calculated compositions of the components dissolved in the crystallizing matrix, hcp-(Mg) in the present case, are shown *versus* fraction solid.

This may imply a misleading simplification in comparison to the experimental profile, since it will be shown in this work that both at the very beginning and also in the final stage of solidification different phases (intermetallics) are precipitated or co-precipitated with hcp-(Mg), which should be included in the calculated profile. The solute profile obtained this way will be denoted as “Scheil-total” in present work.

This approach closely follows the Scheil conditions where in each temperature step a new layer of solid phase(s) crystallizes on the already frozen material. The key point is that the *overall composition* of this layer needs to be calculated since up to four different phases may precipitate simultaneously in this layer from our Mg-Al-Zn-Mn alloy, and hcp-(Mg) may be just one of them. This is done in the following way. At the temperature step with number  $i$  we start with a total fraction of residual liquid  $f_L(i)$  of the alloy that adds up with the fraction of entire solid material to unity:

$$f_S(i) + f_L(i) = 1 \quad (5.5)$$

During this temperature step (number  $i$ ) a thin solid layer precipitates, comprising for example three phases  $\alpha + \beta + \gamma$ , and their fractions,  $f(\varphi, i)$ , are defined on the basis of 1 mol of the initial residual liquid, decomposing into these solid phases and a new residual liquid with fraction  $f(\text{liquid}, i)$ , thus

$$f(\alpha, i) + f(\beta, i) + f(\gamma, i) + f(\text{liquid}, i) = 1 \quad (5.6)$$

Typically,  $f(\text{liquid}, i)$  is close to unity in all steps  $i$  and of course different from  $f_L(i)$ . The desired overall composition of Al in this layer,  $\bar{x}(\text{Al}, i)$ , is then given by the following equation:

$$\bar{x}(\text{Al}, i) = \frac{x(\text{Al}, \alpha, i) \cdot f(\alpha, i) + x(\text{Al}, \beta, i) \cdot f(\beta, i) + x(\text{Al}, \gamma, i) \cdot f(\gamma, i)}{f(\alpha, i) + f(\beta, i) + f(\gamma, i)} \quad (5.7)$$

where  $x(\text{Al}, \varphi, i)$  is the composition of Al in any of the solid phases  $\varphi$  of the new solid layer number  $i$ . This value of  $\bar{x}(\text{Al}, i)$  is used in the following "Scheil-total" solute profiles, where the layer number  $i$  is related to the fraction solid in analogy to Eq. (5.4). These equations, written above in terms of molar fractions, may as well be used in terms of wt.%, provided that all phase fractions are also calculated in terms of mass fractions. The numerical values of  $x(\text{Al}, \varphi, i)$ ,  $f(\varphi, i)$  and  $f_L(i)$  are provided by most of the major thermodynamic software packages.

It is our experience that for alloys with four or more components the Scheil solidification path may depend significantly on the temperature step size. Reasonably convergent results are usually obtained if the temperature steps are not larger than 0.2 K, implying a large total number of crystallized layers,  $N'$ , in the order of thousands, during a Scheil simulation. In order to detect a potential accumulation of numerical inaccuracies during these calculations it is advisable to use the following check. The change of the fraction of entire solid material, referring to  $f_S(i)$ , during the growth of the layer number  $i$  is defined by  $\Delta f_S(i)$  with

$$f_S(i+1) = f_S(i) + \Delta f_S(i) \quad \text{and} \quad f_S(1) = 0 \quad (5.8)$$

Based on the individual solid phase fractions in that step we have

$$\Delta f_S(i) = f_L(i) \cdot \{f(\alpha, i) + f(\beta, i) + f(\gamma, i)\} \quad (5.9)$$

This provides an independent numerical check by comparing the accumulated  $\Delta f_S(i)$  of Eq. (5.9) with the total fraction solid, obtained by the software used for the actual Scheil calculation; the following equation

$$f_S(i+1) - \sum_{n=1}^i \Delta f_S(n) = 0 \quad (5.10)$$

should be fulfilled at each value of  $i$ , and especially at the end with  $f_S(N'+1) = 1$ .

All the thermodynamic and Scheil calculations in this work were done with the PANDAT software package [2002Che] and are based on the Mg-Al-Zn-Mn subsystem dataset

[2006Ohn1, 2006Ohn2, 2006Ohn3] of the larger thermodynamic database for magnesium alloys developed in our group [2001Sch]. The alloy compositions denoted as “Before DS” in Tab. 5.1 were used. Local solidification times are presented in Tab. 5.2, calculated from  $(T_{\text{liq}} - T_{\text{sol}})/GV$ . The liquidus and solidus temperatures,  $T_{\text{liq}}$  and  $T_{\text{sol}}$ , were calculated for the specified AZ31 and AM50 alloys using the Scheil conditions since these alloys are known [2006Ohn1] to follow these conditions more closely than equilibrium solidification in the range of  $GV$  values applied here. In order to obtain practically relevant values the temperatures related to  $f_s = 0.0005$  and  $f_s = 0.9995$  were used since minute amounts of primary intermetallic  $\text{Al}_8\text{Mn}_5$  precipitate from AM50 over a temperature range of 14 K and, especially for AZ31, the termination of solidification is not sharp but fades out with minute fraction solid. Values of  $(T_{\text{liq}} - T_{\text{sol}})$  obtained in this way are  $(633-338)^\circ\text{C} = 295^\circ\text{C}$  for AZ31 and  $(627-433)^\circ\text{C} = 194^\circ\text{C}$  for AM50.

## 5.6 Results

### 5.6.1 Reactions between unprotected steel tube and liquid alloy

**Fig. 5.2** shows the cross section of a typical tube-sample interface of an St35 tube filled by AZ62 Mg-alloy (Mg - 6 Al - 2 Zn - 0.5 Mn, wt.%). Contact time liquid/solid is estimated to be shorter than 5 minutes. Even after this short process of just “tube-filling”, the SEM-EDS analysis of the steel close to the contact surface shows an approximately 20  $\mu\text{m}$  deep diffusion zone with Al content in the steel ranging from 1.5 to 23 wt.%. Directly at the contact surface, some Fe-Al particles are also observed.

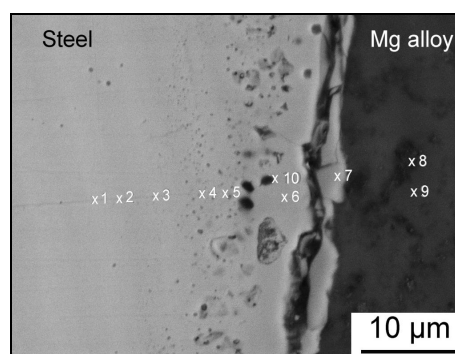


Figure 5.2. Cross section through contact surface between St35 steel tube and AZ62 sample after tube filling; the tube was preheated at  $700^\circ\text{C}$  and filled by  $750^\circ\text{C}$  hot alloy melt and cooled in air; no further processing was performed, though the reaction between sample and unprotected steel is clearly detected; Formation of Fe-Al particles at point 7 (23 wt.% Al) and a diffusion zone (points 6 to 2, 23 to 1.5 wt.% Al) are observed.

Such a filled tube was subsequently held for 12 hours at 650°C. This temperature is 42 K higher than the practical liquidus temperature of the alloy, defined by the start of massive crystallization of the (Mg) phase (Tab. 3.2, section 3.3.1).

After slow cooling in air, the cross section in **Fig. 5.3** shows an approximately 30  $\mu\text{m}$  thick coherent intermetallic compound layer with quite constant Al composition of about 26 wt.% Al and 74 wt.% Fe iron, or  $\text{Fe}_{58}\text{Al}_{42}$  (at.%). Beneath that compound layer an approximately 20  $\mu\text{m}$  deep interdiffusion zone is also existent in the steel, even though it is not obvious on that micrograph.

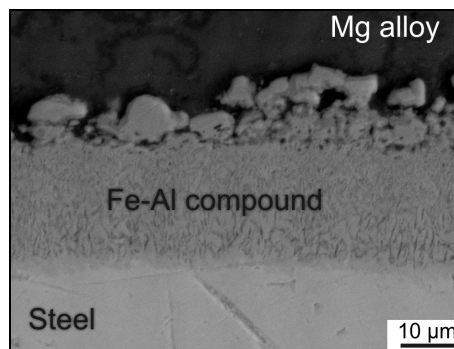


Figure 5.3. Reaction between sample and unprotected steel (BSE micrograph); St35 steel+AZ62; filled (700°C preheated tube, cooled in air), hold for 12h at 650°C and slowly cooled down; Approximately 30  $\mu\text{m}$  thick layer built of Fe-Al compounds is observed; mean composition 74 wt.% Fe and 26 wt.% Al.

After a much longer contact time of 19 days at 650°C between St35 and AZ62 Mg-alloy virtually the same intermetallic layer thickness was observed ( $\sim 30 \mu\text{m}$ ). Differing from the 12 h experiment, approximately 30  $\mu\text{m}$  big  $\text{Fe}_{65}\text{Al}_{35}$  blocky particles are observed, detached from but close to the intermetallic layer and floating into the Mg-melt. This transfer of iron-rich particles into the Mg-melt may eventually result in what is known as the "formation of intermetallic sludge" [2003Tan, 2007Sch].

The alternative V4A steel was also tested for 19 days at 650°C in contact with AZ62 and AZ91 melts. Interface investigation showed a behavior similar to St35 steel. A diffusion zone, the coherent Mn-free intermetallic layer and floating compound blocks are also observed. Differing from St35, about 6 wt.% Cr and 5 wt.% Ni are found in addition to Al and Fe in the intermetallic layer. Furthermore, the occurrence of blocky compound particles is slightly less pronounced compared to St35.

All these significant reactions occur even though 650°C is well below the temperature necessary for the actual directional solidification. Preliminary experiments comprised also DS of AZ91 alloy within the V4A steel tube. The tube spent about 2 hours in contact with the melt heated at 800°C. Similar to the previous experiments, the composition of the intermetallic layer forming is dominated by Al and Fe, containing also Cr and Ni. The significant difference observed was the presence of manganese in the compound layer, ranging up to 7 wt.% Mn. The formation of large detached intermetallic particles was also clearly observed. The particles, typically containing Mg - 28 Al-17 Mn- 42 Fe- 8 Cr- 5 Ni (wt.%), are often observed far away from the inner tube surface. These particles are also often observed within the  $\gamma$ -phase particles. Thus, an impact of this container wall reaction and these particles on the directional solidification process cannot be excluded. More details on the reaction between unprotected steel tube and liquid alloy are given in Appendix B, Cases 1-3.

### 5.6.2 Performance of BN-coated steel tubes

**Fig. 5.4** shows the cross section of a steel tube with Type-V coating and AM50 alloy after passage through the Bridgman furnace at 720°C target temperature. The inset shows a magnification at the interface. It is obvious that this BN-coating successfully prevents melt attack during exposure time of roughly 1 hour. Within experimental accuracy, no Al in the steel next to the coating was found by the EPMA-WDS analysis. This optimized BN-coating fulfilled its protective function, even though the initially equal thickness and polished coating surface changed marginally.

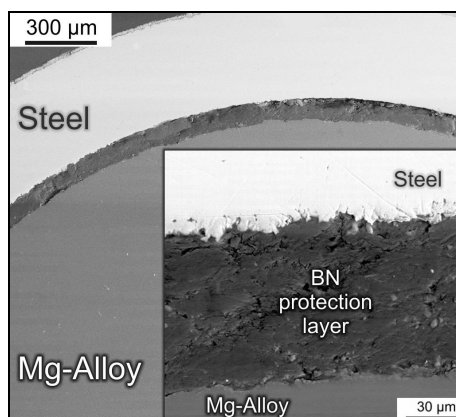


Figure 5.4. Contact surface between AM50 and St35 steel tube (BSE micrograph) after about 1-hour exposure to the melt at 720°C; optimized BN coating fulfilled its protective function, whereas the initially equal thickness and polished coating surface only marginally changed; according to measuring accuracy no Al was detected in steel (EPMA-WDS)

Unpolished Type-V coating combined with St35 steel was also tested, but not shown here. Decreased protection ability with unpolished BN-coating, occasionally deeply intruded by Mg-melt was observed (Appendix B, Case 4). The unpolished coating probably increases the wettability of BN coating by the Mg-melt. It is worth noting that the combination of polished Type-V coating with V4A stainless steel performs not as good as with mild steel St35, even if specifically the same coating process and solidification conditions are applied.

The limitations of the optimized coating-steel combination are also revealed. Extensive experiments showed that the melt temperature was the key factor limiting the protective function. **Fig. 5.5** shows a BSE micrograph of magnified contact surface of St35 steel tube protected by polished Type-V coating after around 2 hours of exposure to the liquid AZ31 alloy at 800°C. This temperature stresses the BN coating to its limit, whereas the same layer performed perfectly at 720°C. At 800°C a marginal Al diffusion zone of less than 5 µm in the steel was also observed, where Mn was not detected. The protective functionality is probably deteriorated due to melt soaking into the BN layer. The small bright particles in Fig. 5.5 are probably an artifact from grinding steel particles, trapped within the softened soaked BN layer. It is interesting that the BN layer partly remained undamaged in the darker band at the bottom side. Nevertheless, even this band was not capable of preventing melt intrusion.

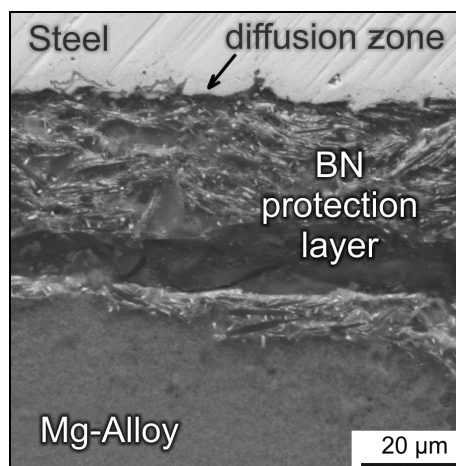


Figure 5.5. Contact surface between AZ31 and St35 steel tube (BSE micrograph) after about 2-hour exposure to the melt at 800°C; The high temperatures (800°C in this case) stress the BN layer to the limit of its resistance; Attack by Mg-melt and partly soaked BN layer are observed; slight diffusion zone of less than 5 µm in the steel was also observed; possible explanation is given in text.

The coating protective efficiency was also tested by analysis of the change in Al composition of the sample. This was done using ICP-AES analysis of alloy samples after directional solidification and removing of the tube by grinding. The samples were cut out directly above the quenched solidification front. The results are highlighted by bold font in

Tab. 5.1. The data "After DS" are sorted with increasing melt temperature and time (decreasing solidification rate) of the melt/tube contact. Only minor Al and Mn losses are observed in the case of 720° furnace (melt) temperature for both the AZ31 and AM50 alloys. The data for AM50 alloy are detailed in Chapter 6 of this thesis. Larger losses are generally observed at 800°C.

This is consistent with the appearance of corresponding BN coatings after directional solidification. For both investigated alloys the significantly stronger melt attack is always observed for 800°C melt temperature. It is also worth noting that the Zn content of AZ31 in Tab. 5.1 appeared virtually unaffected by sample preparation and subsequent directional solidification. No clear impact of the two solidification rates, resulting in roughly doubling the melt-tube contact time from 1 to 2 hours, on the loss of alloying elements was observed.

Another significant difference observed regards the removing of the steel tube after DS experiment. After lateral grinding the steel tube at opposite sides, the two BN coated tube halves were easily detached from the sample. On the contrary, strong tube/sample sticking was observed in the case of uncoated tube.

### 5.6.3 Microstructure in the mushy zone near the solidification front

All results reported below refer to experiments using the optimized polished Type-V BN coated St35 steel tubes. A light optical microscopic micrograph of the quenched mushy zone of AZ31 sample grown at  $GV = 0.811$  K/sec before quenching is shown in **Fig. 5.6**. A three dimensional mushy zone presentation with both longitudinal and cross-section cut is presented in Fig. 5.6a. The individual dendrite stems are clearly resolved. Small deviations regarding the dendrite stem orientation with respect to the axial direction of the tube are observed.

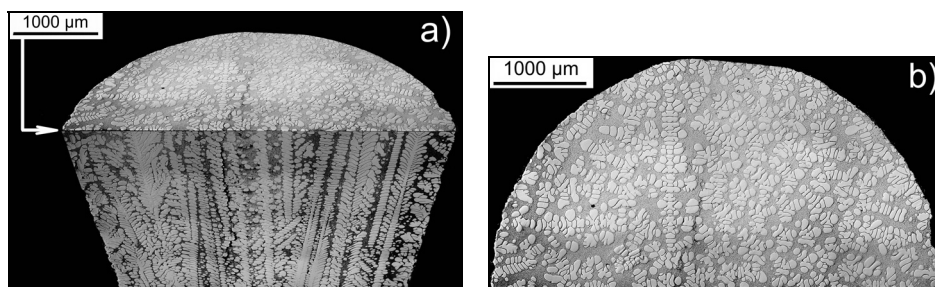


Figure 5.6. Quenched mushy zone; light microscope micrograph of AZ31 alloy solidified at  $GV = 0.811$  K/sec

- a) 3D mushy zone presentation where both longitudinal and cross-sectional cuts are merged; the individual dendrite stems are clearly resolved
- b) Cross section just behind the tips of the dendrites; the dendrites with secondary arms in three directions around the stem are observed

The influence of the  $GV$  value on the mushy zone morphology is studied systematically in Chapter 6 of this thesis. Fig. 5.6b shows a cross section, normal to the solidification direction, just behind the tips of the dendrites. The dendrites with secondary arms in three directions around the stem are dominating. No significant edge effect on the dendritic microstructure near the tube wall is observed. Only few crystals starting their growth at the tube wall were found.

#### 5.6.4 EPMA-WDS microsegregation data beneath the mushy zone

##### 5.6.4.1 Solute compositional maps

As an example, the Al, Zn and Mn compositional maps of AZ31 alloy solidified at  $GV = 0.381$  K/sec are shown in Fig. 5.7a. The scanned area is taken from a cross section beneath the dendrite roots where the sample was completely solidified before quenching. A systematic comparison of compositional maps is shown in Chapter 6 of this thesis for all four cooling rates.

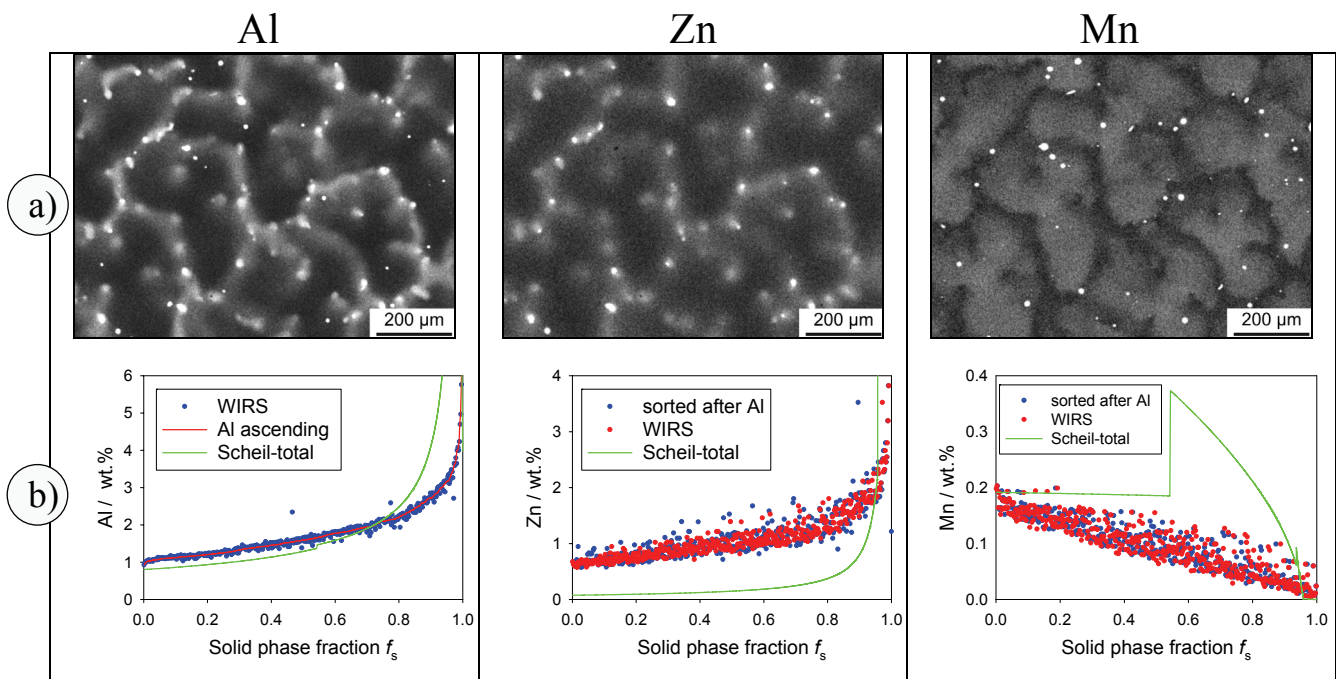


Figure 5.7. AZ31 sample solidified at  $GV = 0.381$  K/sec  
 a) Cross sectional qualitative EPMA-WDS compositional maps of Al, Zn and Mn; brighter areas indicate solute rich regions.  
 b) Corresponding quantitative Al, Zn and Mn solute profiles, each determined by three methods.

The dendritic microstructure is obvious in this cross section. The gray scale shows the varying contents of the segregated components in the Mg alloy. The brighter gray nuances



indicate solute rich regions. Both Al and Zn are segregating into interdendritic regions, whereas manganese shows opposite segregation behavior. The Zn-rich particles are found always in interdendritic regions, typically at the same locations where Al enrichment was observed. This implies an existence of Mg-Al-Zn compounds, such as  $\gamma$ -Mg<sub>17</sub>Al<sub>12</sub> or the  $\phi$  phase. The bright particles showing simultaneously Al and Mn enrichment are observed both in the interdendritic regions and also within the dendrite stems.

The interdendritic microstructure of this sample is shown magnified in **Fig. 5.8**. The four phases, Al<sub>8</sub>Mn<sub>5</sub>,  $\gamma$ -Mg<sub>17</sub>Al<sub>12</sub>,  $\phi$  and (Mg) are revealed by the mass contrast in this back scattered electron (BSE) image. The  $\phi$  phase was observed both as stand-alone particle, but also together with  $\gamma$ -Mg<sub>17</sub>Al<sub>12</sub> phase, as shown in magnified inset (top left). The EPMA analysis of these particles provides the following mean phase compositions: Al<sub>8</sub>Mn<sub>5</sub>: Al60-Mn40;  $\gamma$ -Mg<sub>17</sub>Al<sub>12</sub>: Mg60-Al33-Zn7;  $\phi$ : Mg60-Al24-Zn16 (at.%).

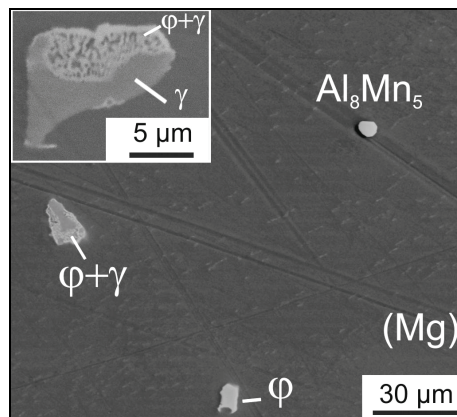


Figure 5.8. BSE image of the magnified interdendritic area from Fig. 5.7a. The four phases, Al<sub>8</sub>Mn<sub>5</sub>,  $\gamma$ -Mg<sub>17</sub>Al<sub>12</sub>,  $\phi$  and (Mg) were observed. The EPMA analysis shown following mean phase compositions, all in at.%. Al<sub>8</sub>Mn<sub>5</sub>: Al 60, Mn 40;  $\gamma$ -Mg<sub>17</sub>Al<sub>12</sub>: Mg 60, Al 33, Zn 7;  $\phi$ : Mg 60, Al 24, Zn 16.

#### 5.6.4.2 Quantitative EPMA data and solute profiles

For the same sample as given above (AZ31 solidified at  $GV = 0.381$  K/sec) the solute-solvent correlation relationships is shown in **Fig. 5.9**. All the 21·21=441 grid point composition quadruples from the quantitative segregation mapping of a 1000 x 1000  $\mu\text{m}^2$  area are presented here. The opposite segregation behavior of Mn compared to both Al and Zn is obvious in this presentation. This provides a quantitative, unbiased basis for step 1 of the WIRS scheme, the determination of normal and inverse partitioning directions.

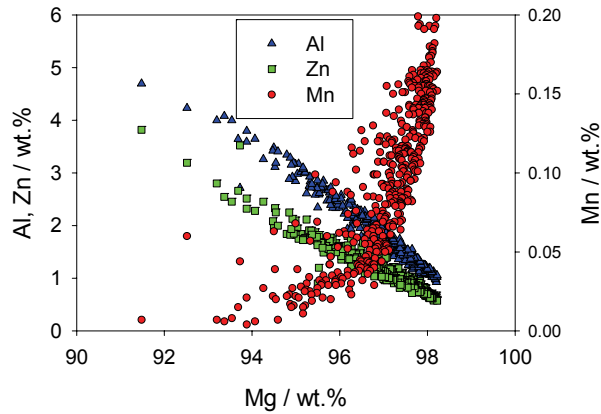


Figure 5.9. Solute-solvent correlation relationship in AZ31 after directional solidification at  $GV=0.381$  K/sec. The opposite segregation behavior of Mn compared to both Al and Zn is obvious.

The average compositions of Al, Zn and Mn, calculated from all 441 measured points, are given in Tab. 5.1, denoted as “EPMA”; the deviation from the ICP-AES data will be discussed later. The Al, Zn and Mn solute profiles determined by WIRS and Al-leading sorting scheme are compared to Scheil-total solute profile in **Fig. 5.7b**.

#### 5.6.4.3 The total solute profile during Scheil solidification and comparison to WIRS data

The Al content in the solid phase(s) during the Scheil solidification of AZ31 alloy is shown in **Fig. 5.10**. The dashed line shows the conventional presentation of the Al content only within the hcp magnesium solid solution (Mg). The monotonous increase is obvious until the precipitation of the  $\gamma$ -Mg<sub>17</sub>Al<sub>12</sub> phase starts at  $f_S = 0.96$ . The *total Al content* considering all Al-containing solid phases appearing during solidification (Scheil-total) is given as solid line in Fig. 5.10. The arrow 1 at  $f_S = 0.54$  marks first deviation due to appearance of the Al<sub>8</sub>Mn<sub>5</sub> phase. This phase increases the total Al content only slightly. The next deviation to the dashed line is significant and related to the start of the  $\gamma$ -Mg<sub>17</sub>Al<sub>12</sub> phase precipitation at  $f_S = 0.96$  (arrow 2), resulting in much larger and more realistic Al content in the Scheil-total curve. The transformation sequence Al<sub>8</sub>Mn<sub>5</sub>  $\rightarrow$  Al<sub>11</sub>Mn<sub>4</sub>  $\rightarrow$  Al<sub>4</sub>Mn is not indicated since it affects the mean Al content only slightly.

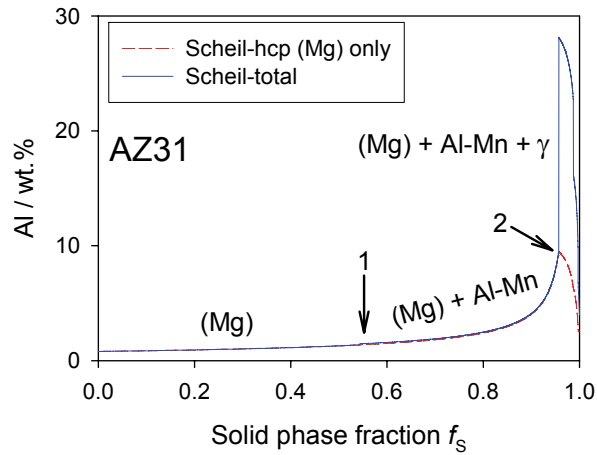


Figure 5.10. Solid phase Al content in the course of Scheil solidification of AZ31 alloys

- Scheil-hcp (Mg) only - only Al contained in Mg solid solution is considered;
- Scheil-total - all Al containing phases appearing during solidification are considered;

Arrow 1 at  $f_s = 0.54$  marks first deviation due to appearance of  $\text{Al}_8\text{Mn}_5$  phase;  
 Arrow 2 at  $f_s = 0.96$  marks occurrence of  $\gamma\text{-Mg}_{17}\text{Al}_{12}$  phase

At the very beginning of solidification, for solid fractions ranging from zero to 1%, both the Mn and Al Scheil-total solute profiles are given for AM50 alloy in **Fig. 5.11** by solid and dashed line, respectively. The high Al and Mn contents occurring simultaneously at the start of solidification are related to the  $\text{Al}_8\text{Mn}_5$  primary phase precipitation. It is worth noting that the temperature interval between the bend points marked by the arrows at  $f_s = 0.0008$  and  $f_s = 0.0073$  represents the temperature step size minimum of only 0.1 K.

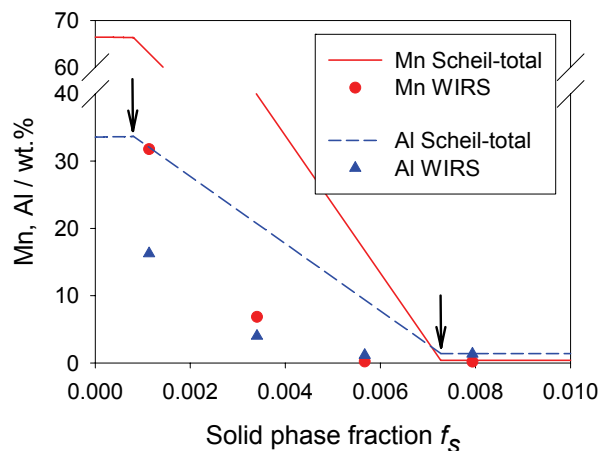


Figure 5.11. Al and Mn solute profiles defined by Scheil-total and WIRS for AM50 alloy solidified at  $G\dot{V} = 0.811$  K/sec, initial stage; primary Al-Mn particles are observed in the microstructure and also confirmed by WIRS.

The experimental Mn and Al WIRS solute profile data for the same alloy solidified at  $GV = 0.811$  K/sec are also shown in Fig. 5.11. Compared with the Scheil-total curves the same trend is clearly observed for the experimental data. This agrees also well with the presence of Al-Mn particles, which are observed in the microstructure of the corresponding AM50 sample (Fig. 6.6 in Chapter 6). It is emphasized that this significant result is obtained because both the advanced Scheil-total simulation and the advanced WIRS sorting scheme was used. The conventional Scheil-hcp and Al-leading-element sort inherently preclude such an initial decrease in the solute profile.

## 5.7 Discussion

### 5.7.1 Sample container and directional solidification

#### 5.7.1.1 Steel tubes without and with BN protection

The results of our experiments with St35 steel and AZ62 Mg-alloy (section 5.6.1) may be compared to those of [2003Tan] immersing the H13 steel into molten Mg-Al alloys with Mn at 680°C (section 5.2.3). Some discrepancies appeared with respect to Mn content within the intermetallic layer. No manganese was found by investigation of our samples tested at 650°C independent on the steel type (both St35 and V4A) or contact time (12 h and 19 days). Slight increase of the Mn content in intermetallic layer was observed in this work only in the case of V4A steel and AZ91 alloy after 2 h in contact with the melt at 800°C.

[2003Tan] reported also about significant aggravation of Al-Fe reaction for Mg alloys with more than a critical content of 7 wt.% Al. In this work no major difference between Mg alloys with 6 and 9 wt.% Al was observed if uncoated steel tube was applied.

The presence of the intermetallic layer at the melt-tube interface may also be detrimental because of abnormally low thermal conductivity of the Al-Fe intermetallic phases, as mentioned by [2002Sha1]. This effect could negatively influence the uniformity of the temperature field during directional solidification. Floating intermetallic particles are also suspected to disturb the directionally solidified microstructure.

Another most significant impact is the Al loss of the sample because of its large surface to volume ratio. This is shown by a simple materials balance calculation for the AZ31 alloy. Let us assume the formation of a 20  $\mu\text{m}$  thick intermetallic layer with averaged 10 wt.% Al, well below the 30  $\mu\text{m}$  layer with 26 wt.% Al in Fig. 5.3. Even such minor layer formation reduces the initial 2.6 wt.% Al of the liquid alloy by a factor of 0.77, that is from 2.6 to 2.0 wt.% Al.

---

Such substantial change in the sample composition is certainly unacceptable, emphasizing the necessity to apply protective measures against the sample/steel reaction.

Comparing these numbers to the ICP-AES measured Al compositions before and after DS demonstrates the effectiveness of the optimized BN protection applied in this work.

The polished Type-V BN coating is considered a solution in order to prevent or at least significantly suppress the negative effects of the melt/tube reaction.

#### 5.7.1.2 Impact of steel sort: St35 versus V4A

It is noted that the combination of polished Type-V coating with V4A stainless steel performs not as good as with mild St35 steel; this was observed for same coating application and solidification conditions. The coating-steel interaction thus also influences coating efficiency and should not be neglected. A possible explanation may be the about 30% larger mean linear thermal expansion of austenitic V4A steel compared to ferritic St35 steel ( $19^1$  versus  $14.7 \cdot 10^{-6} \text{ K}^{-1}$  [1971Lan]). It is assumed that a larger expansion mismatch to BN could abet crack formation in the BN layer on V4A steel.

#### 5.7.1.3 Application of non-ferrous tube materials

The four non-ferrous materials tested by [2001Sha1] are difficult to apply as thin walled tubes, as they are all manufactured by powder metallurgy. Another restriction is the lower temperature ( $625^\circ\text{C}$ ) of Al melt these materials were exposed to by [2001Sha1], compared to the present work ( $720$  and  $800^\circ\text{C}$ ). Even if pure Al melt is more aggressive than molten Mg-Al alloys, the impact of the temperature is more pronounced, as stressed by [2002Sha1] and also confirmed in this work. Although considerably better than H13 steel, the best performing tungsten-based alloy approved by [2001Sha1] may not be regarded as ultimate solution providing absolute protection at higher temperature.

Tantalum was also regarded as possible solution. Both tantalum tubes, as well as galvanic coating of steel carrier by thin Ta layer were taken in consideration, but presently rejected for following reasons: Tantalum tubes offer good protection, but fails on the high Ta oxygen affinity. It demands some protection (gas protection or tube-in-tube system), significantly impeding filling of the tube, as well as subsequent directional solidification. Tantalum coating was rejected since no appropriate coating method was found.

---

<sup>1</sup> <http://www.smt.sandvik.com/tube>

---

#### 5.7.1.4 Bridgman equipment

The generation of a well defined temperature gradient over the alloy's freezing zone is a key parameter of the Bridgman equipment. A steeper temperature gradient improves orientation homogeneity of growing dendrites. The simplest way is to achieve that is to increase the furnace temperature, which also results in a better linearity of the temperature profile that is a more constant temperature gradient within the solidification range.

However, for the Mg-Al alloys it was shown in section 5.6.2 that a higher furnace (melt) temperature aggravates the sample-tube reaction during directional solidification. Therefore, all other measures have to be taken in order to achieve a sufficient temperature gradient while keeping the furnace temperature as low a possible. The strongest effect was attained by cooling trap reconstruction, initially designed as closed water cooled jacket. The direct tube-water contact significantly improves cooling efficiency. The water inlet was also optimized to a sprinkling coil placed around the immersed sample tube directly at the water surface. Additional furnace temperature reduction of 40 K, while retaining the temperature gradient, was attained by decreasing the distance between heating element and cooling trap (water surface). This is achieved by reducing the thermal insulation thickness below the steel block and by narrowing the air gap underneath.

The thermal conductivity of the steel tube is recognized as another factor with a potential impact on the temperature gradient. The austenitic stainless steel V4A exhibits significantly lower thermal conductivity (23 W/m·K) compared to ferritic steel St35 (38 W/m·K at 600°C). The lower thermal conductivity of the V4A steel enables steeper axial temperature gradient within the tube at the same furnace temperature. This is experimentally confirmed ( $G = 12.1$  versus  $9.8$  K/mm at 720°C furnace temperature, secant method for 600°C/400°C range); admittedly, the temperature profile linearity is worse. In spite of this positive potential to slightly reduce furnace temperature while retaining the temperature gradient, V4A steel was finally not accepted due to its inferior compatibility with BN coating, as discussed in section 5.7.1.2. A possible impact of the relatively high heat conductivity of BN coating on  $G$  was also tested but no difference was observed with or without BN in the St35 steel tube.

The influence of tube wall thickness was also checked. Two V4A tubes with 6 mm outer diameter and 0.5 and 1 mm wall thickness are compared at the same conditions and small difference was also observed ( $G = 12.1$  to  $10.9$  K/mm at 720°C furnace temperature). The thinner wall, taken as final solution, is also beneficial with respect to increasing sample volume/surface ratio at given 6 mm outer diameter. This effects less relative Al-loss, if the same thickness of Al-Fe intermetallic layer is assumed.

---

### 5.7.2 Issues regarding quantitative EPMA mapping

Even if measurement and prediction of alloy microsegregation by quantitative x-ray mapping is a well established method in general, it is still not trivial and its interpretation may be subject to various sources of errors as detailed by Lacaze et al. [2003Lac]. Two basic checks are suggested. The first check is a comparison of bulk alloy composition to the average EPMA composition of the area analyzed. The average EPMA compositions of Al, Zn and Mn in Tab. 5.1 show some discrepancy to the chemical ICP-AES analysis. This discrepancy may be explained by existence of particles with much higher composition of Al, Zn and Mn than the matrix, impeding a valid statistical sampling by the grid. Other possible reasons given by [2003Lac], e.g. unrepresentative area selection or macrosegregation are found not to be applicable in the present study. The second test, that the sum of elements should total 100 wt.% at each point, is perfectly passed. The maximal difference amounts to only  $\pm 0.26$  wt.% with 99% confidence. We agree with [2003Lac] that this is a crucial test for the applicability of the spot mode for multiphase materials.

### 5.7.3 EPMA data sorting: Comparison of leading-element sort to WIRS

This study confirms the proposition of [2005Gan] that the WIRS sorting scheme is preferable since it requires no operator judgment, it is physically reasonable and it exploits all the information in the data set. They emphasize that WIRS is especially suitable if alloys with many components are analyzed, such as superalloys which may have up to 10 components; in that case the final solute profiles may be significantly influenced by operator subjectivity, choosing a leading element. Ganesan et al. [2007Gan] also applied WIRS recently to the 319 Al-alloys, containing Cu and Si as the two major alloying elements. Even though the sorting after descending Al content appeared reasonable, an important limitation was highlighted. It is the uncertainty in the measurement of the leading element, which is transferred into noise in other components. This phenomenon is also observed in Fig. 5.7b. Compared to WIRS, the leading-Al sort results into an unrealistic smooth and monotonous Al solute profile whereas the Zn and Mn profiles exhibit a significantly stronger scatter.

Moreover, it is demonstrated in the present work that the WIRS scheme is capable of better describing the phase sequence during solidification, whereas the leading-Al sort is not. It was stated previously [2003Lac, 2005Gan, 2005Kur] that sorting schemes based on a *single selected solute* with monotonously ascending/descending content may not describe the correct phase sequence during solidification. In this work the leading-element sort (Al) is also found to be incapable to reveal primary precipitation of the  $Al_8Mn_5$  phase characteristic for the

---

solidification of the AM50 alloy. The primary solidification of the phase is predicted by Scheil-total calculation and confirmed by the investigation of the microstructure, where the needlelike precipitates were observed (Chapter 6). In fact, the WIRS sorting scheme is capable to reveal the occurrence of such primary Al-Mn intermetallics during the initial stage of solidification, as shown in Fig. 5.11.

#### 5.7.4 WIRS solute profiles compared with Scheil-total

During the main stage of solidification of the AZ31 alloy a qualitative agreement is shown in Fig. 5.7b between the experimental WIRS and the calculated Scheil-total solute profiles. There are several reasons for the quantitative discrepancies.

Firstly, the integrated area under each Scheil-total curve is of course identical to the bulk composition assumed for the calculation and taken as "Before DS" in Tab. 5.1, whereas the average WIRS data are also given by the second "EPMA" entry line for 720°C/38.9  $\mu\text{m}/\text{sec}$ , valid for the  $GV$  value of that sample. The largest difference of 2.63 versus 1.83 wt.% is clearly reflected even in the visual inspection of the Al-profiles in Fig. 5.7b. It is to be noted that the visual integral of the Mn-profile appears very low for the EPMA data since some very high Mn compositions, related to particles, are way above the scale limit.

Moreover, substantial back-diffusion obviously appears for both Al and Zn, significantly decreasing the experimental solute composition gradient at the high end, compared to the blocked diffusion of the Scheil-total profiles. It becomes evident that a more sophisticated micro-model of solidification, incorporating back-diffusion and other effects, is required for a quantitative description of the solute profiles of this magnesium alloy.

## 5.8 Conclusions

The study of directional solidification in a Bridgman experiment is not trivial for alloys containing both Mg and Al. These liquid alloys are highly reactive and attack standard ceramic as well as metallic container materials. This is demonstrated by the extensive reaction of various unprotected steel grades even after only 5 minutes of melt contact. An integrated approach comprising dedicated BN protection of selected St35 steel tube material and limiting the melt temperature while retaining sufficiently high thermal gradients was developed. It performs well for experiments with melt/tube contact of over 75 minutes at 790°C.

It is shown that an advanced processing of quantitative EPMA mapping data using the "weighted interval rank sort" (WIRS) [2005Gan] is superior to the widely used leading-

---



element sort. Even the minute amount of primary crystallizing Al-Mn intermetallic compound from an AM50 Mg-alloy can be revealed from the EPMA data using the WIRS scheme.

The simplest approach of thermodynamic calculation of segregation during solidification, the Scheil method, is also extended to reflect not only the solute profiles of components dissolved in the main matrix, hcp-(Mg), but all precipitating phases. This "Scheil-total" profile is more realistic and its integral reflects the bulk composition of a multiphase alloy. It also predicts the experimentally detected primary crystallizing Al-Mn intermetallic phase.

The methodology developed in the present chapter of this study for Mg-Al alloys, and exemplified essentially with selected data of an AZ31 Mg-alloy, is used as a basis for a systematic and comparative study of two magnesium alloys, AZ31 and AM50, in Chapter 6 of this thesis.

---

## **6 Directional solidification of Mg-Al alloys and microsegregation study of Mg alloys AZ31 and AM50.**

### **part II: Systematic comparison between AZ31 and AM50**

#### 6.1 Introduction and procedures

Details on the background of this study on solidification and microsegregation of magnesium alloys are given in Chapter 5 of this thesis. The main purpose of the present Chapter 6 is a comprehensive comparison of the AZ31 and AM50 alloys with respect to their solidification behavior during directional solidification (DS), including a systematic variation of cooling rate. The microstructure and microsegregation developed during directional solidification are in the focus of this comparison. The solute segregation behavior and corresponding solute profiles obtained by processing of EPMA data were analyzed in-depth in this work. Moreover, details are presented here for the alloy AM50 that may be compared to the data given for AZ31 in the methods-oriented Chapter 5.

These magnesium alloys are widely used especially for automotive applications. The AZ31 is known as a good wrought alloy; it is commonly processed by rolling and forging/extrusion. The AM50 is a general casting alloy providing good strength and ductility [2007Kul]. For both applications, extrusion and casting, the primary solidification and apparent microstructure are crucial for subsequent processing and final product quality. Even though, the microstructure formation and evolution during solidification is still not fully understood, as recently stated by [2005Ger] for AM50 and similar die cast alloys. Gertsman et al. [2005Ger] recently reported about microstructure and second-phase particles in low- and high-pressure die cast AM50 alloy.

Related work concerns the much more common magnesium alloy AZ91. Pettersen et al. [1989Pet, 1990Pet] studied dendrite stem crystallography of directionally solidified AZ91. They found that the stem direction depends on the interplay of temperature gradient,  $G$ , and growth velocity,  $V$ . Mathiesen [1988Mat] studied primary dendrite spacing as function of  $GV$  of the AZ91 alloy.

The methodology used for the comparison of the AZ31 and AM50 alloys is based on a customized directional solidification technique, presented in Chapter 5 of this thesis. This improved experimental procedure comprises sample tube material and its protective coating, filling of tubes and DS procedure, and finally microstructure and microsegregation

---

characterization. The dedicated processing of the quantitative EPMA data as well the calculation of the Scheil-total solute profiles are also specified in Chapter 5.

Details on the starting material and compositions of the alloy AZ31 are also given in Chapter 5 of this thesis. The ingot chemical composition of the alloy AM50 is shown in **Tab. 6.1**, where the Fe, Cu and Ni contents are not shown, being less than 50  $\mu\text{g/g}$ . The ingot chemical compositions, as well as compositions related to subsequent sample preparation stages listed in Tab. 6.1, are provided by in-house chemical laboratory using Inductively Coupled Plasma Atomic Emission Spectroscopy (ICP-AES). The parameters relevant for directional solidification in the Bridgman equipment are the same as given in Chapter 5 (Tab. 5.2, section 5.3.4).

**Table 6.1.** Chemical composition [wt.%] of investigated AM50 samples as ingot, before and after directional solidification (DS), balance Mg. EPMA is related to the mean value of all 441 points measured on the  $1 \times 1 \text{ mm}^2$  area.

Sample AM50	Furnace temperature, $^{\circ}\text{C}$	$V$ , $\mu\text{m/sec}$	Comment	Al	Zn	Mn
Ingot	-	-	ICP-AES	4.63	0.035	0.28
Before DS	-	-	<b>ICP-AES</b>	<b>4.39</b>	<b>0.022</b>	<b>0.30</b>
After DS	720	82.8 <sup>c)</sup>	<b>ICP-AES</b>	<b>4.11</b>	<b>0.019</b>	<b>0.15</b>
			EPMA	2.94	0.025	0.176
		38.9 <sup>a)</sup>	<b>ICP-AES</b>	<b>4.16</b>	<b>0.020</b>	<b>0.067</b>
			EPMA	2.57	0.027	0.043
	800	82.8 <sup>d)</sup>	<b>ICP-AES</b>	<b>3.14</b>	<b>0.021</b>	<b>0.14</b>
			EPMA	1.65	0.030	0.03
		38.9 <sup>b)</sup>	<b>ICP-AES</b>	<b>3.72</b>	<b>0.024</b>	<b>0.31</b>
			EPMA	1.50	0.030	0.002

Conversion to cooling rates,  $GV$ : <sup>a)</sup> 0.381, <sup>b)</sup> 0.614, <sup>c)</sup> 0.811, <sup>d)</sup> 1.31 K/sec

## 6.2 Results and discussion

### 6.2.1 Difference between AZ31 and AM50 regarding the performance of BN-coated steel tubes

One of the present methods for testing the coating protective efficiency is the analysis of the change in Al composition of the sample, caused by the reaction of Al solute with the steel

tube. This was done using ICP-AES analysis of alloy samples after directional solidification and removing of the tube by grinding. The samples for chemical analysis were cut out directly above the dendrite tips of the quenched solidification front. The results are highlighted by bold font in Tab. 6.1 and may be compared to the corresponding Tab. 5.1 for AZ31 in Chapter 5. The data "After DS" are sorted with increasing melt temperature and time of the melt/tube contact, reflected by decreasing solidification rate. Only minor Al- and Mn-losses are observed in the case of 720°C furnace (710°C melt) temperature for both the AZ31 and AM50 alloys in the ICP-AES data. Larger losses are generally observed at 800°C. This is particularly valid for AM50 alloy, where significantly increasing Al-loss compared to AZ31 alloy is observed.

This is consistent with the appearance of corresponding BN coatings after directional solidification. For both investigated alloys the much stronger melt attack is always observed for 800°C melt temperature. Comparing the AZ31 and AM50 alloys, the stronger melt attack is observed for AM50 alloy. It remains unclear if this is only due to the higher Al content of nominally 5 compared to 3 wt.% Al; the presence of Zn in AZ31 may cause differing physical properties, such as viscosity or surface tension, which might play a more important role in penetrating the protective layer. It is also worth noting that the Zn content of AZ31 and AM50 (Tab. 6.1) appeared virtually unaffected by sample preparation and subsequent directional solidification.

### 6.2.2 Microstructure in the mushy zone near the solidification front

A light optical microscopic micrograph of the quenched mushy zone of AM50 sample grown at  $GV = 1.31$  K/sec before quenching is shown in **Fig. 6.1**. A three dimensional mushy zone presentation with both longitudinal and cross-section joined together is presented in Fig. 6.1a. The individual dendrite stems are clearly resolved. Only minor deviations regarding the dendrite stem orientation with respect to the axial direction of the tube are observed. Fig. 6.1b shows a cross section, normal to the solidification direction, within the mushy zone. The dendrites with secondary arms in three directions around the stem are dominating. No significant edge effect on the dendritic microstructure near the tube interface is found. The coaxial cracks observed in the cross section are due to the thermal stress during the quenching.

---

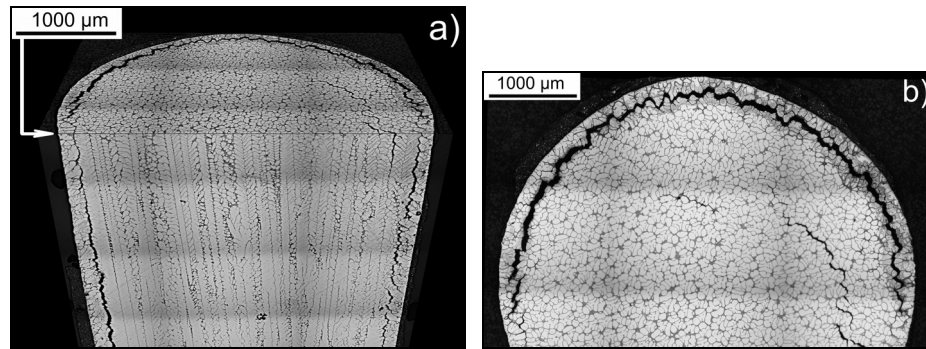


Figure 6.1. Quenched mushy zone; light optical microscopic (LOM) micrograph of AM50 alloy solidified at  $GV = 1.31$  K/sec

- a) 3D mushy zone presentation where both longitudinal and cross-sectional cuts are joined together; the individual dendrite stems are clearly resolved
- b) cross section within the mushy zone; the dendrites with secondary arms in three directions around the stem are observed

The mushy zone morphology of AM50 and AZ31 alloys as a function of the applied cooling rate  $GV$  is shown in **Figs. 6.2 and 6.3**, respectively. The typical distance from the dendrite tips to the water level of the cooling trap was 70-75 mm, irrespective of the solidification conditions. During the quasi-stationary state it is assumed that the dendrites growth velocity equals the preset downward speed of the sample in the Bridgman equipment. This may not be applicable during the initial solidification stage and for primary stems tilted relative to the sample axis. The investigation of the cross sections showed that after 30 mm solidification length, or less, the quasi-stationary dendritic growth conditions were established. Within the first 30 mm a stronger edge effect of the tube wall and insufficient axial dendrite alignment were observed. All samples were solidified at least over a length of 100 mm with the preset solidification rate before quenching.

It is noted that for both alloys the deviation regarding the dendrite stem orientation with respect to the axial direction of the tube is much more pronounced for  $GV$  values 0.381 and 0.811 K/sec. These  $GV$  values relate to the lower temperature gradient (9.8 K/mm) obtained by the lower furnace temperature of 720°C. The axial misalignment is even more obvious in the case of alloy AM50 where severe side branching was observed.

It is also clearly observed that increasing cooling rate  $GV$  imply refinement of the dendritic microstructure. The crossover from coarse trunks and side branches to the fine primary dendrite stems and secondary and tertiary arms is observed. Even by the bare eye, the finer dendrite microstructure of the AZ31 alloy is recognizable, compared to AM50.

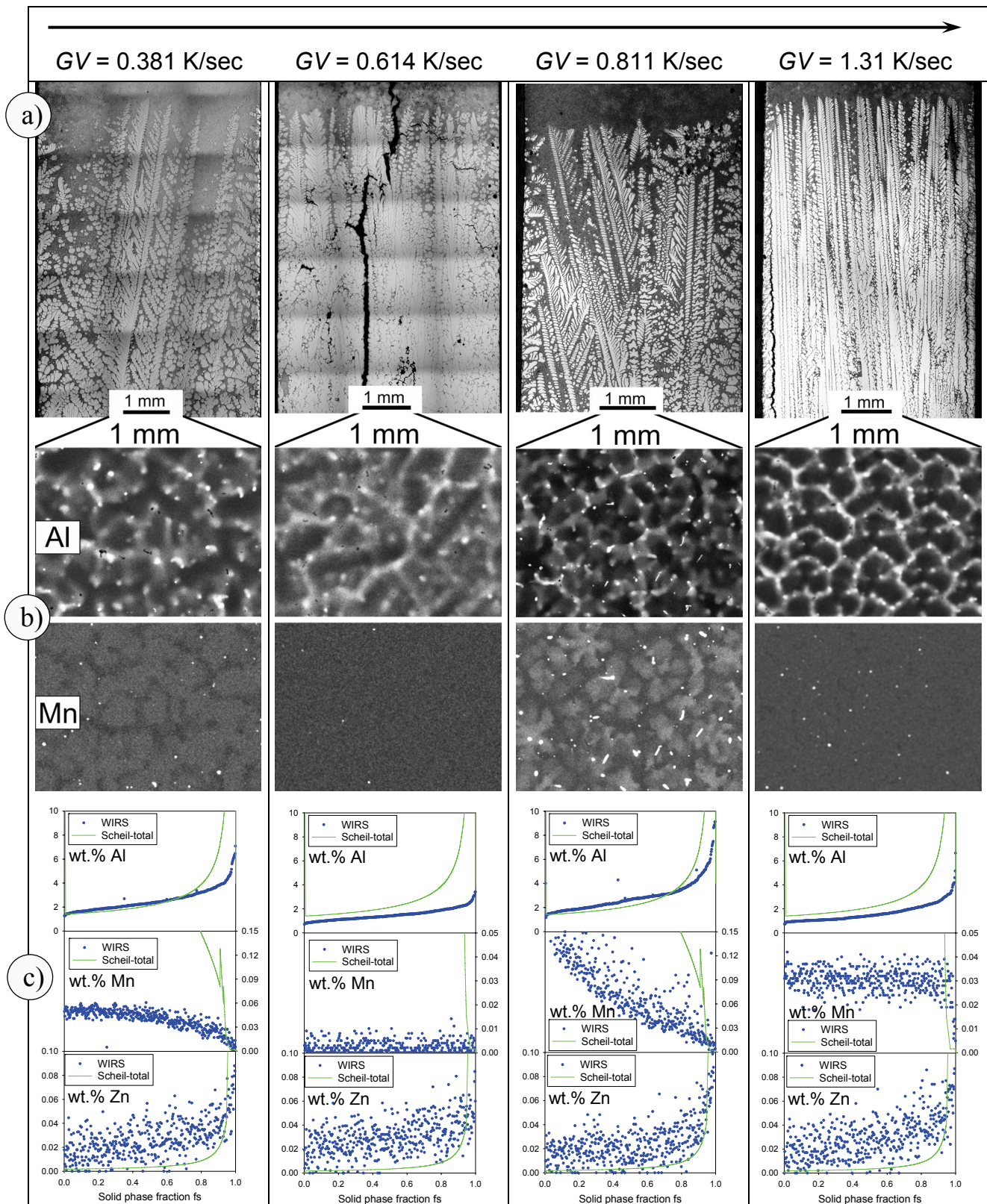


Figure 6.2. AM50 at four cooling rates:  
 a) Quenched mushy zone, LOM of longitudinal section;  
 b) Cross sectional EPMA-WDS compositional maps of Al and Mn;  
 c) Comparison WIRS to Scheil-total solute profiles.



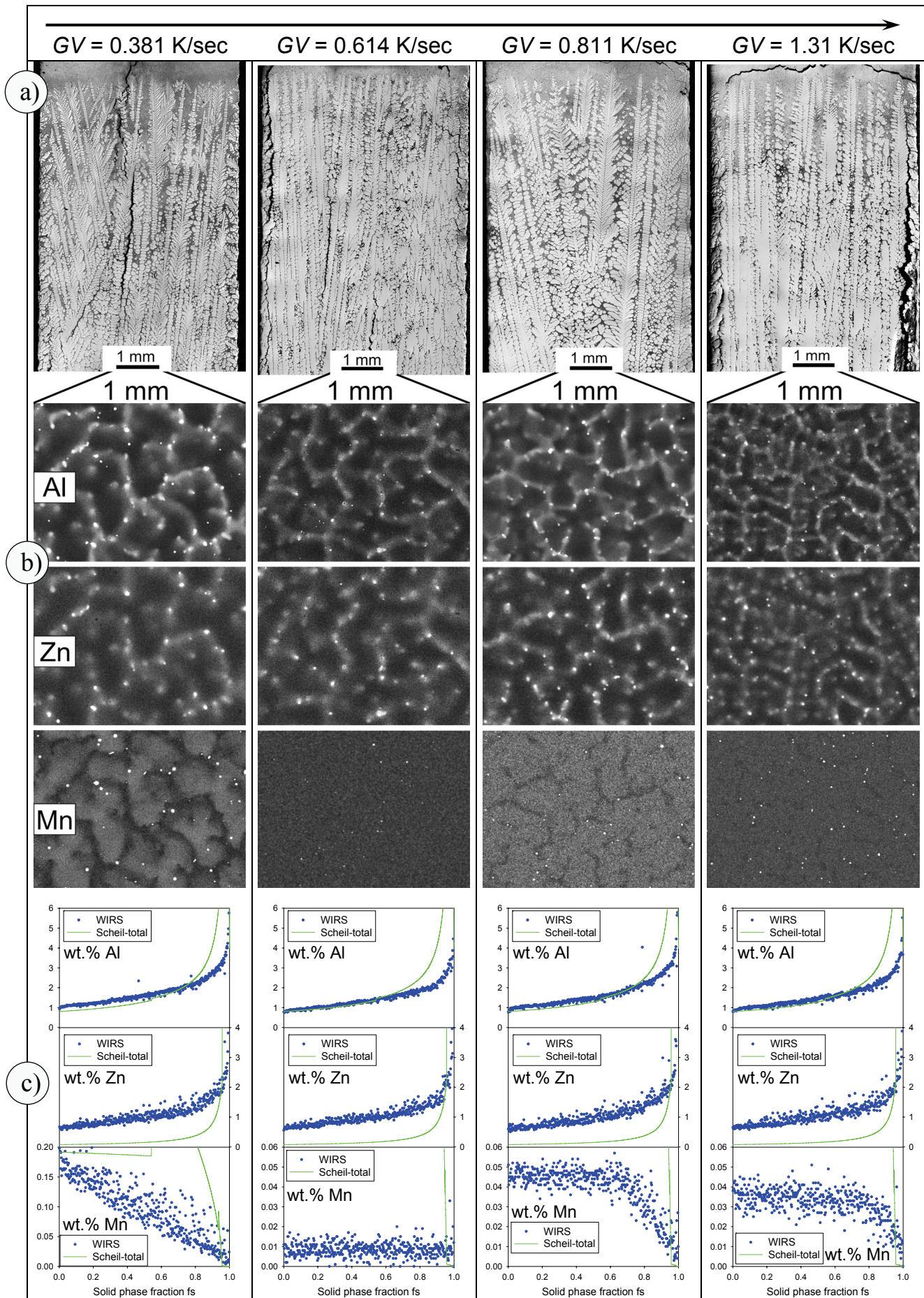


Figure 6.3 AZ31 at four cooling rates: a) Quenched mushy zone, LOM of longitudinal section; b) Cross sectional EPMA-WDS compositional maps of Al, Zn and Mn; c) Comparison WIRS to Scheil-total solute profiles.

The mushy zone cross sections and compositional maps, which are also shown in Figs. 6.2 and 6.3, are used to quantitatively determine average primary dendrite arm spacing  $\lambda_1$  for both alloys. **Fig. 6.4** shows decreasing  $\lambda_1$  with increasing cooling rate  $GV$ , confirming this visual observation. Even if only two solidification rate values per temperature gradient were applied in this work (Tab. 5.2, Chapter 5), the Hunt-Lu model [1996Hun] may be used as an estimation. According to the Hunt-Lu model,  $\lambda_1$  is described as a power law function of the solidification rate  $V$  ( $\lambda_1 \sim V^n$ ). For the temperature gradient  $G = 9.8$  K/mm virtually the same exponent  $n$  was found for both alloys,  $n = -0.41$  for AM50 and  $n = -0.40$  for AZ31. For the higher temperature gradient of  $G = 15.8$  K/mm the values differ somewhat,  $n = -0.66$  for AM50 and  $n = -0.75$  for AZ31. These data may be compared with the value  $n = -0.59$  obtained for a Mg - 4 wt.% Al alloy solidified under  $G = 4$  K/mm over a wider range of cooling rates [2007Zha].

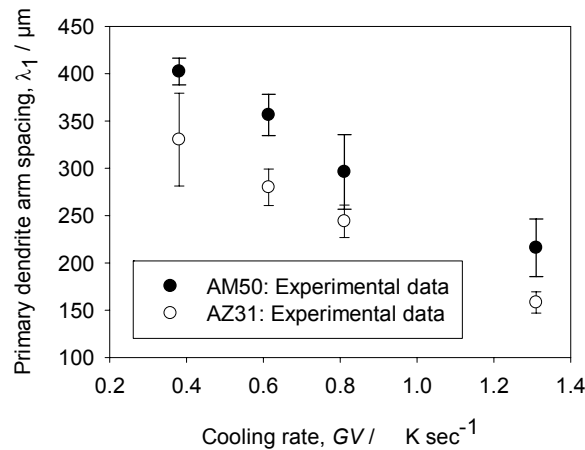


Figure 6.4. The average primary dendrite arm spacing ( $\lambda_1$ ) decreases with cooling rate.

Two main coarsening mechanisms are observed in the dendritic microstructure obtained during directional solidification in this work. The dynamic coarsening [1981Hua] i.e. competitive growth of secondary arms, is dominating within the mushy zone. Here some secondary arms appear stopping growth, while the direct neighbors continue their growth. Approaching the end of the mushy zone, where fraction solid,  $f_s$ , becomes unity, the sintering of neighboring arms becomes the dominating coarsening mechanism. With increasing distance beneath dendrite roots this coarsening mechanism yielded a virtually continuous plane instead of individual arms. Only a severe etching enabled resolving the individual dendrite arms if the distance, measured beneath dendrite roots at  $f_s=1$ , exceeded 50 mm.



### 6.2.3 EPMA-WDS microsegregation data beneath the mushy zone

#### 6.2.3.1 Solute compositional maps

Segregation in the AM50 alloy solidified at  $GV = 0.811$  K/sec is detailed in **Fig. 6.5a** with compositional maps of all components, including the minority component Zn. The scanned area is taken from a cross section beneath the dendrite roots where the sample was completely solidified before quenching. The dendritic microstructure is obvious in this cross section. The gray scale shows the varying contents of the segregated components in the Mg alloy, the brighter areas indicate solute rich regions. It is to be noted here that the contrast was strongly increased in both the Mn and Zn maps in order to reveal the solute concentration gradient in (Mg) dendrite stems. For that reason the observed area fractions of the very bright Zn and Mn containing particles appear overestimated.

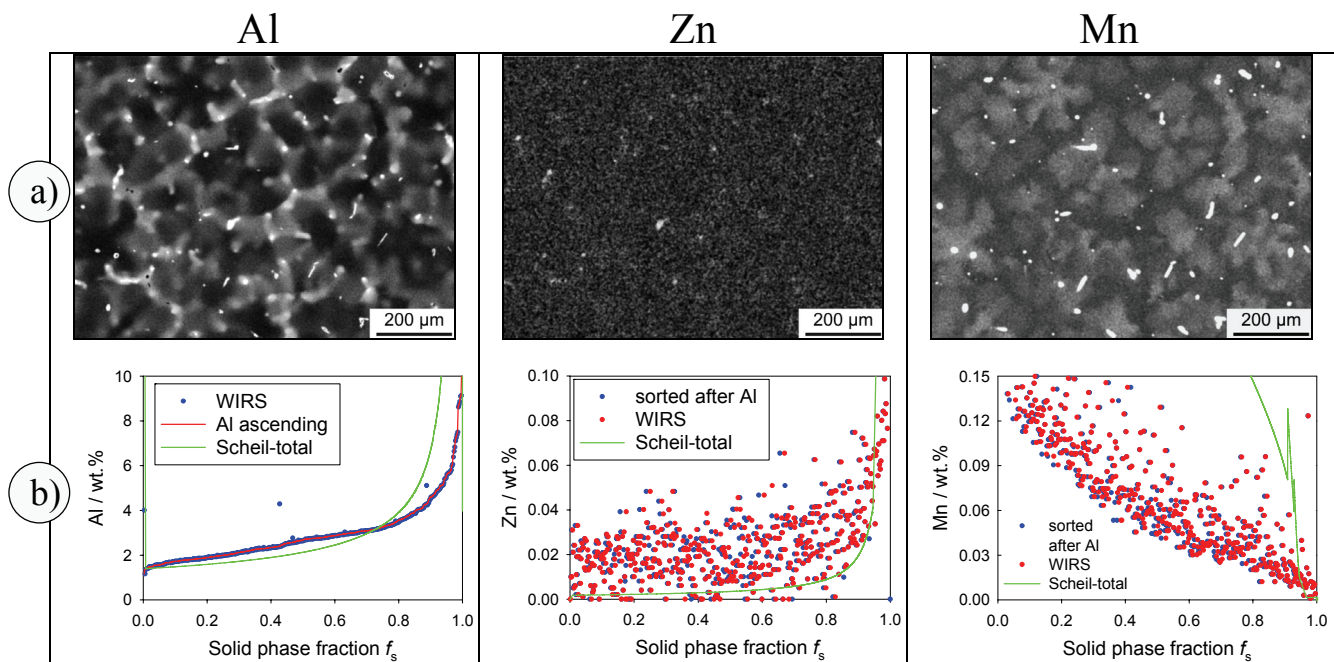


Figure 6.5. AM50 sample solidified at  $GV = 0.811$  K/sec  
 a) Cross sectional qualitative EPMA-WDS compositional maps of Al, Zn and Mn; brighter areas indicate solute rich regions.  
 b) Corresponding quantitative Al, Zn and Mn solute profiles, each determined by three methods.

Aluminum is clearly segregating into interdendritic regions. This is apparently also valid for Zn when viewing the original microscope screen. The manganese shows opposite segregation behavior. The Zn-rich particles are found always in interdendritic regions, typically at the same locations where Al enrichment was observed. The bright particles showing simultaneously Al and Mn enrichment are observed both in the interdendritic regions and also within the dendrite stems. The Al-Mn particles observed within the dendrites

typically emerge in needlelike shape, indicating primary crystallization. The bright Al containing particles found in interdendritic regions are related to the  $\gamma$ -Mg<sub>17</sub>Al<sub>12</sub> phase, as detailed below.

The interdendritic microstructure of this sample is shown magnified in **Fig. 6.6**. The three phases, Al<sub>8</sub>Mn<sub>5</sub>,  $\gamma$ -Mg<sub>17</sub>Al<sub>12</sub> and (Mg) are revealed by the mass contrast in this back scattered electron (BSE) image. The EPMA analysis of these particles provides the following mean phase compositions: Al<sub>8</sub>Mn<sub>5</sub>: Al 62-Mn 38;  $\gamma$ -Mg<sub>17</sub>Al<sub>12</sub>: Mg 67-Al 33 (at.%). The occurrence of these phases is in good agreement with the Scheil calculations detailed later.

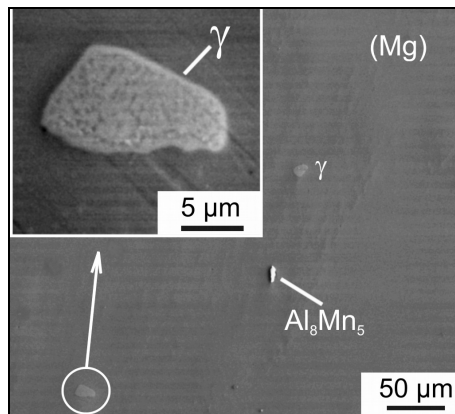


Figure 6.6. Electron microscopic close-up image (BSE contrast) of the interdendritic area from Fig. 6.5a; inset shows a magnified view of the encircled particle. The three phases, Al<sub>8</sub>Mn<sub>5</sub>,  $\gamma$ -Mg<sub>17</sub>Al<sub>12</sub> and matrix (Mg) were observed, also identified by EPMA spot analysis.

The effect of the homogenization during the solidification was also observed on the example of the AZ31 alloy. Transverse EPMA–WDS line scan solute profiles were measured over secondary dendrite arms. For the AZ31 sample solidified at  $GV=1.31$  K/sec two line scans were compared: first, in the next proximity of the dendrite tips, and the second, within the same plane investigated to obtain quantitative EPMA data, which is approximately 70 mm distance to dendrite tips and completely solidified before quenching. The first line scan measured close to the dendrite tips shows significantly sharper peaks when crossing the interdendritic area. Within the (Mg) dendrite itself, virtually constant Al and Zn content were found. The second line scan, measured beneath the mushy zone, shows much smoother Al and Zn profiles. A peak drifting and merging, as reported by [2003Lac], was not observed in this study.

A systematic comparison of compositional maps for all four cooling rates and for both AM50 and AZ31 is shown in Figs. 6.2 and 6.3, respectively. The essentially empty Zn maps

for AM50 are excluded. The solute distribution will be discussed below, jointly with the quantitative solute profiles.

For both alloys no significant impact of the cooling rate  $GV$  on the aluminum distribution during the solidification was observed. The manganese distribution within dendrite stems appears more homogenous for  $GV$  values of 0.614 and 1.31 K/sec. These  $GV$  values imply a higher temperature gradient (15.8 K/mm) obtained by higher furnace temperature of 800°C.

### 6.2.3.2 Quantitative EPMA data and solute profiles

For the same sample as given in Fig. 6.5 (AM50 solidified at  $GV = 0.811$  K/sec) the solute-solvent correlation is shown in **Fig. 6.7**. All the  $21 \cdot 21 = 441$  grid point composition quadruples from the quantitative segregation mapping of a  $1000 \cdot 1000 \mu\text{m}^2$  area are presented here. The opposite segregation behavior of Mn compared to both Al and Zn is obvious in this presentation. Just like in the case of AZ31, this provides a quantitative and unbiased basis for step 1 of the WIRS scheme, the determination of normal and inverse partitioning directions. A virtually scatter-free and almost perfect correlation of descending Al content with ascending Mg content is detected in this AM50 sample. This may be compared with the data of AZ31 in Fig. 5.9, Chapter 5, showing also a clear correlation but significantly more scatter.

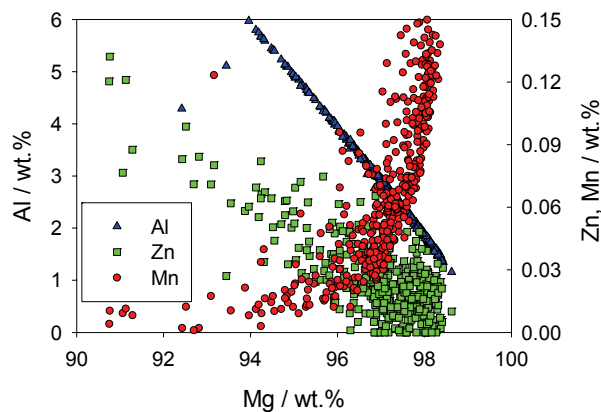


Figure 6.7. Solute-solvent correlation relationship in AM50 after directional solidification at  $GV=0.811$  K/sec, revealing the opposite segregation behavior of Mn compared to both Al and Zn.

The Al, Zn and Mn solute profiles determined by EPMA are compared in **Fig. 6.5b** for the two sorting schemes WIRS and Al-leading-element. Apparently, the differences between these sorting schemes are small, as viewed best in the Al profile; this is of course due to the unusually close Al-Mg correlation shown in Fig. 6.7. However, a most significant difference in the initial stage is emphasized: The Al-leading-element sorting can, by definition, only

produce monotonously ascending Al-content with  $f_S$ , and not the initial decrease produced correctly by the WIRS scheme for this alloy as detailed in Fig. 5.11, Chapter 5. This relates to the primary precipitation of small amounts of Al-Mn intermetallic phase. Therefore, the WIRS scheme is clearly superior to a leading-element sort for both alloys, AM50 and AZ31. In the case of AZ31 it reflects the distribution of experimental scatter over the three solute profiles more realistically than showing a monotonous Al profile and wider scattering Zn and Mn profiles.

The average compositions of Al, Zn and Mn, calculated from all 441 measured points, are given in Tab. 6.1, denoted as “EPMA”; the deviation from the ICP-AES data is assumed to have essentially the same explanation as for AZ31 alloy, which is detailed in the section 5.7.2, Chapter 5. The AM50 alloy compositions denoted as “Before DS” in Tab. 6.1 were used for calculation of the Scheil-total solute profile. These profiles, plotted for comparison in Fig. 6.5b, demonstrate the effect of homogenization during solidification, or back-diffusion, mentioned above. The very steep calculated composition gradients at the high end of  $f_S$  are mitigated in the experimental data, accompanied by a higher level of solute (lower level for Mn) in the medium range in view of the materials balance of the back-diffusing components. The same effect is also observed for the AZ31 alloy.

### 6.2.3.3 Impact of cooling rate ( $GV$ ) on the solute profiles

A systematic comparison of solute profiles for all four cooling rates and for both AM50 and AZ31 is shown in Figs. 6.2 and 6.3, respectively. The effect of homogenization or back-diffusion is observed under all conditions for both alloys by comparing the deviation of the experimental WIRS data to the (cooling rate independent) Scheil-total calculations. The qualitative trends are in agreement, though. An exception is the extremely low Mn content measured in both alloys solidified at  $GV = 0.614$  K/sec; the average EPMA value is only 0.002 (0.009) wt.% Mn compared to initial values of 0.30 (0.20) wt.% Mn before DS in AM50 (AZ31) alloys, respectively. This deviation cannot be explained. A larger deviation, due to average Al-deficit, is also observed for the AM50 alloy in Fig. 6.2 at  $GV = 0.614$  and 1.31 K/sec, the WIRS data being significantly below the Scheil-total profiles. These conditions relate to the higher furnace temperature of 800°C and, thus, an increased Al-loss compared to the initial value of 4.39 wt.% Al. As discussed in Chapter 5, these conditions are stressing the BN protection layer to the limit, even more so for AM50 compared to AZ31. None of these drastic composition changes are observed for the Zn-content, initially 0.97 wt.% in AZ31 and 0.022 wt.% Zn in AM50. This accentuates the finding that Zn is not

---

involved in the detrimental reaction between the (protected) steel tube and Mg alloy, detailed in Chapter 5. Consequently, the Zn solute profiles show a consistent back-diffusion effect compared to Scheil-total at reasonably similar average values for AZ31; the same holds true for AM50, considering the much wider experimental scatter due to the very low total Zn content. It is also noted that back-diffusion is more pronounced for Zn compared to Al for both alloys based on a qualitative judgment of the solute profiles in Figs. 6.2 and 6.3.

A nicer visual agreement for all solute profiles may be obtained if the composition assumed for the Scheil-total calculation is readjusted to the ICP-AES data, or even the average EPMA data, of the corresponding solidification conditions in Tab. 6.1. On the other hand, keeping a fixed initial alloy composition provides a set of independent "benchmark" Scheil-total profiles in Figs. 6.2 and 6.3, respectively. This decision may be reconsidered if a more elaborate quantitative micro-modeling of the microsegregation in these alloys is attempted.

A direct comparison of the WIRS Al solute profiles of AM50 for all four cooling rates (0.381 – 1.31 K/sec) applied in this work shown in **Fig. 6.8**. The sequence of the legend reflects the distinguishable values in the profiles at about  $f_S = 0.9$ . The two upper WIRS curves relate to a lower temperature gradient,  $G = 9.8$  K/min, and lower furnace temperature of 720°C. This is well explained by the larger total Al-loss observed at 800°C pertinent to the two lower curves. Within each group, the sample solidified at higher cooling rate,  $GV$ , builds up a more strongly rising Al-content beyond about  $f_S = 0.7$  to 0.8. This might indicate a lesser back-diffusion, as expected, but is not considered clear enough.

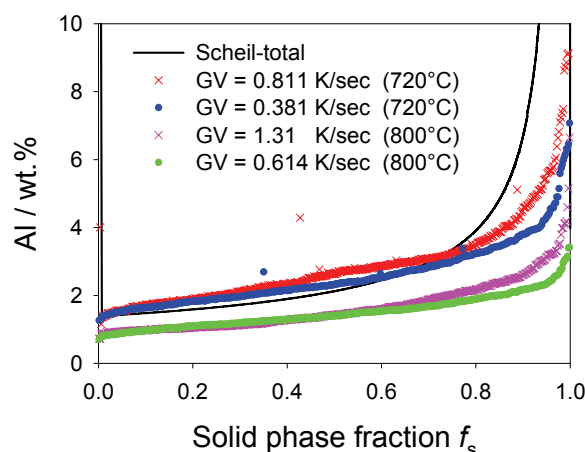


Figure 6.8. The WIRS Al solute profiles of AM50 at four cooling rates; see text.

The same comparison made for the AZ31 alloy does not show a significant dependence on the solidification or cooling rate. The WIRS Al solute profiles essentially overlap within the experimental scatter and are not reproduced here.

### 6.3 Conclusions

Dendritic microstructures and microsegregation data are investigated in a systematic and comparative study of two magnesium alloys, AM50 and AZ31. Results presented in a wallpaper-style combination of microstructures taken from longitudinal sections of the quenched mushy zone, X-ray maps of fully directional solidified cross sections and quantitative WIRS-EPMA solute profiles reveal the impact of cooling rate and alloy type. Primary dendrite arm spacing is significantly higher in AM50 compared to AZ31 under same cooling conditions. The AM50 alloy is more aggressive in attacking the steel tube, even through an optimized boron nitride protective layer, compared to AZ31.

Solute-Solvent correlation relationship in AM50 disclose the opposite segregation behavior of Mn compared to both Al and Zn and provide an impartial basis for the advanced WIRS sorting scheme. Precipitates  $Al_8Mn_5$  and  $\gamma-Mg_{17}Al_{12}$ , predicted by thermodynamic calculations, are identified in the (Mg) solid solution phase. The effect of the homogenization, or back-diffusion, during the solidification was clearly observed for both alloys in comparison with dedicated Scheil-total calculations; it appears most pronounced for the component Zn.

## 7 Summary

The micro-scale solidification of commercial Mg alloys of the AZ and AM series is in the focus of the present thesis. Two approaches of investigating solidification are implemented, complementary regarding temperature gradient and solidification rate, and also with respect to the generated microstructure.

The first approach considers solidification under a negligible spatial temperature gradient. Here the solidification curves, i.e. fraction solid versus temperature, were determined by developing an improved heat-transfer modeling applicable on both differential thermal analysis (DTA) and differential scanning calorimetry (DSC) signals. The correlation between solidification enthalpy and fraction solid during solidification was tested in detail. A better evaluation of the measured DTA and DSC signals is attained through an independent measurement of the time constant as function of temperature for the applied equipment. A further improvement is achieved through a more impartial interpretation of the measured curves. Both improvements enable a better desmearing of measured signals and reduce the error induced by the operator. The novel tantalum encapsulation enabled appropriate handling of challenging Mg-alloys. This special adaptation of the DTA/DSC setup using sealed Ta capsules was indispensable for generation of reproducible and reliable data. The obtained solidification curves are highly reproducible. The results indicate a potential of this method for simple, fast and reliable determination of solidification curves even for Mg alloys, despite their high reactivity and vapor pressure. The viability and limitations of thermal analysis in general to determine start and end of solidification of AZ magnesium alloys was also studied.

The second approach is based on directional solidification in a high temperature gradient and at constant solidification rate, achieved by the Bridgman technique. The resulting dendritic microstructure and inherent microsegregation are studied in this work. The solute profiles, i.e. solute content versus solid phase fraction during solidification, are determined by an advanced treatment of the EPMA data. The key experimental challenge in the Bridgman technique for Mg alloys containing Al is the development of a sufficiently inert sample tube. Problems that are demonstrated in this work are Al-loss and melt pollution due to reaction with typical sample container material made of unprotected steel. This issue was entirely ignored in the few experimental reports in the literature pertinent to this alloy group. As basis for a reliable and reproducible microsegregation study, a new experimental method was developed emphasizing the preservation of the initial alloy composition during solidification. The development of an optimized boron nitride (BN) coating to prevent detrimental reaction between Al and sample container is a successful novelty. The interplay between tube material,

---

---

inside tube coating and details of the Bridgman device was thoroughly investigated. The result enables controlling the reaction on the tube/sample interface. The next novelty is correct implementation of the Scheil model for the solute profile calculation, implying precipitates during multiphase solidification. The combination of the optimized technique for directional solidification, sophisticated WIRS sorting scheme of EPMA data and true Scheil-total solute profile enables a reliable and more quantitative microsegregation study of Mg-alloys containing Al. This approach is proposed as a reliable tool for determination of correct phase sequence during solidification, thus complementing the determination of solid phase fraction by the heat-transfer modeled DSC experiments.

---



## Appendices

### Appendix A The use of Ta-encapsulation at extreme conditions

The DTA and DSC Ta-capsules shown in Fig. 4.1, Chapter 4 entirely meet the requirements set out in this study regarding their reactivity with the studied AM and AZ magnesium alloys within the applied temperature range.

However, these Ta-capsules were also applied for the investigation of other samples. In this case the Ta-capsules appeared not to meet these requirements. Three examples of experiments are given below, which demonstrate limitations in the use of these capsules. A promising solution for treating these challenging cases is proposed.

**Figs. A.1-A.3** depict the cross sectioned contact surfaces between Ta-capsules and pure Al,  $Mg_{10}Mn_{90}$  and  $Al_{39}Bi_{11}Cu_{50}$  (at.%) samples, respectively. In the measurement of these samples by DTA and DSC, the Ta-capsules have been investigated at significantly higher temperatures and, in case of the sample containing Mn also at higher pressures, relative to the conditions prevailing in the normal experimental procedure used in present work.

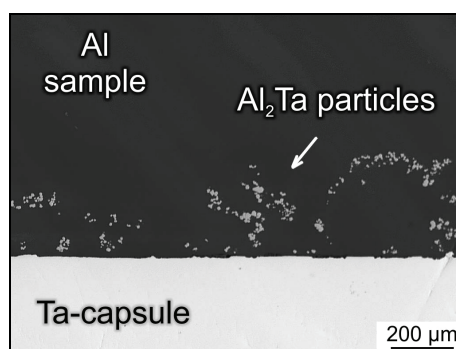


Figure A.1. BSE micrograph of the pure Al sample showing the bottom region of the cross sectioned Ta-crucible after one 100 – 850 – 100°C DTA cycle using a 5 K/min scanning rate and 15 minutes holding time. Particles of  $Al_2Ta$  detach from the Ta-capsule and float into the Al-melt.

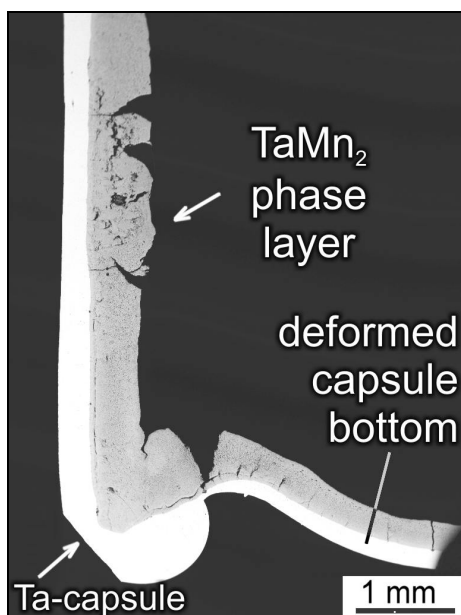


Figure A.2. BSE micrograph of the  $\text{Mg}_{10}\text{Mn}_{90}$  sample showing the bottom region of the cross sectioned Ta-crucible after *three* 600 – 1250 – 600°C DTA cycles using a 5 K/min scanning rate. All Mn is consumed to form a  $\text{TaMn}_2$  phase. This phase forms a layer on the walls of the Ta-crucible. The deformation of the capsule bottom due to the high internal pressure at higher temperatures is also visible.

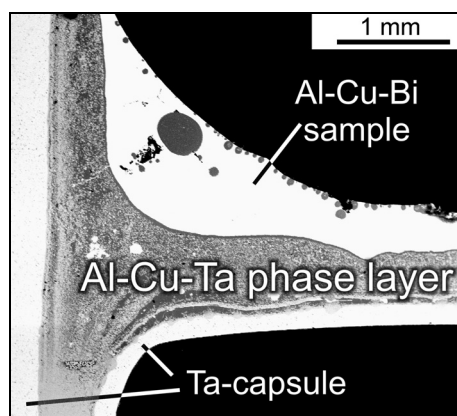


Figure A.3. BSE micrograph of the  $\text{Al}_{39}\text{Bi}_{11}\text{Cu}_{50}$ , at.% sample showing bottom region of the cross sectioned Ta-capsule after *four* 150 – 1200 – 150°C DSC cycles using a 5 K/min scanning rate. The Al-Cu-Ta phase layer was observed.

These BSE micrographs reveal that under such extreme experimental conditions it is not possible to reliably exclude a chemical reaction between the Ta-capsule and the sample. Additionally, in the case that samples are employed characterized by the formation of high vapor pressures, mechanical stress affects integrity and tightness of the capsule. For DTA/DSC measurements of such challenging samples, a boron nitride (BN) inlay for Ta-capsule was developed. It is well-known that BN is chemically inert to most substances and by performing additional experiments it was confirmed that the above mentioned sample did not react with BN.

**Fig. A.4** shows that this inlay realizes a reliable mechanical and chemical barrier between the sample and Ta-capsule.

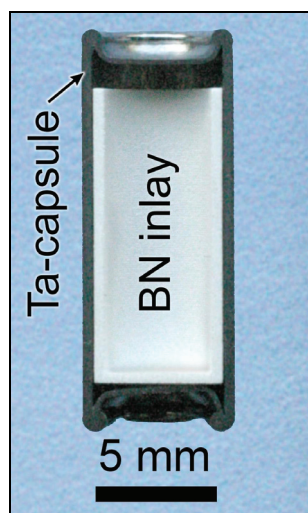


Figure A.4. A Ta capsule with boron nitride (BN) inlay was developed for performing measurements of samples exhibiting strong reactivity with tantalum.

Apart from these advantages, it is obvious that the application of a BN inlay results in a decrease of effective volume and an increased time-constant, which in turn lead to a lower resolution of the measurement. The high thermal conductivity of BN is advantageous, though.

## Appendix B Details of the reaction between steel tube and Mg-Al alloy

This appendix describes four cases of reactions between the sample and tube material. In the first two cases, results of experiments are described in which the contact time between uncoated tube and sample is 19 days at 650°C. The first case is the reaction between a tube composed of St35 steel and a sample composed of an AZ62 Mg-alloy and the second one is the reaction between a V4A steel tube with an AZ91 Mg-alloy. In the third case results are presented of the reaction between a V4A steel tube and an AZ91 alloy sample at the higher temperature of 800°C. Finally, In the last case results are given of the reaction between a St35 steel tube coated with a Type-V BN layer and an AZ31 alloy.

### *Case 1. Uncoated St35 steel tube and AZ62 Mg-alloy brought in contact for 19 days at 650 °C*

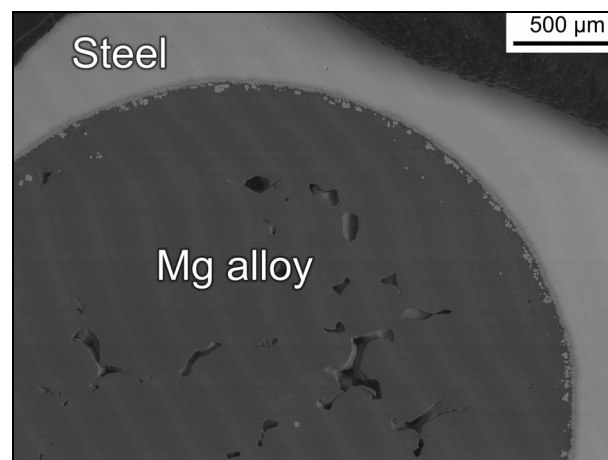


Figure B.1. Contact surface between AZ62 and St35 steel tube (BSE micrograph) after 19 days exposure to the melt at 650°C.

In the section 5.6.1 it was pointed out that after 12 hours of contact between a St35 steel tube and AZ62 Mg-alloy sample at 650°C, an intermetallic layer was formed with a thickness of about 30 μm. In the present research it was found that this layer thickness is not significantly time dependent when the contact time is extended to 19 days.

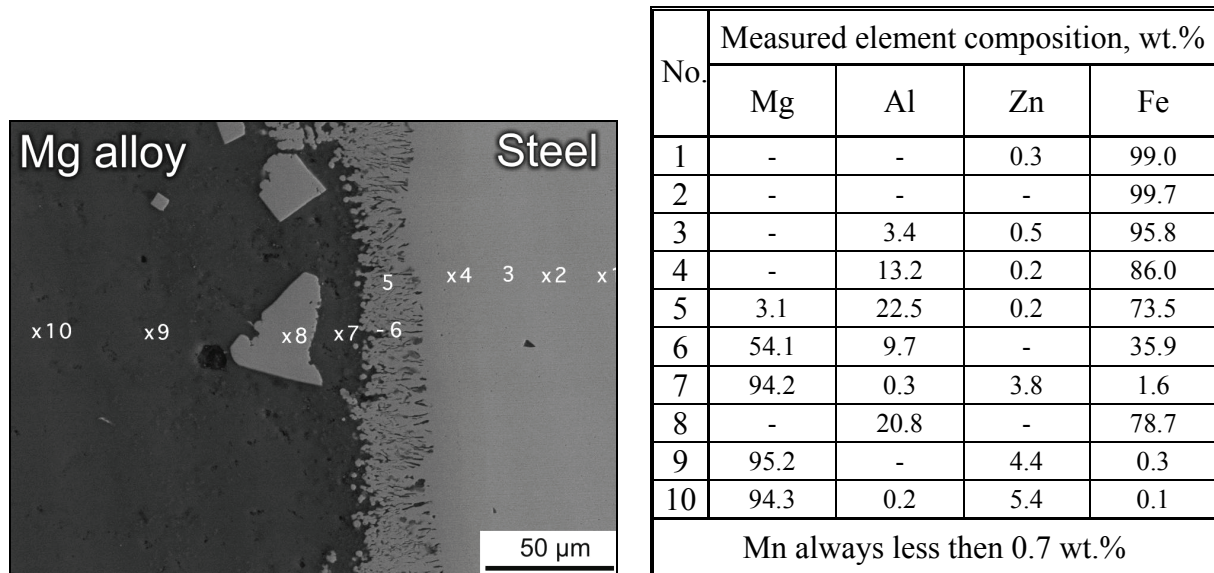


Figure B.2. Magnification of the interface region shown in Fig. B.1. SEM-EDS results indicate the composition of different locations in this region.

However, a salient feature occurred in this period of time. In the micrograph shown in **Fig. B.2** evidence was found of the formation of 30 µm large blocky particles. SEM/EDS analysis showed that these particles have an average composition of Fe<sub>65</sub>Al<sub>35</sub> (at.%). Fig. B.2 is a magnification of **Fig. B.1** showing that these particles detach from the intermetallic phase covering the tube wall and float in the Mg-melt.

### ***Case 2. Uncoated V4A steel tube and AZ91 Mg-alloy brought in contact for 19 days at 650 °C***

The alternative tube material, composed of V4A steel, was also tested for 19 days at 650°C. This tube was brought into contact with a melt formed from an AZ91 alloy. The investigation of the interface between tube and sample showed a similar behavior as the St35 steel tube in contact with the AZ62 Mg-ally sample.

Just as for the St35 steel tube a coherent Mn-free intermetallic layer and blocky particles floating in the melt were found in the diffusion zone. **Fig. B.3** and the magnification shown in **Fig. B.4** demonstrate that the formation of these blocky particles is less pronounced than is the case for St35 steel tube. Another difference is that not only Al and Fe are present in the intermetallic layer, but also Cr and Ni, 6 wt.% and 5 wt.% respectively. These elements stem from the stainless V4A steel.

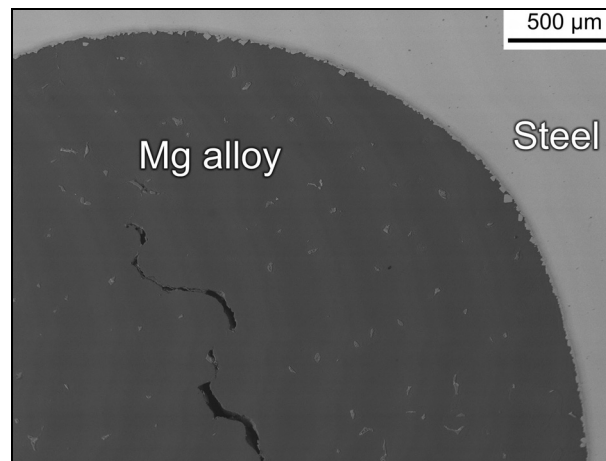


Figure B.3. Contact surface between AZ91 and V4A steel tube (BSE micrograph) after 19 days exposure to the melt at 650°C.

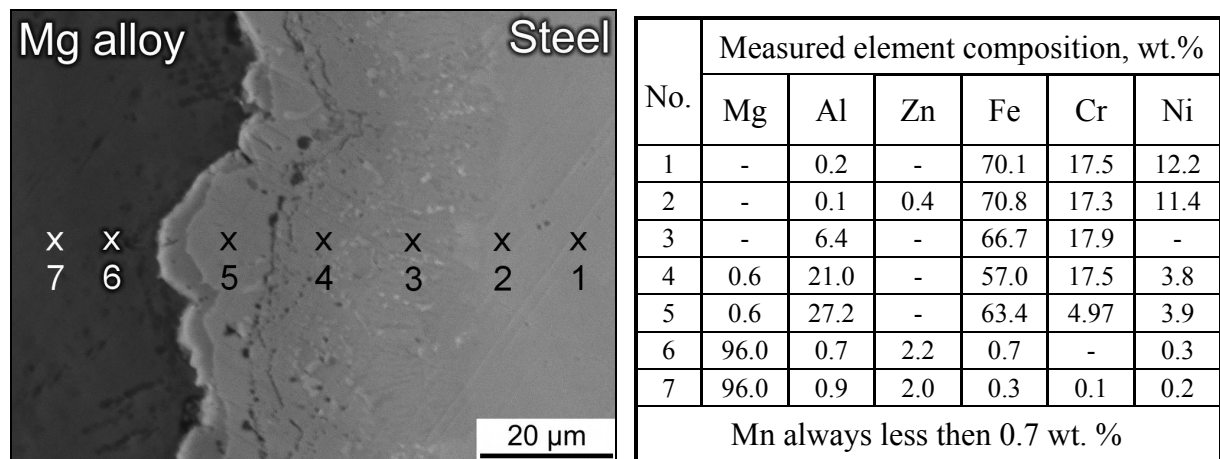


Figure B.4. Magnification of the interface region shown in Fig. B.3. SEM-EDS results indicate the composition of different locations in this region.

All these reactions shown in these two cases are significant and they occur even though 650°C is well below the temperature necessary for the actual directional solidification.

**Case 3. Uncoated V4A steel tube and AZ91 Mg-alloy brought in contact for 2 hours at 800 °C**

Preliminary experiments were carried out comprising direct solidification of an AZ91 alloy within the V4A steel tube at 800°C during a contact time of 2 hours.

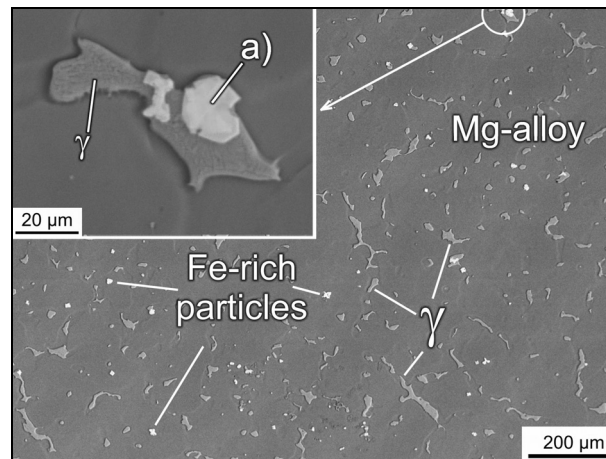


Figure B.5. The cross sectioned V4A steel tube with directionally solidified AZ91 alloy; The tube spent about 2 hours in contact with the melt heated at 800°C; The shown site is located approximately 1mm away from the inner tube surface; The bright Fe-rich particles are clearly recognisable in the microstructure; These particles are often observed within the  $\gamma$ -phase particles; SEM-EDS measurement of the site marked by a) shows that the particle has a 49Fe-29Al-11Mn-7Cr-3Ni-1Mg (wt.%) composition; Particles containing up to 16 wt.% Ni besides Fe and Mn are also found in the microstructure; Both the elements Fe and Ni originate from steel tube.

It is evident from **Fig. B.5** that Fe and Ni are transferred from the tube into the melt region. Similar to the case 2, the intermetallic layer, which is forming between the tube and sample (not shown here) is mainly composed of Fe and Al, with significant amounts of Cr and Ni. A difference with the two former cases is the observation of a significant amount of 7 wt.% of manganese in this intermetallic layer. Fig. B.5 shows that large intermetallic particles detached from this layer into the melt. These particles were observed at a considerable distance of 1 mm away from the inner tube surface. A salient feature is that these particles are often observed within the  $\gamma$ -phase particles as shown in the inset of Fig. B.5.

**Case 4. Type-V BN coated St35 steel tube and AZ31 alloy brought in contact for 1 hour at 720 °C**

The last case discussed here is the reaction between a St35 steel tube coated with a BN layer and an AZ31 alloy. Figure 6 demonstrates that occasionally deep intrusions of Mg-melt in the BN coating are observed when the coating was not polished. A possible reason for this is that an unpolished coating has a larger wettability by the Mg-melt relative to a polished coating. Therefore the unpolished coating has less protection ability.

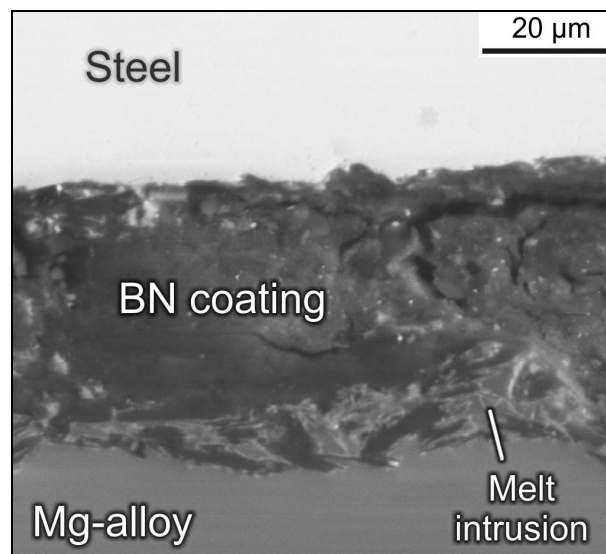


Figure B.6. Contact surface between AZ31 and St35 steel tube (BSE micrograph) after about 1-hour exposure to the melt at 720°C; The BN coating was not polished before the tube was filled with the Mg-alloy; The coating is in some places damaged by melt intrusions.

This Figure can be compared to Fig. 5.4 in Chapter 5, because in both cases the same parameters for directional solidification were applied and a similar alloy was studied. The only difference is the preparation of the BN coating, because the coating shown in Fig. 5.4 was carefully polished before the tube was filled with the Mg-alloy.



## Appendix C DSC response to the varying Zn content in Mg-Al-Zn alloys

### *Introduction and procedure*

Description of solidification path for the Mg rich corner of the Mg–Al–Zn alloys using the DTA/DSC experimental techniques is presented in this appendix. A particular attention is directed to the composition range, 0-10 wt.% Al and 0-3 wt.% Zn, which is quite important from the point of view of industrial applicability of Mg-alloys. Since highly precise analysis on the phase equilibria in this composition range has previously not been carefully performed applying current sophisticated equipment, it has been carried out own key experiments using DTA/DSC measurements with Ta crucible [2006Ohn3]. Two samples with varying Zn contents were investigated (**Tab. C.1**).

Table C.1. Chemical composition of the investigated alloys, balance Mg (wt.%).

The compositions of the major elements of our concern, i.e., Al and Zn are denoted in bold letters.

Alloy sample	<b>Al</b>	<b>Zn</b>	Mn	Si	Fe	Cu	Ni	Be
Mg–Al6–Zn1	<b>6.24</b>	<b>0.50</b>	0.0190	0.017	0.0213	0.0019	0.0005	<0.0001
Mg–Al6–Zn2	<b>5.61</b>	<b>1.70</b>	0.011	0.013	0.0229	0.0012	0.0004	<0.0001

The experimental procedures for DTA and both DSC measurements are thoroughly described in section 2.3.1 for DTA, the section 3.2.1 for the DSC 1 and section 3.3.3 for DSC 2.

### *Results and discussion*

**Tab. C.2** summarized the experimental results of the DTA/DSC measurements. Two signals A and B were clearly observed in both, Mg-Al6-Zn1 and Mg-Al6-Zn2 investigated alloys (**Fig. C.1a**). The signal A represents the beginning of the primary equilibrium solidification  $L \rightarrow (Mg)$ , while signal B corresponds to the precipitation of  $\gamma\text{-Mg}_{17}\text{Al}_{12}$  phase. The

temperature for the signal A, which corresponds to the liquidus, was evaluated based on the onset of the signal on cooling curve.

Table C.2. Evaluated signal temperatures of the three alloy samples by means of the DTA and two independent DSC measurements in °C.

	Mg–Al6–Zn1		Mg–Al6–Zn2		
	signal A <sup>(a)</sup>	signal B <sup>(b)</sup>	signal A <sup>(a)</sup>	signal B <sup>(b)</sup>	signal C <sup>(c)</sup>
DSC 1 <sup>(d)</sup> [this work]	611	433	613	415	361
DSC 2 <sup>(e)</sup> [this work]	/		606	411	360
DTA this work	/		608	415	not certain

(a) – start of the (Mg) precipitation

(b) – start of the  $\gamma$  phase precipitation

(c) – start of the  $\phi$  phase precipitation (weak signal)

(d) – evaluation from multiple samples and scanning rates.

(e) – DSC 2 is the experimental data measured with different equipment at Ferro's group (section 3.3.3)

On the other hand, the temperature for the signal B was evaluated based on the maximum of another signal on heating curve. This point will be discussed later in this appendix. In addition to strong signals A and B, a weak signal C was observed at lower temperature in the DSC measurements of Mg–Al6–Zn2 alloy. The temperature for the signal C was evaluated based on both the onset temperatures on the cooling and the maximum temperature on heating curves. It is noted that according to the device performance and the experimental conditions such as cooling/heating rate, the results of DSC1 are considered to be most reliable.

Fig. C.1a shows complete DSC signals (heating/cooling) for both alloys. It has been already mentioned that beside two signals A and B, the signal C was observed in the magnified DSC measurements for Mg–Al6–Zn2 alloy (**Fig. C.1b**). The DSC curve of Mg–Al6–Zn2 alloy in the vicinity of signal C is represented by blue line in Fig. C.1b.

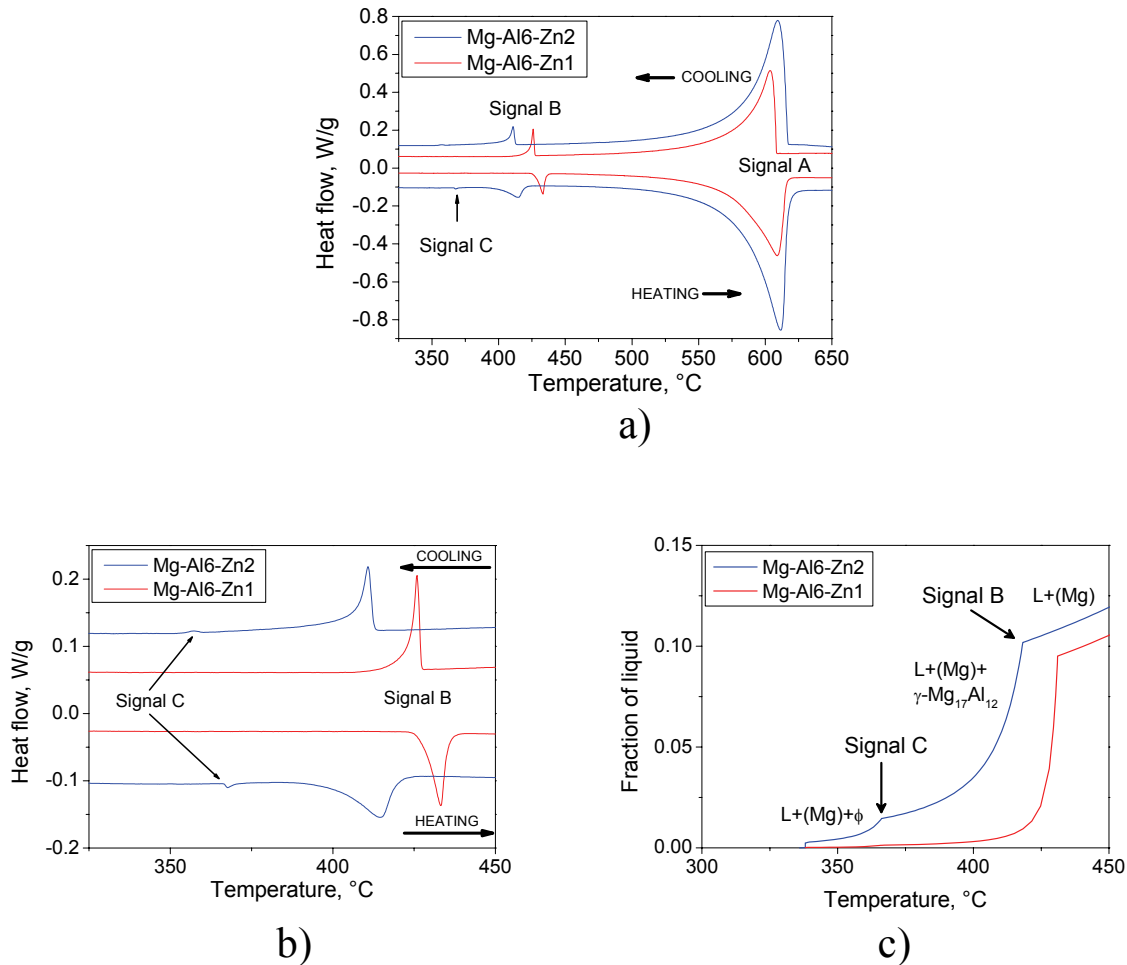


Figure C.1. a) DSC curves of alloys Mg–Al6–Zn2 (blue lines) and Mg–Al6–Zn1 (red lines);  
 b) Magnified signal B and the vicinity of signal C;  
 c) Solidification behavior of alloys Mg–Al6–Zn2 (blue line) and Mg–Al6–Zn1 (red line) calculated by Scheil scheme [2006Ohn3].

For the sake of comparison, also, the DSC curve of Mg–Al6–Zn1 alloy, in which signal C was clearly absent, is indicated by red line in Fig. C.1b. One sees that there exists the small though distinct peak of signal C on both the heating and cooling curves for Mg–Al6–Zn2 alloy. **Fig. C.1c** demonstrates the solidification curves of Mg–Al6–Zn2 alloy (blue line) and Mg–Al6–Zn1 (red line) calculated by Scheil scheme. In the calculated solidification curve of Mg–Al6–Zn2 alloys (blue line), the precipitation of  $\gamma$ -Mg<sub>17</sub>Al<sub>12</sub> phase takes place at 418°C and, furthermore, the ternary intermetallic compound,  $\phi$  phase, starts to precipitate at 366°C. From the comparison between the DSC curve and the sharp bend in the Scheil calculated curve, one can grasp that the signal C is closely related to the precipitation of  $\phi$ -phase. The precipitation of  $\phi$  phase starts at the invariant reaction temperature,

$L + \gamma\text{-Mg}_{17}\text{Al}_{12} \leftrightarrow (\text{Mg}) + \phi$ , 366 °C. More precisely, since this reaction requires the dissolution of  $\gamma\text{-Mg}_{17}\text{Al}_{12}$  phase, this four-phase reaction type cannot be realized under Scheil condition and the precipitation of  $\phi$  phase virtually starts just below this invariant reaction temperature. It should be pointed out that in the case of Mg–Al6–Zn1 alloy also, the precipitation of  $\phi$  phase occurs during the calculated solidification process (red line in Fig. C.1c). However, this is not visible in the solidification curve because of very small amount of  $\phi$ -precipitate and this is quite consistent with the fact that the signal C was not detected in Mg–Al6–Zn1 alloy (red line in Fig. C.1b). The Scheil calculation also showed that very small amount of  $\phi$  phase precipitates in the case of Mg–Al9–Zn1 alloy. It should be noted that even the signal C does not represent the end of solidification and solidification process finishes at lower temperature.

The present research has experimentally established the solidification path of Mg-rich corner of the Mg–Al–Zn alloys by means of DTA/DSC measurements. The following most important results are highlighted.

- (i) Even though the very slow cooling rate in thermal analysis (2 K/min) has been used, the solidification path is far from equilibrium condition and is close to Scheil condition. There is virtually no difference between the results measured with cooling rates of 1 K/min and those results obtained by measuring with even higher cooling rate up to 30 K/min [2006Ohn3].
  - (ii) The low temperature signal B observed in thermal analysis and often claimed as "solidus" is not the equilibrium solidus temperature and is not even the end of non-equilibrium solidification process. This signal corresponds to the *start* of the monovariant eutectic reaction,  $L \rightarrow (\text{Mg}) + \gamma\text{-Mg}_{17}\text{Al}_{12}$ .
  - iii) The lowest signal C observed in the DSC measurement of Mg–Al6–Zn2 alloy represents the precipitation of  $\phi$  phase. It is consistent that this signal was not observed in the Mg–Al6–Zn1 alloy, because the Scheil calculation shows that the precipitation of  $\phi$  phase occurs in that alloys in minute amounts only; the solidification process finishes at even lower temperature.
-

## References

- [1942Sch] E. Scheil, *Bemerkungen zur Schichtkristallbildung*, Z. Metallkd. 34 (1942) 70-72.
- [1968Gra] A.P. Gray, *A Simple Generalized Theory for the Analysis of Dynamic Thermal Measurement*, in Analytical Calorimetry, R.S. Porter and J. F. Johnson, eds., Plenum Press, New York (1968) 209-218.
- [1970Fle] M.C. Flemings, D.R. Poirer, R.V. Barone, H.D. Brody, Microsegregation in iron-base alloys, J. Iron Steel Int., 208 (1970) 371-381.
- [1970Wie] H.G. Wiedemann, A. van Tets, *Thermoanalytical investigations on melting and freezing processes. Calorimetric calibration of DTA apparatus with metal standards*, Thermochim. Acta, 1 (1970) 159-172.
- [1971Lan] Landolt-Boernstein: *Eigenschaften der Materie in ihren Aggregatzuständen*, 1. Teil, Mechanisch-thermische Zustandsgrößen, eds. K. Schaefer, G. Beggerow, Springer-Verlag, Berlin (1971) p. 423.
- [1979Fre] H. Fredriksson, B. Rogberg, *Thermal analysis for interpretation of solidification cycle*, Met. Sci., 3 (1979) 685-690.
- [1981Hua] S.-C. Huang, M.E. Glicksman, *Fundamentals of dendritic solidification. I - Steady-state tip growth. II - Development of sidebranch structure*, Acta Metallurgica. 29 (1981) 701-715, 717-734.
- [1983Sch] K.H. Schönborn, *On the Time Lag between Thermal Event and Measuring Signal in a heat Flux Calorimeter*, Thermochim. Acta, 69 (1983) 103-114.
- [1984Che] I.G. Chen, D.M. Stefanescu, Computer-aided differential thermal analysis of spheroidal and compacted graphite cast irons, AFS Trans., 92 (1984) 947-963.
- [1985Loe] K.R. Loeblich, *A theoretical contribution to the analysis of DTA-peaks of rapid reactions*, Thermochim. Acta, 83 (1985) 99-106.
- [1986Bac] L. Bäckerud, E. Krol, J. Tamminen: *Solidification Characteristics of Aluminium Alloys*, vol. 1: Wrought Alloys, Skanaluminium, Oslo (1986) 65-70.
- [1988Mat] S. Mathisen, Doctoral Thesis, NTH, Trondheim, Norway, 1988.
- [1988Tam] J. Tamminen, *Thermal analysis for investigation of solidification mechanisms in metals and alloy*: Ph.D. Thesis, University of Stockholm, Stockholm (1988) 3-34.
- [1989Gun] M.N. Gungor, *A statistically significant experimental technique for investigating microsegregation in cast alloys*, Metall. Mater. Trans. A, 2011 (1989) 2529-2533.
- [1989Hem] W. Hemminger, H. Cammenga, *Methoden der thermischen Analyse*, Springer-Verlag, Berlin, Heidelberg (1989) 140-164.
- [1989Pet] K. Pettersen; N. Ryum, *Crystallography of Directionally Solidified Magnesium Alloy AZ91*, Metall. Trans. A, 20A (1989) 847-852.
- [1990Pet] K. Pettersen, O. Lohne, N. Ryum, *Dendritic Solidification of Magnesium Alloy AZ91*, Metall. Trans. A, 21A (1990) 221-230.
- [1991Hem] W.F. Hemminger, S.M. Sarge, *The baseline construction and its influence on the measurement of heat with differential scanning calorimeters*, J. Therm. Anal., 37 (1991) 1455-1477.
- [1993Fra] E. Fras, W. Kapturkiewicz, A. Burbielkoa, H.F. Lopez, A new concept in thermal analysis of castings, AFS Trans., 101 (1993) 505-511.
- [1993Ulbr] U. Ulbrich, H.K. Cammenga, *Kopplung kalorimetrischer mit optischen Methoden und deren Anwendung zur Entschmierung von DSC-Kurven* Thermochim. Acta, 229 (1993) 53-67.
- [1994Kiu] M. Kiuchi, S. Sigiyama, *A new method to detect solid fractions of mushy/semi-solid metals and alloys*, Annals of the CIRP, 43(1) (1994) 271-274.
- [1994Loe] K.R. Loeblich, *On the characteristics of the signal curves of heat flux calorimeters in studies of reaction kinetics. Part I. A contribution to the desmearing technique*, Thermochim. Acta, 231 (1994) 7-20.
- [1995Che1] S.W. Chen, C.C. Huang, J.C. Lin, *The Relationship between the Peak Shape of a DTA Curve and the Shape of a Phase Diagram*, Chem. Eng. Sci., 50(3), (1995) 417-431.
- [1995Ban] D.K. Banerjee, W.J. Boettinger, R.J. Schafer M.E. Williams, *Modeling of Heat Flow During Solidification and Melting in a Differential Thermal Analyzer (DTA)*, in Modelling of Casting, Welding and Advanced Solidification Processes VII, M. Cross and J. Campbell, eds., TMS, Warrendale (1995) 491-498.
- [1995Jen] S.C. Jeng, S.W. Chen, C.C. Huang, *Determination of the Solidification Curve of the 7075 Aluminium Alloy by using DTA and Mathematical Modelling*: in Light Weight Alloys for Aerospace Applications III, E.W. Lee, N.J. Kim, K.V. Jata and W.E. Frazier, eds., TMS, Warrendale, (1995) 219-226.
- [1996Jen] S.C. Jeng, S.W. Chen, *Determination of the solidification characteristics of the A356.2 aluminum alloy*, Mater. Sci. Forum 217 (1996) 283-288.
- [1996Che1] S.W. Chen, C.C. Huang, *Solidification Curves of AL-Cu, Al-Mg and Al-Cu-Mg Alloys*, Acta

- Mater., 44(5) (1996) 1955-1965.
- [1996Che2] S.W. Chen, S.C. Jeng, *Determination of the Solidification Curves of Commercial Aluminum Alloys*, Metall. Trans. A, 27A (1996) 2722-2726.
- [1996Hoe] G.W.H. Höhne, W. Hemminger, H.-J. Flammersheim, *Differential scanning calorimetry: an introduction for practitioners*, Springer-Verlag, Berlin, Heidelberg, 1996.
- [1996Hun] J.D. Hunt, S.-Z. Lu, *Numerical Modeling of Cellular/Dendritic Array Growth: Spacing and Structure Predictions*, Metall. Mater. Trans. A, 27A (1996) 611-623.
- [1997Che] S.W. Chen, S.C. Jeng, *Determination of the Solidification Curve of a RENE N4 Superalloy*, Metall. Trans. A, 28A (1997) 503-504.
- [1997Kra] T. Kraft, Y.A. Chang, *Predicting microstructure and microsegregation in multicomponent alloys*, JOM, 49, 12 (1997) 20-47.
- [1997Kra1] T. Kraft, M. Rettenmayr, H. E. Exner, *Modeling of dendritic solidification for optimizing casting and microstructure parameters*, Prog. Mater. Sci., 42, 1-4 (1997) 277-286.
- [1997Sai] K. Saito, K. Takeda, T. Tsukeda, S. Matsuki, : JSW Technical Review 17 (1997) 21.
- [1998Che] S.W. Chen, C.C. Lin, C.M. Chen, *Determination of the melting and solidification characteristics of solders using differential scanning calorimetry*, Metall. Trans. A, 29A (1998) 1965-1972.
- [1998Kur] W. Kurz, D.J. Fisher, *Fundamentals of Solidification*, 4th ed., Trans. Tech. Publ., Aedermannsdorf, 1998.
- [1999Mat] R.H. Mathiesen, L. Arnberg, F. Mo, T. Weitkamp, A. Snigirev, *Time Resolved X-Ray Imaging of Dendritic Growth in Binary Alloys*, Phys. Rev. Lett., 83(4) (1999) 5062-5065.
- [1998Sau] N. Saunders: in *COST507 - Thermochemical Database for Light Metal Alloys*, I. Ansara, A.T. Dinsdale and M.H. Rand, eds., European Communities, Luxembourg (1998) 28-33.
- [2000Boe] W.J. Boettinger, S.R. Coriell, A.L. Greer, A. Karma, W. Kurz, M. Rappaz, R. Trivedi, *Solidification microstructures: recent developments, future directions*, Acta Mater, 48, 1 (2000) 43-70.
- [2000Sar] S.M. Sarge, G.W.H. Höhne, H.K. Cammenga, W. Eysel, E. Gmelin, *Temperature, heat and heat flow rate calibration of scanning calorimeters in the cooling mode*, Thermochim. Acta, 361 (2000) 1-20.
- [2001Che] S.L. Chen, S. Daniel, F. Zhang, Y.A. Chang, W.A. Oates, R. Schmid-Fetzer, *On the Calculation of Multicomponent Stable Phase Diagrams*, J. Phase Equilib., 22 (2001) 373-378.
- [2001Don] H.B. Dong, J.D. Hunt, *A Numerical Model of a Two-pan Heat Flux DSC*, J. Therm. Anal. Calorim., 64 (2001) 167-176.
- [2001Don1] H.B. Dong, J.D. Hunt, *A Novel Single-pan Scanning Calorimeter. Measurement of thermophysical properties of metallic alloys*, J. Therm. Anal. Calorim., 64 (2001) 341-350.
- [2001Sch] R. Schmid-Fetzer, J. Gröbner, *Focused Development of Magnesium Alloys using the Calphad Approach*, Adv. Eng. Mater., 3(12) (2001) 947-961.
- [2002Agr] J. Ågren, F. H. Hayes, L. Höglund, U.R. Kattner, B. Legendre, R. Schmid Fetzer, *Applications of Computational Thermodynamics*, Z. Metallkd. 93, (2002) 128-142.
- [2002Boe] W.J. Boettinger, U.R. Kattner, *On differential thermal analyzer curves for the melting and freezing of alloys*, Metall. Mater. Trans. A, 33A (2002) 1779-1794.
- [2002Che] S.-L. Chen, S. Daniel, F. Zhang, Y. A. Chang, X.-Y. Yan, F.-Y. Xie, R. Schmid-Fetzer, W. A. Oates, *The Pandat Software Package and its Applications*, Calphad, 26 (2002) 175-188.
- [2002Lin] A. Lindemann, J. Schmidt, M. Todte, T. Zeuner, *Thermal analytical investigations of the magnesium alloys AM60 and AZ91 including the melting range*, Thermochim. Acta, 382 (2002) 269-275.
- [2002Mat] R.H. Mathiesen, L. Arnberg, K. Ramsoskar, T. Weitkamp, C. Rau, A. Snigirev, *Time-resolved X-ray imaging of aluminum alloy solidification processes*, Metall. Mater. Trans. B, 33(4) (2002) 613-623.
- [2002Sha] S. Shankar, D. Apelian, *Die soldering: Mechanism of the interface reaction between molten aluminum alloy and tool steel*, Metall. Mater. Trans. B, 33, 3 (2002) 465-476
- [2002Sha1] S. Shankar, D. Apelian, *Mechanism and preventive measures for die soldering during Al casting in a ferrous mold*, JOM, 54, 8 (2002) 47-54.
- [2003Don] H.B. Dong, M.R.M. Shin, E.C. Kurum, H. Cama, J.D. Hunt, *A Study of Microsegregation in Al-Cu Using a Novel Single-Pan Scanning Calorimeter*, Metall. Mater. Trans. A, 34A (2003) 441-447.
- [2003Don1] H.B. Dong, M.R.M. Shin, E.C. Kurum, H. Cama, J.D. Hunt, *Determination of liquid fraction during solidification of aluminium alloys using a single-pan scanning calorimeter*, Fluid Phase Equilib., 212(1) (2003) 199-208.
- [2003Fra] W. Fragner, H. Kaufmann, R. Potzinger, *Magnesium New Rheocasting as an Industrial Process: An Update of Recent Developments*, in Magnesium Alloys and Their Applications VI, K. Kainer, ed., Wiley-VCH, Weinheim (2003) 688-693.
- [2003Loh] A. Lohmüller, M. Scharrer, R. Jennings, M. Hilbinger, M. Hartmann, R.F. Singer, *Injection Molding of Magnesium Alloys*, in Magnesium Alloys and Their Applications VI, K. Kainer, ed.,

- Wiley-VCH, Weinheim (2003) 738-743.
- [2003Mir] D. Mirković, J. Gröbner, R. Schmid-Fetzer, *Solidification Curves of AZ-Magnesium Alloys determined by DSC Experiments and Heat-transfer Model (DSC-HTM)*, in *Magnesium Alloys and Their Applications VI*, K. Kainer, ed., Wiley-VCH, Weinheim (2003) 842-847.
- [2003Rid] Y.W. Riddle, M.M. Makhlof, *Characterizing solidification by non-equilibrium thermal analysis*, in *Magnesium Technology 2003*, H.I. Kaplan, ed., TMS, San Diego (2003) 101-106.
- [2003Han] Q. Han, S. Viswanathan, *Analysis of the Mechanism of Die Soldering in Aluminum Die Casting*, *Metall. Mater. Trans. A*, 34A (2003) 139-146.
- [2003Lac] J. Lacaze, P. Benigni, A. Howe, *Some issues concerning experiments and models for alloy microsegregation*, *Adv. Eng. Mater.* 5, 1-2 (2003) 37-46.
- [2003Lar] D. Larouche, C. Laroche, M. Bouchard, *Analysis of differential scanning calorimetric measurements performed on a binary aluminium alloy*, *Acta mater.*, 51 (2003) 2161-2170.
- [2003Tan] C. Tang, M. Jahedi, M. Brandt, *Role of manganese in the soldering reaction in magnesium high pressure die casting*, *Adv. Eng. Mater.* 5 (12) (2003) 903-906.
- [2003Xie] F.Y. Xie, X.Y. Yan, L. Ding, F. Zhang, S.L. Chen, M.G. Chu, Y.A. Chang, *A study of microstructure and microsegregation of aluminum 7050 alloy*, *Mater. Sci. Eng. A*, 355 (2003) 144-153.
- [2004Bak] S.I. Bakhtiyarov, R.A. Overfelt, S.G. Teodorescu, *Fraction Solid Measurements on Solidifying Melt*, *J. Fluids. Eng.*, 126 (2004) 193-197.
- [2004Cha] Y. Austin Chang, S. Chen, F. Zhang, X. Yan, F. Xie, R. Schmid-Fetzer, W. Alan Oates, *Phase Diagram Calculation: Past, Present and Future*, *Prog. Mater. Sci.*, 49 (2004) 313-345.
- [2004Pra] A. Prasad, H. Henein, F. Maire, C.A. Gandin, *X-ray tomography study of atomized Al-Cu droplets*, *Can. Metall. Q.*, 43(2) (2004) 273-82.
- [2005Che] Z.W. Chen, *Formation and progression of die soldering during high pressure die casting*, *Mater. Sci. Eng. A*, 397 (2005) 356-369.
- [2004Gro] J. Gröbner, D. Mirković, R. Schmid-Fetzer, *Grain Refining and Solidification Enthalpies of Al-Ce-Si Alloys*, *Metall. Mater. Trans. A*, 35A (2004) 3349-3362.
- [2005Dio] A. Diószegi, I.L. Svensson, *On the problems of thermal analysis of solidification*, *Mater. Sci. Eng. A*, 413-414 (2005) 474-479.
- [2005Don] H.B. Dong, J.D. Hunt, *A numerical model for a heat flux DSC: Determining heat transfer coefficients within a DSC*, *Mater. Sci. Eng. A*, 413-414 (2005) 470-473.
- [2005Kur] E.C. Kurum, H. B. Dong, J. D. Hunt, *Microsegregation in Al-Cu alloys*, *Metall. Mater. Trans. A*, 36, 11, (2005) 3103-3110.
- [2005Gan] M. Ganesan, D. Dye, P.D. Lee, *A Technique for Characterizing Microsegregation in Multicomponent Alloys and Its Application to Single-Crystal Superalloy Castings*, *Metall. Mater. Trans. A*, 36a (2005) 2191-2204.
- [2005Haz] A. Hazotte, J.S. Lecomte, J. Lacaze, *Setting-up rules to characterize microsegregation*, *Mater. Sci. Eng. A*, 413-414, (2005) 223-228.
- [2005Mat] R.H. Mathiesen, L. Arnberg, *X-ray radiography observations of columnar dendritic growth and constitutional undercooling in an Al-30wt%Cu alloy*, *Acta mater.*, 53(4) (2005) 947-956.
- [2005Mat1] R.H. Mathiesen, L. Arnberg, *Stray crystal formation in Al-20wt.% Cu studied by synchrotron X-ray video microscopy*, *Mater. Sci. Eng. A*, 413 (2005) 283-287.
- [2006Cao] G. Cao, S. Kou, *Predicting and reducing liquation-cracking susceptibility based on temperature vs. fraction solid*, *Weld. J.*, 85(1) (2006) 9-18.
- [2006Fen] Q. Feng, L.J. Carroll, T.M. Pollock, *Solidification segregation in ruthenium-containing nickel-base superalloys*, *Metall. Mater. Trans. A*, 37, 6 (2006) 1949-1962.
- [2005Ger] V.Y. Gertsman, L. Jian, S.Xu, J.P. Thomson, M. Sahoo, *Microstructure and second-phase particles in low- and high-pressure die-cast magnesium alloy AM50*, *Metall. Mater. Trans. A*, 36, 8 (2005) 1989-1997.
- [2006Li] B. Li, H.D. Brody, A. Kazimirov, *Synchrotron microradiography of temperature gradient zone melting in directional solidification*, *Metall. Mater. Trans. A*, 37A(3A) (2006) 1039-1044.
- [2006Mir] D. Mirković, R. Schmid-Fetzer, *Solidification curves for commercial Mg alloys obtained from heat-transfer modeled DTA experiments*, *Z. Metallkd.*, 97 (2006) 119-129.
- [2006Ohn1] M. Ohno, D. Mirković, R. Schmid-Fetzer, *Liquidus and Solidus Temperatures of Mg-rich Mg-Al-Mn-Zn Alloy*, *Acta Mater.*, 54 (2006) 3883-3891.
- [2006Ohn2] M. Ohno, R. Schmid-Fetzer, *Mg-rich phase equilibria of Mg-Mn-Zn alloys analyzed by computational thermochemistry*, *Int. J. Materials Research (Z. Metallkd.)*, 97 (2006) 526-532.
- [2006Ohn3] M. Ohno, D. Mirković, R. Schmid-Fetzer, *Phase equilibria and solidification of Mg-rich Mg-Al-Zn alloys*, *Mater. Sci. Eng. A*, 421 (2006) 328-337.
- [2007Gan] M. Ganesan, L. Thuinet, D. Dye, P.D. Lee, *Quantification of Microsegregation in Cast Al-Si-Cu Alloys*, *Metall. Mater. Trans. B*, 38b (2007) 557-566.
- [2007Kul] M.K. Kulekci, *Magnesium and its alloys applications in automotive industry*, *Int. J. Adv. Manuf.*

- 
- Technol, (2007) online publishing.
- [2007Mir] D. Mirkovic, R. Schmid-Fetzer, *Solidification curves for commercial Mg alloys determined from differential scanning calorimetry with improved heat transfer modeling*, Metall. Mater. Trans. A, 38A (2007) 2575-2592.
- [2007Nos] M. Nose, T. Kawabata, M. Ohi, T. Nagae, S. Masa, Y. Hatano, S. Ikeno, K. Nogi, *Development of PVD-TiAlN/a-C Nanocomposite Coating for Pressure Die Casting Applications*, Plasma Process. Polym., 4 (2007) 681-686.
- [2007Zha] C. Zhang, D. Ma, K.-S. Wu, H.-B. Cao, G.-P. Cao, S. Kou, Y.A. Chang, X.-Y. Yan, *Microstructure and microsegregation in directionally solidified Mg-4Al alloy*, Intermetallics, 15, 10 (2007) 1395-1400.
-



## Curriculum vitae

### Personal Data:

Name: Djordje Mirković  
Date of Birth: August 14<sup>th</sup> 1970  
Place of Birth: Užice, Serbia  
Nationality: Serbian  
Marital status: married, one daughter

### School Education:

September 1977 - Jun 1985 Elementary school „Andrija Djurović“, Užice  
September 1985 - June 1989 Secondary school „Radoje Marić“, Užice  
June 1989 Degree “Technician for Mechanical Engineering”

**Military service:** September 1989 - August 1990, Danilovgrad, Montenegro

### University Education:

July 1990 - January 1996 study in the metallurgical department at the Faculty of Technology and Metallurgy, Belgrade University.  
February 1996 - June 1996 graduation work: “Structure and properties of medium carbon V-micro alloyed as-forged steels”  
June 1996 Degree: Diplom-Ingenieur

### Current Position:

since January 1997 Research assistant,  
Institute of Metallurgy,  
Clausthal University of Technology

---